Processing and protection of rare earth permanent magnet particulate for bonded magnet applications

by

Peter Kelly Sokolowski

A thesis submitted to the graduate faculty

in partial fulfillment of the requirements for the degree of

MASTER OF SCIENCE

Major: Materials Science and Engineering

Program of Study Committee:
Iver E. Anderson, Major Professor
Ralph W. McCallum
Frank E. Peters

Iowa State University

Ames, Iowa

2007

Dedicated to my family and friends
who instilled in me the importance and aptitude
of learning is a lifelong goal.

TABLE OF CONTENTS

ABSTRACT

Rapid solidification of novel mixed rare earth-iron-boron, $MRE_2Fe_{14}B$ (MRE = Nd, Y, Dy; currently), magnet alloys via high pressure gas atomization (HPGA) have produced similar properties and structures as closely related alloys produced by melt spinning (MS) at low wheel speeds. Recent additions of titanium carbide and zirconium to the permanent magnet (PM) alloy design in HPGA powder (using He atomization gas) have made it possible to achieve highly refined microstructures with magnetic properties approaching melt spun particulate at cooling rates of 10^5-10^6K/s. By producing HPGA powders with the desirable qualities of melt spun ribbon, the need for crushing ribbon was eliminated in bonded magnet fabrication. The spherical geometry of HPGA powders is more ideal for processing of bonded permanent magnets since higher loading fractions can be obtained during compression and injection molding. This increased volume loading of spherical PM powder can be predicted to yield a higher maximum energy product $(BH)_{max}$ for bonded magnets in high performance applications.

Passivation of RE-containing powder is warranted for the large-scale manufacturing of bonded magnets in applications with increased temperature and exposure to humidity. Irreversible magnetic losses due to oxidation and corrosion of particulates is a known drawback of RE-Fe-B based alloys during further processing, e.g. injection molding, as well as during use as a bonded magnet. To counteract these effects, a modified gas atomization chamber allowed for a novel approach to in situ passivation of solidified particle surfaces through injection of a reactive gas, nitrogen trifluoride (NF_3). The ability to control surface chemistry during atomization processing of fine spherical RE-Fe-B powders produced advantages over current processing methodologies. In particular, the capability to coat particles while “in flight” may eliminate the need for post atomization treatment, otherwise a necessary step for oxidation and corrosion resistance. Stability of these thin films was attributed to the reduction of each RE’s respective oxide during processing; recognizing that fluoride compounds exhibit a slightly higher (negative) free energy driving force for

formation. Formation of RE-type fluorides on the surface was evidenced through x-ray photoelectron spectroscopy (XPS). Concurrent research with auger electron spectroscopy has been attempted to accurately quantify the depth of fluoride formation in order to grasp the extent of fluorination reactions with spherical and flake particulate. Gas fusion analysis on coated powders (dia. <45μm) from an optimized experiment indicated an as-atomized oxygen concentration of 343ppm, where typical, nonpassivated RE atomized alloys exhibit an average of 1800ppm oxygen. Thermogravimetric analysis (TGA) on the same powder revealed a decreased rate of oxidation at elevated temperatures up to 300°C, compared to similar uncoated powder.

THESIS ORGANIZATION

The thesis begins as a general description of the purpose of this study. The literature review starts with a brief history of permanent magnetism and topics which support information presented in the body of the text. The idea is to provide background on the discovery of magnetism and the evolution of permanent magnets as their industrial importance grew. In addition, background on rapid solidification, alloying behavior, and processing of rare earth magnets is given such that the reader is made aware of the different methods of production and as a result, the influence these parameters have on the magnetic properties. The remainder of the literature review details the significance of protecting magnets from oxidation and corrosion during service. In particular, the concept of in situ HPGA particle surface fluorination and the modification of a fluidized bed for controlled growth of a rare earth fluoride coating are aimed at preventing ambient oxidation and reducing the rate of oxidation at elevated temperatures.

Next, the methods used to produce magnetic particulate and fluorinate samples in a magnetically stirred fluidized bed as well as the first trials with in situ HPGA fluorination are presented. Following is a list and description of the analysis techniques used to obtain the body of the results. The results section begins with microstructural and magnetic analysis in order to correlate solidification structures to magnetic properties of a similar alloy produced by two separate methods. This analysis was performed as supporting information during alloy development, a main focus of the overall research goal, though not the focus of this thesis' contribution. The remainder of the results, which is the chief contribution, provides information on surface passivation improvement through controlled fluorination both in the magnetically stirred fluidized bed apparatus and gas atomization chamber.

After the main body, a brief discussion and conclusion detailing the highlights of the results is given followed by an acknowledgement of the source of funding and everyone who has uniquely influenced this thesis.

PURPOSE OF STUDY

In order to meet cost and performance goals for advanced electric drive motors which utilize an internal permanent magnet (PM) rotor design, it was necessary to characterize the effects of PM alloy modifications for the translation from melt spinning (MS) to high pressure gas atomization (HPGA) processing. Melt spinning was used during initial development of a preferred magnet alloy, while HPGA is the preferred processing route for production of spherical magnetic particulate for use in isotropic bonded PM with increased volumetric solids loading. This characterization effort aimed to establish specific microstructural effects on the magnetic properties as a result of the differences in processing and alloy components. Differences in heat flow directionality induced by the MS and HPGA processing methods appeared to be responsible for the different solidification microstructures (at least in part) and for the resulting magnetic properties. However, recent alloying additions (e.g. Zr and TiC) were intended to encourage similar solidification behavior such that meaningful microstructural predictions could be made to facilitate the translation from one processing method to the other.

In addition, the incorporation of an in situ HPGA fluoride gas-solid reaction needed to be developed to form a protective coating on atomized particulate, capable of reducing the rate of oxidation during further handling. Since oxidation and corrosion of similar magnetic material was shown to result in irreversible magnetic losses over time, the formation of rare earth-type fluorides (REF_3, REOF) on the spherical particle surfaces was attempted to prevent degradation prior to the polymer bonding step and for increased performance reliability. Initial in situ treatment results were shown to be successful at forming a protective fluoride layer, however it was essential to determine an effective fluoride thickness, thereby optimizing processing conditions and providing a viable industrial concept. The use of a small scale fluidized bed apparatus provided a method for surface passivation of both flake and spherical magnetic particulate to develop effective control of fluoride thickness. A challenge was faced for transferring optimal fluorination parameters from the

fluidized bed reactor to the in situ HPGA procedure where the environment is highly chaotic with non-steady state conditions in comparison to the fluidized bed.

As a result of this work, compression bonded magnet samples will be produced with surface treated magnet material from a scaled-up fluidized bed for testing of short term and long term irreversible magnetic losses (STILT, LTILT) in conjunction with an industrial partner. The systematic characterization of alloy development and optimized application of a protective coating will be useful for the overall objective of providing a reliable PM material for use in advanced applications at temperatures approaching 200°C.

1. LITERATURE REVIEW

1.1 History of Permanent Magnets

Attraction to the mystical properties of magnets has been around for over 4,000 years and these materials are perhaps still puzzling to many. Certainly, there is continued interest in understanding and optimizing their beneficial properties and in development of advanced magnetic materials. Several major scientific breakthroughs in advanced magnetic materials were notable in the past century, including the discovery of $RE_2Fe_{14}B$ magnets in the 1980's.

The origin of the word *magnet* is derived from one of two possibilities. One, being more of a legend, is believed to be from the name of a shepherd, Magnes, in ancient Greece who discovered that iron nails in his shoes and the tip of his staff "stuck fast in a magnetic field while he pastured his flocks" [1]. The other derivation comes from Magnesia, a land region in Macedonia where deposits of magnetic "lodestones" were commonly found. This lodestone, a 16^{th} century term coming from *lode* - an old English word for leading or guiding, was discovered to exhibit an unusual attractive force, now referred to as magnetism. It was the first material to demonstrate a constant or "permanent" magnetic force, although very weak by today's standards, which was believed to have been induced from lightning strikes [2]. Lodestone possesses this unique property due to its chemical composition and characteristic internal structure, something not realized until the advent of microscopes. It is comprised of several forms of iron oxide, mostly magnetite (Fe_3O_4) and small concentrations of wustite (FeO), hematite (Fe_2O_3), and maghemite (Fe_2O_3) a form of magnetite. The random and inhomogeneous distribution of wustite, hematite, and maghemite, considered to be "impurities" in magnetite, as well as other elemental traces, are responsible for pinning magnetic domains within the material and, thereby, creating a permanent magnet effect.

In contrast, pure iron or magnetite by itself is essentially a soft magnet, exhibiting little or no external magnetization without the alignment effect of an applied field. To differentiate

between a permanent, or hard, magnet (PM) and a soft magnet, a quantity known as coercivity is used to describe the amount of applied magnetic field required to demagnetize it. This extrinsic property is determined in part by the microstructure of the material as a result of the solidification process and by its thermal history [3]. The intrinsic coercive field H_{ci} needed to reverse magnetic alignment in a magnet is however a function of its limiting magnetic saturation based on equation 1 [4]. Where K_1 is a constant relating a material's preferred alignment of the magnetic dipole moments, known as magnetocrystalline anisotropy, and μ_0 is the permeability of free space.

$$H_{ci} = \frac{2K_1}{\mu_0 M_{sat}} \tag{1}$$

The greater an applied field needed to reduce magnetization to zero, the greater the strength of the PM, whereas an ideal soft magnet would have coercivity near zero. As mentioned, another attribute of a magnet is its saturation magnetization M_{sat}, meaning the extent to which it can be magnetized. Saturation is dependent only on the magnitude of the atomic magnetic moments and number of atoms per unit volume [4]. Soft magnets tend to have a greater saturation over permanent magnets, an intrinsic compositional effect. Upon saturation and removal of an applied field, the magnetization of a magnet will revert to a residual magnetic state, or its remanence M_R. These properties, of a magnet, can be directly inferred from a hysteresis loop as seen in Figure 1, with H being the applied field and B the induced magnetism (where remanent induction $B_R = \mu_0 M_R$).

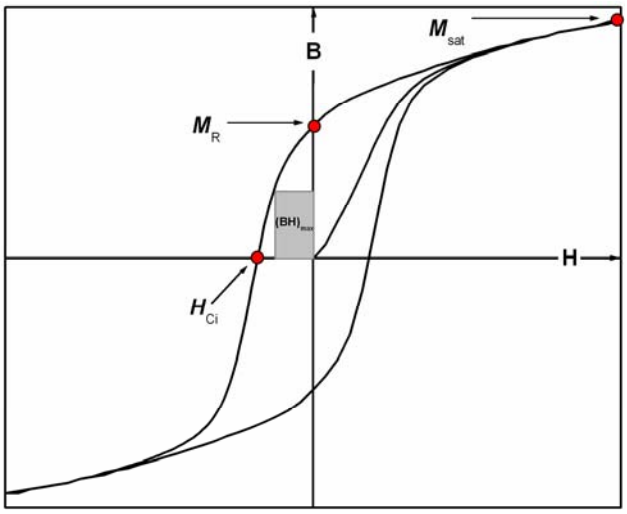

Figure 1: Generalized magnetic hysteresis loop, H being the applied field and B the induced magnetism.

Through extensive research into modified steel magnets in the 1930's, it was noticed that significant additions of aluminum, nickel, and cobalt in solution with iron produced a highly effective and commercially viable PM produced by conventional ingot casting. These AlNiCo magnets were 100 times stronger than any lodestone, with maximum energy products approaching 10 MGOe [2]. The maximum energy product, $(BH)_{max}$, represents a magnet's ability to store energy or deliver work outside of its volume, thereby indicating the performance or strength of the PM. As illustrated with the shaded region in Figure 1, a magnet's energy product is directly proportional to the material's M_{sat} through equation 2 [4]. Therefore, a magnet's performance can be greatly enhanced if its intrinsic saturation is increased through using elements with higher initial M_{sat}.

$$-(BH)_{\max} = \mu_0 \left(\frac{M_{sat}}{2} \right)^2 \tag{2}$$

Later in the 1950's, ceramic ferrite magnets with compositions composed of Fe_2O_3 and either strontium (Sr) oxide or barium (Ba) oxide were introduced as "next generation" PM materials, finding a broad range of applications. Their relatively cheap raw material cost and ease of production made them ideal for bulk manufacturing, although they were limited in their effective energy product. Hard ferrite magnets still account for nearly 90 percent, by

weight, of the PM market due to their low cost (1996 estimate) [2]. Alternatively, another important class of rare earth (RE) type PM gained popularity in the 1960's due in part to the recent success in the reduction of rare earth elements to their pure form [5]. A realization that rare earth elements, when coupled with transition metals (RE-TM, where TM = iron, cobalt, and nickel for instance), formed intermetallic compounds [6], resulted in a quick progression of increased $(BH)_{max}$ within a smaller volume of material. Theoretically, these materials were suggested to have the highest magnetocrystalline anisotropy allowing for increased M_{sat} and ultimately the highest $(BH)_{max}$ to date [7]. Initially, compounds based on samarium and cobalt (Sm-Co) became known for having the highest energy product for many years as well as the greatest temperature stability. Conversely, several factors have made Sm-Co type magnets more appropriate for high performance applications only. The shortage in supply of raw materials (elemental Sm and Co), difficulty in producing the compounds, and their brittle nature have made them expensive and non-ideal for broad application.

1.2 Development of 2-14-1 Magnets

The search for a more feasible PM with equally impressive magnetic properties, compared to Sm-Co, resulted in a more notable RE-TM hard magnetic phase, based on the ternary compound $RE_2Fe_{14}B$ (RE = Nd, primarily) with a tetragonal structure and magnetic axis along its *c*-axis [7][8]. It was simultaneously discovered through two separate processing routes. A chillcasting/annealing/grinding and powder sintering method was developed by Sagawa *et al* [9] at Sumitomo Special Metals of Japan and a rapid quenching/(brief) anneal process, termed *magnequench* was developed by Croat *et al* [10] at General Motors of the U.S. in 1984. The advantage of this alloy was that its main constituents, Fe and Nd, are more abundant than those of Sm-Co type magnets, allowing for significantly reduced raw materials cost. Also, their $(BH)_{max}$ was superior with a predicted M_{sat} of 10.1 kGs [4] surpassing that of Sm-Co (6.1 kGs), which made them desirable for numerous applications. The principle drawback pertains to their temperature dependence, with a Curie temperature of only 312°C,

compared to the most widely used magnetic materials and their associated T_C values and applicable energy products, $(BH)_{max}$, in Table I [4]. The Curie temperature is defined as the transition temperature at which magnetic alignment or ordering is destroyed and the material goes from ferromagnetic or ferrimagnetic to paramagnetic behavior [4].

Table I: Curie temperature and energy product of common magnetic materials.

Material	T_C *(°C)*	$(BH)_{max}$ *theoretical (MGOe)*
Iron	770	0.2
Nickel	358	-
Cobalt	1130	-
Gadolinium	20	-
Terfenol ($Tb_{0.3}Dy_{0.7}Fe_2$)	380-430	-
$Nd_2Fe_{14}B$	312	65.6
Alnico ($Fe_{35}Co_{35}Ni_{15}Al_7Cu_4Ti_4$)	850	9.4
$SmCo_5$	720	20
Sm_2Co_{17}	810	30
Hard ferrites ($SrO{\cdot}6Fe_2O_3$)	400-700	2.5
Barium ferrite ($BaO{\cdot}6Fe_2O_3$)	450	3.5

Actually, the practical operating temperature for $Nd_2Fe_{14}B$ magnets is in the range of 125°C to 150°C, well below its respective T_C. This sensitivity to temperature has been a limitation for Nd-Fe-B type magnets and has hindered its use in high temperature applications. A further problem surrounding Nd-Fe-B magnets has been its rather low corrosion resistance. RE elements are highly susceptible to oxidation and corrosion in applications with increased temperature and high humidity [11], leading to reduced magnetic properties over time. It is known that the light rare earth elements, such as Nd, are easily oxidized [12]. The formation of the oxide, Nd_2O_3, reduces the amount of the Nd-rich phase which is responsible for pinning of the domain walls. As the Nd-rich grain boundaries break down, the effective H_c declines rapidly [13]. Without providing a protective surface coating, i.e. epoxy or metallic, or alloying addition to a RE element, exposure to moisture was found to cause the reactions listed as equations 3 and 4 [14]. The decomposition of water vapor reacting with Nd results in the local production of hydrogen. Hydrogen, known to easily diffuse throughout the bulk

of the material, preferentially reacts with the Nd-rich areas, equation 4. This leads to intergranular hydrogen embrittlement which escalates the corrosion process throughout the volume of the material and further degrades its useful properties, magnetically and structurally.

$$Nd + 3H_2O \rightarrow Nd(OH)_3 + 3H \tag{3}$$

$$Nd + 3H \rightarrow NdH_3 \tag{4}$$

1.3 Thermal stability of 2-14-1 Magnets

To counteract problems with temperature dependence and environmental degradation, much research has gone into developing Nd-Fe-B based magnets with enhanced properties, both intrinsically through alloy modifications (i.e. Co, Ni, Al additions) and extrinsically by means of surface modification techniques (i.e. epoxy resin coatings and Ni plating) [13][15][16]. For example, small substitutions of Co for Fe can result in a noticeably higher T_C value for the mixed 2-14-1 compound [17] and can significantly improve high temperature properties, as research by Campbell *et al* clearly showed, Figure 2 [13].

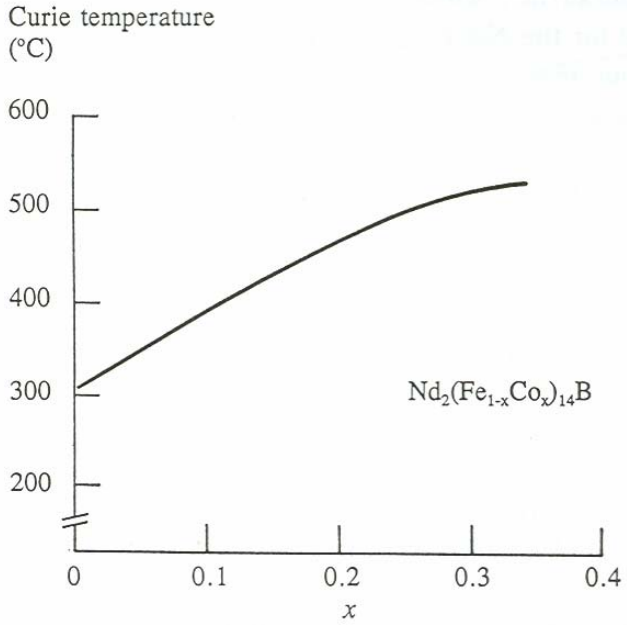

Figure 2: Effect of Co substitution on the Curie temperature of $Nd_2Fe_{14}B$.

However, this benefit was derived at the cost of reduced intrinsic coercivity. One way to offset the effect of a lower H_{ci} has been to substitute a heavy rare earth, such as Dy, in for Nd, since $Dy_2Fe_{14}B$ is known to exhibit a higher anisotropy than $Nd_2Fe_{14}B$. Unfortunately Dy has an antiferromagnetic coupling with Co, which further reduces the saturation magnetization and lowers $(BH)_{max}$. Through sensible substitutions of Co and Dy within the alloy, the adverse effects were able to be minimized, while thermal stability was enhanced [13].

1.4 Current Progress on 2-14-1 Magnets

Today, permanent magnets based on Nd-Fe-B constitute an interesting area for continued commercial development through basic research focused on enhancing their attractive intrinsic properties and applied research targeted to customizing the extrinsic magnetic properties for specific use [6]. Typically, modifications have aimed at improving the lifetime and reducing the cost of anisotropic sintered PM due to their desirable energy products. However, in recent years polymer bonded isotropic permanent magnets (PBPM) have grown

in interest [18][19] for their ability to form complex net shapes at low cost for use in electric motors and other automotive devices, a topic to be discussed in a following section.

As industry demands continually increase, required operating temperatures for bonded magnets are nearing 200°C and current commercial $RE_2Fe_{14}B$ alloys are incapable of maintaining adequate magnetic performance. To combat the need for increased reliability and performance at 200°C, a MRE-Fe-B alloy modification (MRE = Nd, Y, Dy; currently) has been designed to maintain a sufficient $(BH)_{max}$ at elevated temperatures through judicious "mixed RE" alloying additions [20]. The development of a $MRE_2Fe_{14}B$ solid solution was founded on previous magnetic studies of the individual intrinsic 2-14-1 properties [21][22]. Figure 3 shows the temperature dependence of the magnetic moment (affecting remanence) and anisotropy energy (affecting coercivity) for each respective $RE_2Fe_{14}B$. It was noticed that $Nd_2Fe_{14}B$ possesses the highest saturation (Figure 3a), while $Dy_2Fe_{14}B$ (Figure 3b) has the greatest anisotropy [13], however each is strongly dependent on temperature and declines rapidly at increased T. Conversely, $Dy_2Fe_{14}B$ exhibits a diminished saturation dependency on temperature (Figure 3a) as does $Y_2Fe_{14}B$ with anisotropy (Figure 3b), although their respective magnetic property levels are substantially lower at room T.

It was believed that, through ideal solid solution behavior, addition of both Dy and Y will effectively improve magnetic temperature stability at increased T, but at the price of a somewhat decreased $(BH)_{max}$ at ambient temperature [20]. Indeed, this complex alloy design strategy that also uses a Co addition [13] was demonstrated by a melt spinning approach to produce superior isotropic magnetic energy product values above about 125°C, although lagging the benchmark properties at ambient temperature (see Figure 4).

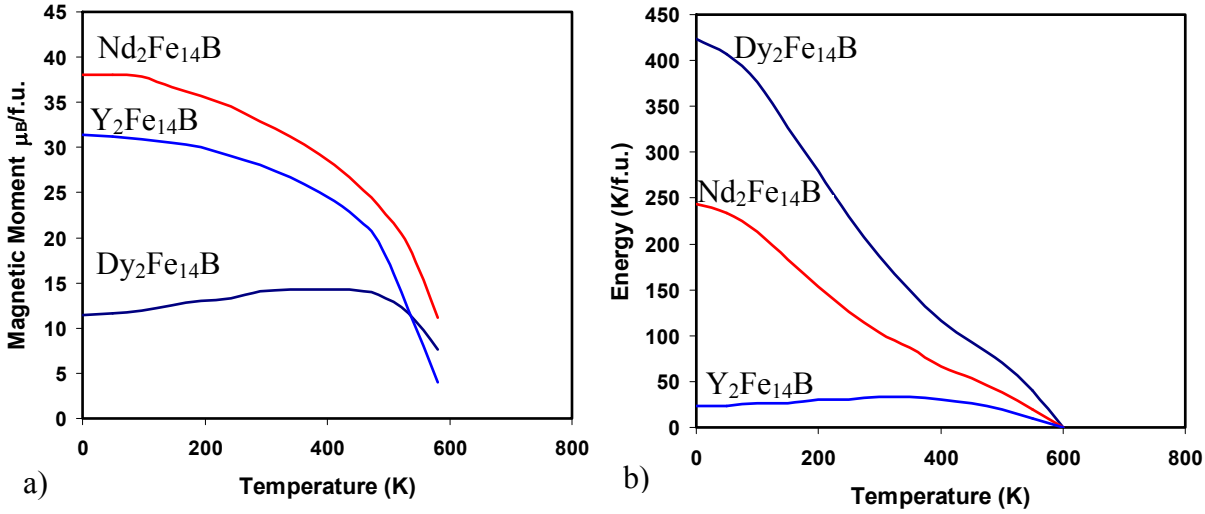

Figure 3: (a) Magnetic moment (remanence) and (b) anisotropy energy (coercivity) dependence on temperature for each $RE_2Fe_{14}B$.

From a more general perspective, high temperature vibrating sample magnetometer (VSM) measurements in Figure 4 reveal the progress in magnet alloy design. The new MRE-Fe-B alloy designs are capable of retaining greater $(BH)_{max}$ values at higher temperatures, as noted with cross-over points by the dashed lines, over the commercially available alloys produced by Magnequench Inc. (MQP) [23]. The curves with the hollow symbol represent alloys produced at Ames Laboratory in melt spun ribbon (WT-102) and in gas atomized spherical powder $[Nd_{0.45}(Y_{0.66}Dy_{0.33})_{0.55}]_{2.3\text{-}0.1}Zr_{0.1}(Fe_{0.89}Co_{0.11})_{14}B+Ti_{0.02}C_{0.02}$ (GA-1-66) forms, compared to their commercial counterparts. The spherical form of the alloy, GA-1-66, maintains a greater $(BH)_{max}$ at 150°C over MQP-S-11-9, and further alloy development aims to reduce the cross-over point to that of the melt spun version, 125°C.

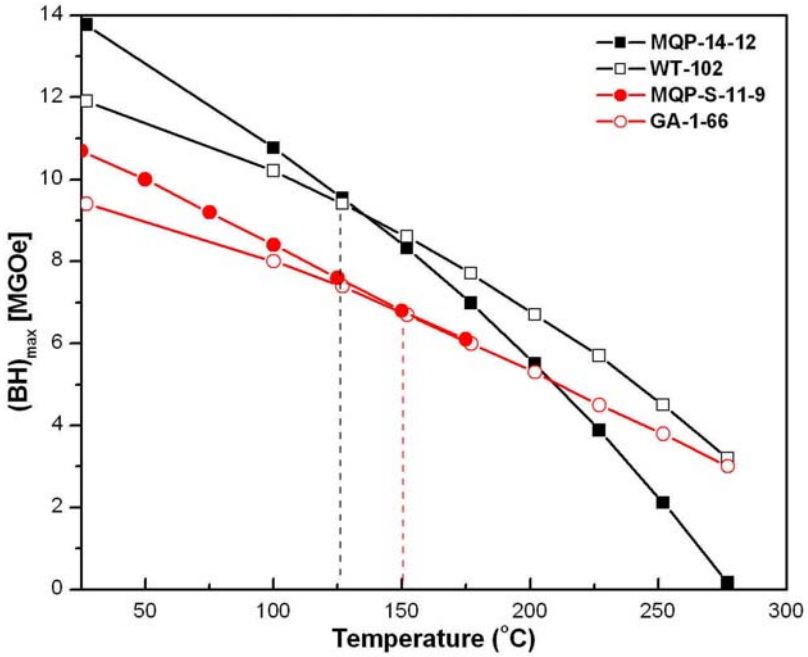

Figure 4: Comparison of energy products $(BH)_{max}$ for different alloys as a function of Temperature. Square symbols indicate flake particulate produced by melt spinning; circular symbols indicate spherical particulate produced by HPGA.

1.5 Ames Lab Alloy Improvements

As previously mentioned, it was demonstrated that the novel $MRE_2Fe_{14}B$ magnet alloy design approach resulted in a reduced loss of $(BH)_{max}$ at 200°C when compared to commercial $Nd_2Fe_{14}B$ [24]. Although the MRE alloys generally exhibit a lower $(BH)_{max}$ at room temperature, compared to commercial counterparts, they can begin to retain a greater $(BH)_{max}$ over the commercial alloys above 125°C (and up to the Curie temperature, ~312°C). These improved high temperature magnetic properties can be beneficial to motor designers that must plan for a motor operating temperature regime of 150°C - 200°C. This significant attribute was accomplished initially by substituting dysprosium and yttrium for neodymium on the rare earth sites in the $Nd_2Fe_{14}B$ tetragonal structure, the prototype PM compound exhibiting the highest $(BH)_{max}$ to date [25].

It is widely known that $Dy_2Fe_{14}B$ and $Y_2Fe_{14}B$ demonstrate a stabilization of remanence M_r and coercivity H_C, respectively, with an increase in temperature as previously stated. Now, it has been demonstrated that the Dy and Y substitution for Nd can provide temperature stabilization for the mixed 2-14-1 compound, proving to be an acceptable combination as a hard magnet. Subsequent alloy enhancements included the addition of Nd to boost the energy product and incorporation of Co, which is known to increase the Curie temperature of PM's. However, these additions led to an increased tendency for the formation of soft magnetic phases Nd_2Fe_{17} or α-Fe. To resolve this issue, a series of experiments were performed to establish the effect of an increased zirconium substitution for the rare earth sites to obtain improved magnetic properties [26]. Zr, normally a glass former, effectively inhibits the growth of grains during solidification, and makes it possible to bypass the nucleation of soft phases and to promote the formation of the hard 2-14-1 phase [27]. The optimized magnetic properties were achieved through the addition of 0.4wt% Zr, which produced a refined and uniform 2-14-1 microstructure on the order of 65nm exhibiting H_C of 10.6 kOe and $(BH)_{max}$ of 9.56 MGOe [26].

In order to refine the microstructure further and provide a mechanism to inhibit grain coarsening during annealing, TiC was incorporated into the alloy design. Previous research [28][29][30] on TiC additions to stoichiometric 2-14-1 found that there was nearly zero solubility in 2-14-1, forming precipitates of the compound during RSP at grain boundaries. These precipitates provided a nucleation site for the hard magnetic phase as well as an effective grain pinning mechanism, resulting in a refined microstructure. Through adding a glass former and a mechanism to inhibit grain growth [31], the high cooling rate required to form 2-14-1 no longer becomes a necessity, making it possible to move toward a lower cooling rate processing route when compared to melt spinning, e.g. high pressure gas atomization.

1.6 Rapid Solidification

Under typical casting conditions, i.e. with a large continuous liquid volume poured into a mold, the onset of solidification occurs at the most potent nucleation sites within the liquid metal or at its surface. The resulting crystal phases will continue to grow until impingement with a grain boundary, pinning site, or exhausting all available liquid phase, effectively stopping growth. Typically, heterogeneous nucleation (non-intrinsic) sites are associated with the presence of an impurity or pre-existing catalyst that reduces the barrier for the onset of solidification at the location of the nucleant [32][33]. In order to avoid active heterogeneous nucleation and to establish high undercooling within a melt volume that promotes increased solidification rates, methods such as forming isolated liquid droplets, conditioning of the bulk sample, and rapid cooling are primarily used [33]. Isolation of the most active heterogeneous nucleation sites, or motes, is achieved by breaking a volume of liquid into progressively smaller divisions of the original volume and in doing so producing an increased population of mote-free, deeply undercooled particles. This mote isolation effect is illustrated in Figure 5, where an increase in subdivisions of a given volume, corresponding to increased mote-free fractions X, reduces the probability of finding a mote in any explicit melt volume partition [34].

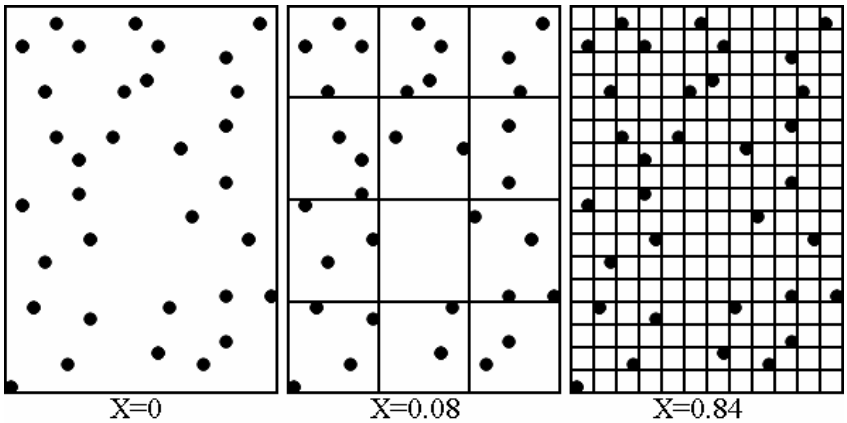

Figure 5: Consecutive subdivisions display mote isolation effect as increase in X relates to increased volume of highly undercooled particles.

Conditioning of a bulk melt involves encasement of the melt with a layer of inorganic glass, for instance, which prevents possible catalytic sites on the container wall from initiating nucleation. This inactive layer may also act to capture nucleants from the melt during melting and cooling cycles, preventing the motes from heterogeneous nucleation within the volume. This approach can lead to considerable undercooling, however is not as efficient as the isolation of liquid droplets.

Rapid cooling, a function of the heat flow characteristics, is established through processing conditions. Cooling of the melt requires heat transfer to the surroundings, either through conductive, convective, or radiative mechanisms, with conductive heat transfer being the most effective. The medium through which heat transfer takes place, i.e. conduction to a rotating Cu wheel for melt spinning or convection to the cooled gas for atomization (to be discussed in greater detail), greatly influences the extent to which a melt can obtain deep undercoolings and maintain a rapid solidification rate. The heat transfer coefficient, h, is a measure of the effectiveness of the quenching medium where conduction to a substrate is in the range of 10^{-1} to 10^{2} W/cm^{2}K and convective cooling with gas ranges from 10^{-3} to 10^{2} W/cm^{2}K depending on particle size [32][35]. For atomized particles, equation 5 [35] relates the effectiveness of the atomizing gas and particle size to h, dictated by convective and radiative heat flow considerations. Where k_f is the conductivity of the atomizing gas (He = 0.1394 W·m^{-1}·°C, N_2 = 0.0252 W·m^{-1}·°C [36]), D is the particle diameter, and Re and Pr are the Reynold's number and Prandtl number respectively.

$$\frac{hD}{k_f} = 2.0 + 0.6\,\mathrm{Re}^{1/2}\,\mathrm{Pr}^{1/3} \tag{5}$$

The Reynold's number, equation 6, is a function of the velocity, v, of the atomizing gas, diameter of the particle, the density of the atomizing gas, ρ_f (He = 0.1635 kg·m^{-3}, N_2 = 1.137 kg·m^{-3}[36]) and the viscosity of the atomizing gas, μ_f (He = 1.72x10^{-5} kg·ms^{-1}, N_2 = 1.78x10^{-5} kg·ms^{-1}[36])

$$\mathrm{Re} = vD\frac{\rho_f}{\mu_f} \tag{6}$$

The Prandtl number, equation 7, accounts for the specific heat of the atomizing gas, C_f (He = 5.25 kJ·kg^{-1}·°C, N_2 = 1.03 kJ·kg^{-1}·°C [36]) as well as the viscosity and conductivity of the gas.

$$\mathrm{Pr} = C_f\frac{\mu_f}{k_f} \tag{7}$$

It is known that rapid solidification of a melt requires accelerated removal of the latent heat of fusion, a consequence of crystallization. If the latent heat is not adequately absorbed by the remaining liquid fraction and removed through external heat extraction at a high enough rate, the previously solidified material must serve as a heat sink to absorb the heat instead. This crystallization heat release phenomenon, known as recalescence, may lead to considerable heating of the solidified material in the quasi-adiabatic solidification situation, just described. An increase in solid temperature then reduces the solidification velocity as the temperature gradient across the solid-liquid interface is minimized. Normally, a change in solidification velocity is illustrated with a microstructural transformation as stability of the growth interface adjusts.

In the case of atomization, reduced particle sizes are capable of experiencing high initial undercoolings, leading to rapid solidification and most likely the formation of a refined microstructure or an amorphous phase [37]. However, for larger particles, heterogeneous nucleation can prevent deep undercooling and continued rapid solidification of the particle microstructure, resulting in unstable crystal growth, typically represented by dendritic or cellular pattern formation. Figure 6 [38] describes three general cases for solidification of atomized particulate. Path A, usually experienced by larger particles (dia. >50μm), shows solidification occurring isothermally. This allows for increased segregation and dendritic growth since there is essentially no undercooling and little temperature gradient and hence no driving force for a high solidification rate.

In contrast, if nucleation is kinetically suppressed within a given volume (characteristically seen in very fine particles, dia. <5μm) and an equal amount of enthalpy (heat) in regards to the heat of fusion has been removed prior to solidification, then adiabatic solidification (as described above) occurs, path B [38]. Particle morphologies associated with path B are (depending on alloy composition) usually amorphous or highly refined nanostructures embedded within an amorphous matrix as a result of the extreme undercooling, on the order of $0.22T_m$ (absolute) or greater [3]. Generally, the bulk of atomized particulate will follow path C, where initial liquid undercooling levels absorb the released heat of fusion until the majority of the undercooling is relieved. At this stage however, continued recalescence allows solute partitioning due to slowed solidification, approaching isothermal solidification, since heat flow is now restricted to external heat extraction [38]. In this case, a mixed microstructure is often formed as a result of the solidification rate change, revealing a combination of a supersaturated crystalline/amorphous area and a segregated dendritic/cellular region.

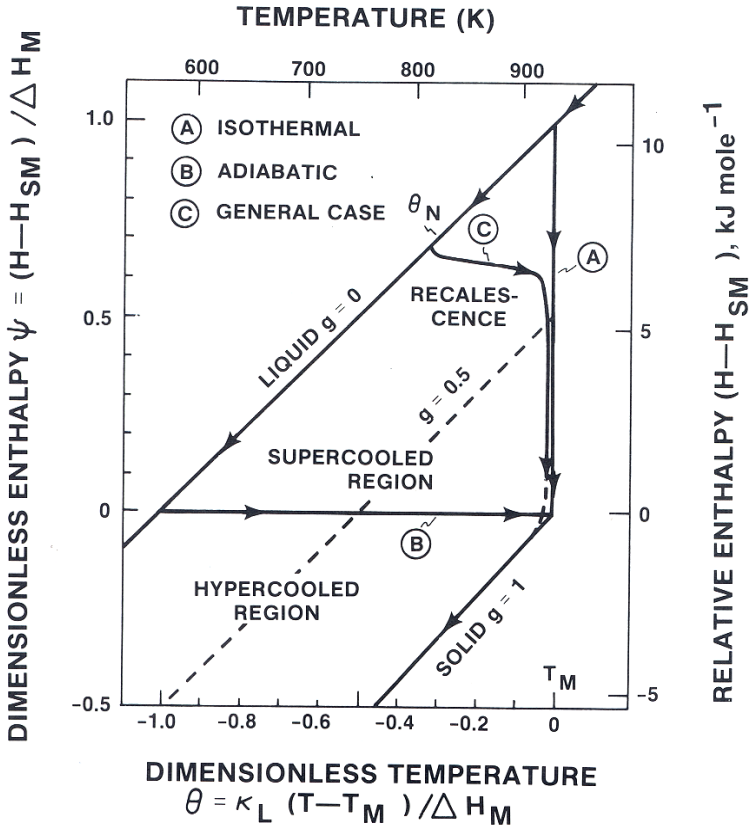

Figure 6: Possible solidification paths for atomized powder as a function of enthalpy.

1.7 Rapid Solidification of 2-14-1 Alloys

The formation of a favorable magnetic phase, e.g. $Nd_2Fe_{14}B$, within the solidified matrix is a direct result of the amount of undercooling in the $MRE_2Fe_{14}B$ alloy, for example $[Nd_{0.45}(Y_{0.66}Dy_{0.33})]_{2.3\text{-}0.1}Zr_{0.1}(Fe_{12.5}Co_{1.5})_{14}B+Ti_{0.02}C_{0.02}$. It is anticipated that the solidification path for this alloy will likely resemble the dashed line in Figure 7a, a vertical isopleth of the Dy-Fe-B ternary phase diagram. This phase diagram was suggested [39] to be the most probable map to follow based on the relative amount of phase equilibrium information known, as compared to Nd-Fe-B, e.g. results showed that it retained a high melting 2-14-1 phase at 1280°C [40]. It will be shown later that the $MRE_2Fe_{14}B$ alloy also exhibits a comparatively high melting magnetic phase, consistent with the heavier rare earth elements. From the liquid state, the primary phase to solidify under equilibrium conditions

would be the Dy_2Fe_{17} phase, if Figure 7a is assumed to apply. Yet, rapid solidification of the melt can extend the choices, as kinetics is considered, and the predominant phase to form can be the peritectic $Dy_2Fe_{14}B$ line compound.

Actually, this is a likely case, as the only phase to consume B from the melt is the 2-14-1 according to the Dy-Fe-B diagram. If the solidification path were to follow the dashed line in Figure 8a, a vertical isopleth of the Nd-Fe-B ternary phase diagram [41], it is possible for B to be consumed by the $NdFe_4B_4$ phase in conjunction with the 2-14-1 phase, given sufficient undercooling and the right solidification conditions, e.g. local boron enrichment. In Nd-Fe-B compositions containing greater than 77at% Fe, a considerable amount of undercooling is needed in order to suppress the formation of α-Fe, a soft magnetic phase. Conversely, if the composition moves toward the rare-earth rich zone (<77at% Fe), there is an increased probability of forming a low melting RE-rich phase. As pointed out earlier, the drawback of the RE-rich phase is its vulnerability to oxidation and corrosion. Ideally, rapid solidification would provide a direct route to forming the 2-14-1 phase in either system given the original liquid composition is close to stoichiometric 2-14-1 and the required undercooling level is achieved.

If the cooling rate is insufficient to form an amorphous structure and or directly form the 2-14-1 invariant line compound, it is conceivable that the solidification path of the MRE-Fe-B alloy would demonstrate multiple phase formation, as illustrated in Figure 7b. The first phase to form would be Dy_2Fe_{17} or MRE_2Fe_{17}, according to Figure 7a, since its phase field is the highest melting at the indicated composition. Nucleation of the line compound $MRE_2Fe_{14}B$ would be the next likely phase to develop around the 2-17 phase as local enrichment of boron in the liquid phase competes during solidification, driving out the possibility of α-Fe formation. Subsequent cooling of the alloy requires solid state diffusion to maintain a steady flux of RE constituents and Fe to the solid-liquid interface. However, since solid state diffusion is too sluggish to sustain growth of the $MRE_2Fe_{14}B$ phase and the liquid composition is continually fluctuating, it is possible that other phases could form such

as MRE_1Fe_3, $MRE_1Fe_4B_4$, MRE_1Fe_2, or even the low melting Nd-rich phase until final solidification is complete.

a)

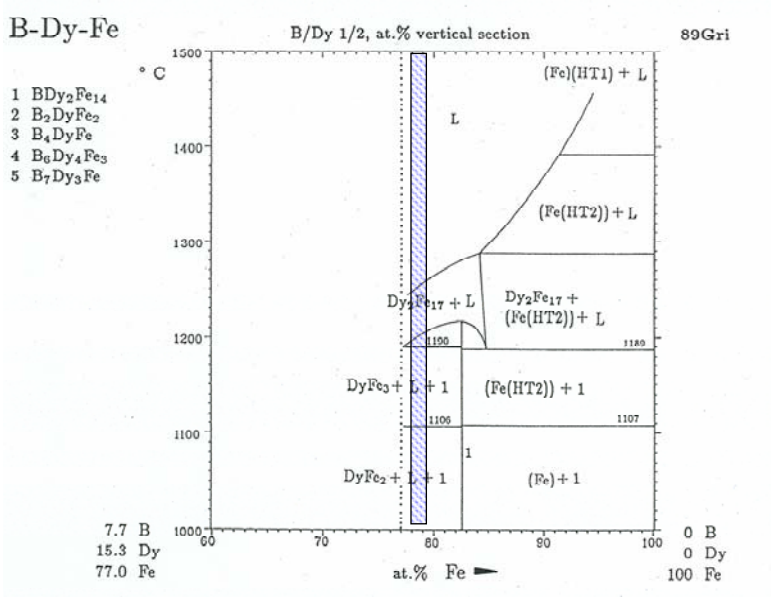

b)

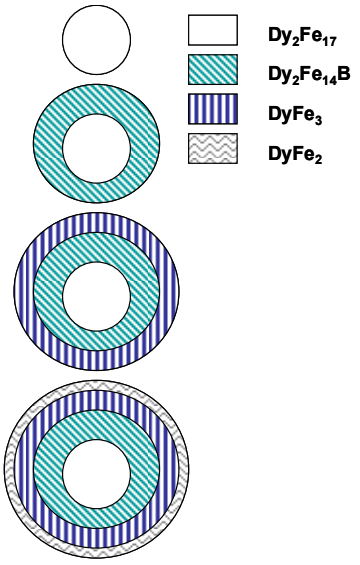

Figure 7: (a) Isopleth of B-Dy-Fe phase diagram; (b) Idealized illustration of phase selection during equilibrium solidification according to associated B-Dy-Fe diagram.

a)

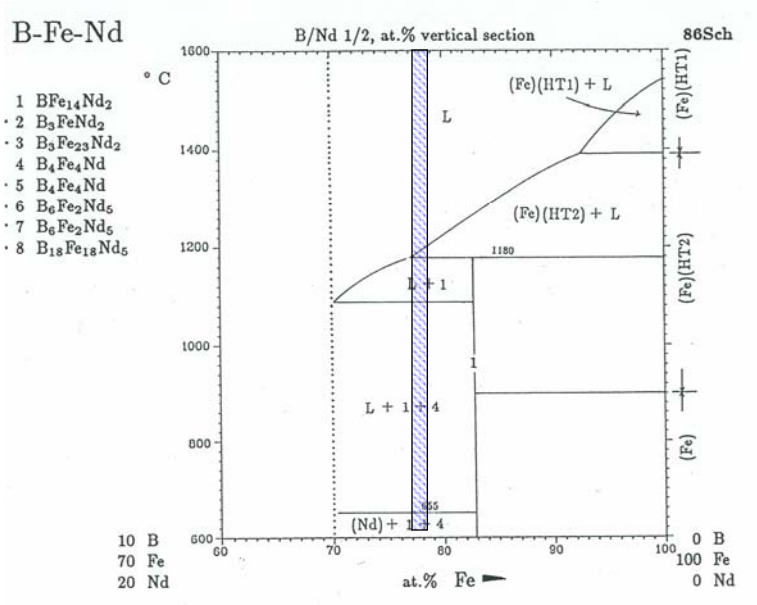

b)

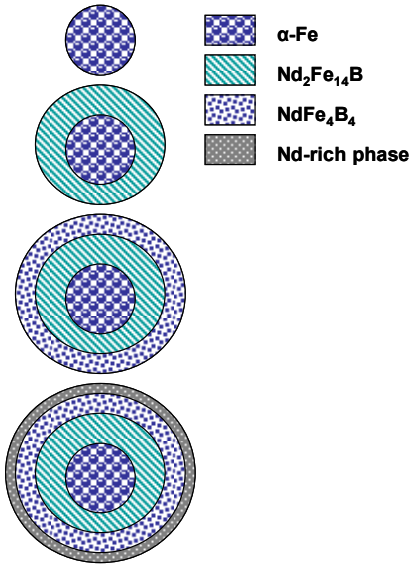

Figure 8: (a) Isopleth of B-Fe-Nd phase diagram; (b) Idealized illustration of phase selection during equilibrium solidification according to associated B-Fe-Nd diagram.

Consideration of the other prevalent $RE_2Fe_{14}B$ constituent, Y, solidification path is also necessary to discern possible phase formation upon rapid solidification. The B-Fe-Y ternary isotherm [42], Figure 9, reveals a completely solidified alloy at 800°C, with similar non-ideal compound formation if the alloy is off 2-14-1 stoichiometry (indicated with a dot), such as Y_2Fe_{17} and YFe_4B_4. These similarities in possible phase formations suggest that the ideal

solid solution behavior of the $MRE_2Fe_{14}B$ is a promising approach for obtaining desired magnetic properties.

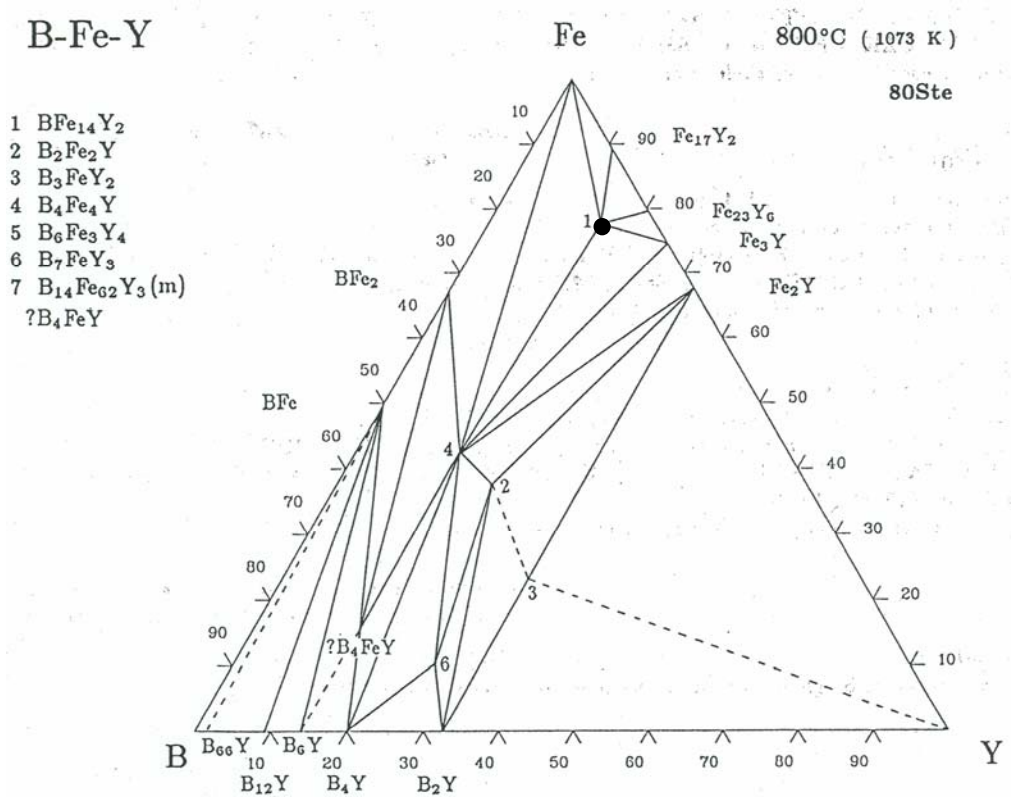

Figure 9: 800°C isotherm of the B-Fe-Y ternary phase diagram. Stoichiometric $Y_2Fe_{14}B$ is indicated by the black dot at 1.

1.8 Commercially Available Types of 2-14-1 Magnets

Currently, large-scale manufacturing of fully aligned-sintered and isotropic (unaligned) nanocrystalline $Nd_2Fe_{14}B$ magnets is carried out to satisfy technological needs based on performance demands and intended environment of each application. The following description explains and contrasts the main differences of each processing route and the inherent product characteristics.

1.8.1 Aligned Sintered Manufacturing Method

Typical processing routes for obtaining the highest energy product for $Nd_2Fe_{14}B$ compounds are based on a liquid-phase sintering mechanism [8][43]. A chill cast ingot of the alloy is infused with hydrogen gas to promote hydrogen decrepitation (HD), a method that causes the alloy to break into fine particles, whose size is a function of Nd-rich phases distributed around 2-14-1 grains. Hydrogen, which is readily absorbed at the surface, quickly diffuses through the bulk of the ingot within the atomic structure causing expansion at the Nd-rich phase and a considerable amount of stress, which is responsible for the fragmentation. Further reduction into a single-grain particle size, down to an average of 3-6μm [3], is achieved through a comminution step with mechanical crushing such as ball or jet milling. This procedure is carried out in an inert atmosphere, typically Ar, to protect the freshly created surface area from damaging oxidation. The particles are subsequently collected and aligned magnetically in a 10-30kOe field during uniaxial compaction with the alignment direction perpendicular to the pressing. The green compact is then heated between 1,035°C and 1,155°C in a vacuum, which removes the hydrogen and allows for the low melting Nd-rich phase to assist in liquid-phase sintering of crystallites of 2-14-1 phase.

Immediately after the sintering stage, the densified compact is rapidly quenched to prevent segregation and formation of magnetically soft phases, such as Nd_2Fe_{17} or α-Fe. A solid-state anneal is required to optimize the final microstructure and to relieve the material of cooling stresses [3]. The post-sintering heat treatment is done at a temperature below the eutectic melting temperature of the Nd-rich phase, 655°C, yet high enough to encourage solid-state diffusion for "smoothing" of the grain boundaries of the 2-14-1 phase to inhibit reverse domain nucleation. The final compact, once machined to shape, is eventually "hand placed" within its designed configuration and magnetized to saturation, M_{sat}.

The fully dense sintered $Nd_2Fe_{14}B$ magnets possess the highest energy product per volume at 54.2 MGOe, achieved through optimized processing conditions [6]. However, several drawbacks are associated with the sintered form. These magnets require delicate machining

and surface finishing to match final dimensions for their intended application. The brittle nature of the alloy makes the machining step difficult and often much material is wasted in obtaining the desired shape and size, creating an increase in cost. Also, the presence of the Nd-rich intergranular boundary phase is highly susceptible to corrosion in environments with increased humidity. As mentioned previously, the formation of $Nd(OH)_3$ not only reduces the effective intergranular region, but also liberates $3H^+$ leading to very aggressive hydrogen decrepitation. Further processing to encapsulate the sintered magnets with either a sacrificial metallic coating or epoxy resin is then beneficial (even a necessity) for any proposed application.

1.8.2 Isotropic Nanocrystalline Manufacturing Methods

1.8.2.1 Melt Spinning

Free-jet chill-block melt spinning is used as a practical alternative to ingot casting, with melt spinning being the primary alloy design processing technique used during this research, see Figure 10 [44]. The molten alloy can be rapidly solidified upon contact with the rotating water cooled Cu wheel at cooling rates as high as $10^{6\text{-}7}$K/s at the upper wheel tangential speeds. The resultant microstructure is a function of several processing parameters as well as alloy characteristics which ultimately determine the rate of heat transfer and hence the rate of solidification, as previously mentioned. These factors include the ejection and chamber pressure, diameter of crucible orifice, distance of crucible from the wheel, wheel speed, melting temperature of the alloy, the induced superheat, thermal conductivity of the melt, and heat capacity of the alloy [45].

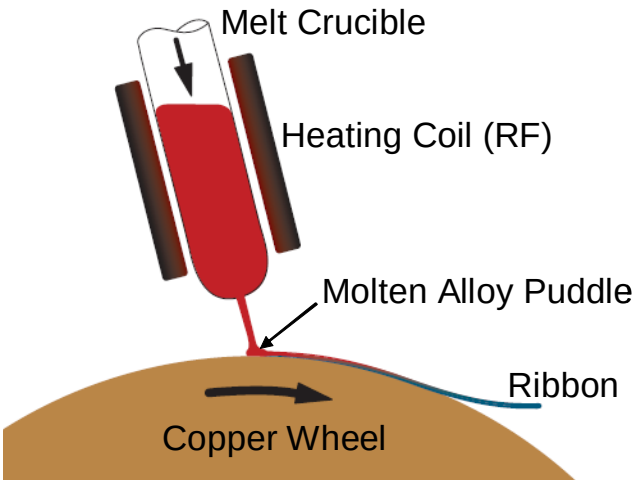

Figure 10: Free-jet chill-block melt spinning schematic.

Melt spinning utilizes the conductive nature of the chilled rotating Cu wheel to extract heat (unidirectional) through the thickness of the ribbon. Upon leaving the Cu wheel, the ribbon undergoes convective cooling to a stagnant atmosphere allowing for a reduced solidification rate in unsolidified portions or annealing of the initial solidified region. At high wheel speeds, liquid in contact with the wheel surface will be cooled below its melting point and can continue on as a liquid for some distance before nucleation occurs. This allows for substantial undercooling of the melt and transformation into an amorphous structure. At optimum wheel speeds during melt-spinning, elevated quench rates are capable of producing an ideally homogeneous microstructure consisting of fine nanocrystallites dispersed within an amorphous matrix [46][47].

Melt spinning is commercially utilized due to its broad range in cooling rates, with the ability to supply overquenched uniform microstructures in a variety of alloys. However, the main deficiencies of this processing technique arise from the shape of the solidified product, i.e. the ribbon form reduces the fill factor and increases viscosity for polymer bonded permanent magnet processing due to the geometry. This geometry effect will be discussed in a following section. Therefore, melt spun ribbons must undergo a crushing or milling step to reduce the particle size into a preferred equiaxed shape.

1.8.2.2 High Pressure Gas Atomization (HPGA)

Close-coupled discrete-jet gas atomization processing may be developed into a beneficial replacement for melt spinning in producing rapidly solidified RE-Fe-B nanocrystalline particulate for bonded magnet production. The high energy shearing mechanism of the high velocity gas (Mach 2-3) provides the necessary energy to break-up the melt stream into fine, spherical particles immediately upon exiting the pour tube, see Figure 11 inset. Considerable research has gone into making the HPGA system more efficient and capable of increasing the yield within a desired particle range, all while maintaining a low standard deviation [48]. It has been shown through previous research by Buelow *et al* [49][24], that this processing route can indeed be used as a viable alternative for mass production of magnet alloy powder. However, the difference in heat transfer mechanisms, with respect to melt spinning, and the geometric limitations to heat flow of spherical droplets may reduce the overall yield that is capable of exhibiting an optimal nanocrystalline or amorphous microstructure. Through certain alloy additions, e.g. the addition of Zr, aimed at improving glass formability, the idea has been to increase the range of particle sizes with kinetically suppressed nanocrystalline microstructures, allowing for greater yield control.

Due to distinctions in heat transfer mechanisms and directionality during solidification, observed morphologies between melt spun ribbon and gas atomized particles can be considerably different. HPGA particles primarily experience convective cooling induced by the high velocity gas wherein particle surfaces can be extremely undercooled and the interior can exhibit increased nucleation and crystallization [39]. Due to mote isolation effects during atomization, the number of available heterogeneous nucleation sites per particle drastically decreases with a decrease in particle size distribution, resulting in a high yield of undercooled particles. The smallest particles are capable of experiencing extreme undercoolings, forming a homogeneous microstructure consisting of fine nanocrystallites dispersed within an amorphous matrix or completely amorphous particles, depending on magnet alloy composition.

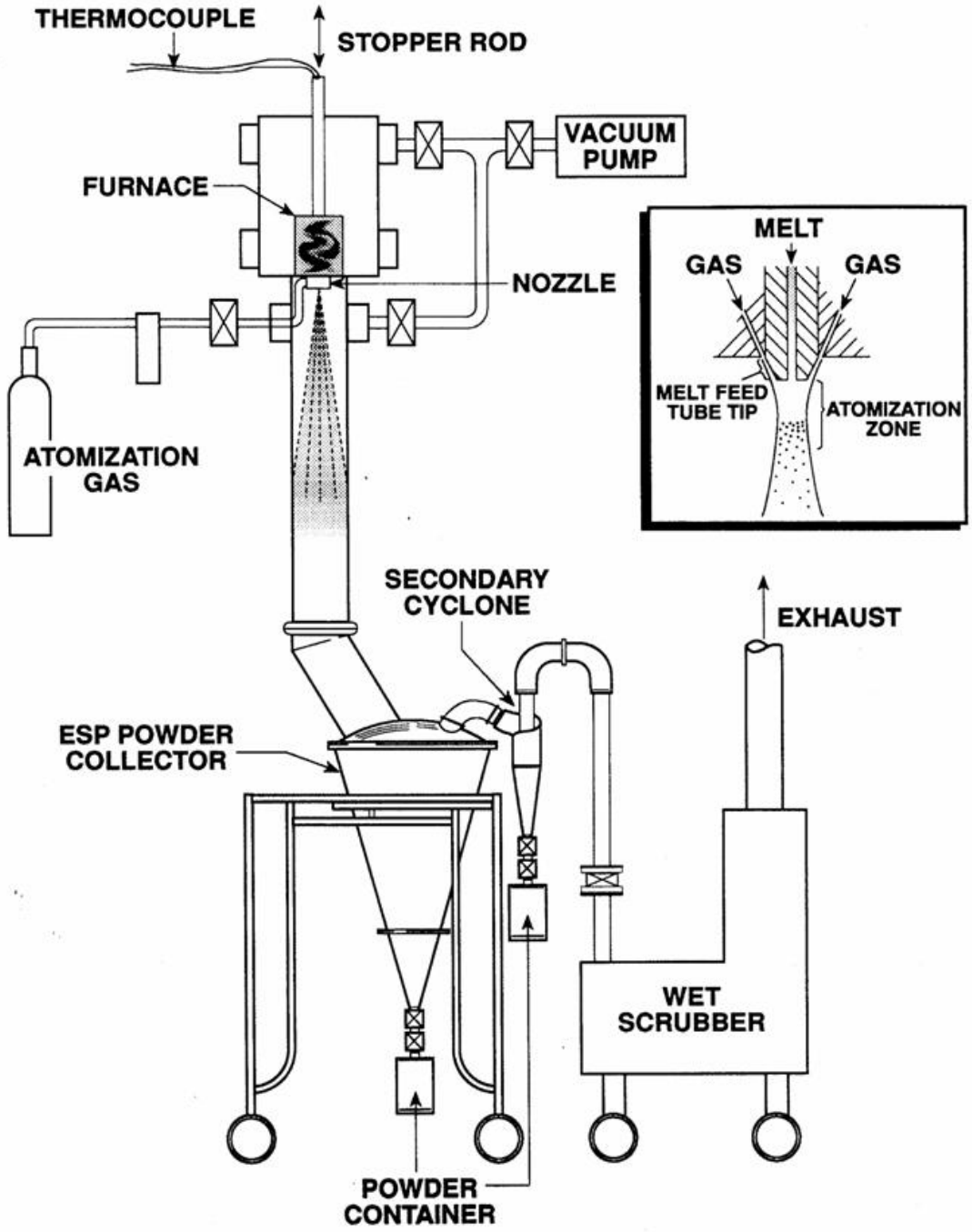

Figure 11: High pressure gas atomization schematic with (inset) close-coupled nozzle configuration.

1.9 Protective Coatings and Surface Passivation Mechanism

In order to fully prevent oxidation or corrosion of the magnetic material, a protective coating can be applied to the finished magnet, generally a sintered magnet. Common methods include a nickel-plated coating with an effective thickness of 10-15μm, an ion vapor deposited aluminum layer of about 10μm, or an epoxy-type coating of approximately 20-30μm in thickness [13]. These coating techniques for sintered magnets can be costly and require additional process steps, which ultimately drive up the price of the magnet. Alternatively, other methods aim to coat the magnetic particles prior to the consolidation process and are commonly referred to as bonded magnets since the magnet is physically held together by an organic matrix in comparison to a metallic bond found in sintered magnets. Particles may be mixed with an epoxy resin solution, or other organic resin, which is added in small concentrations (1-3wt %) sufficient to uniformly coat each particle without leaving excess resin in the matrix. The resin coated particles are (cold or hot) pressed to green density and then cured to full density. There are numerous modifications to the organic coating method, with multiple types of organic precursors which enhance surface wetting behavior and either volatilize or contribute to the final surface coating, based on the type of organic used [16]. Though the epoxy coatings are themselves limited in their range of operating temperature, they can provide efficient means to protect against chemical and mechanical degradation.

Current surface coating methods, such as proposed by Guschl *et al* [50] and Brown *et al* [51] make use of an organic micro-dispersion route to coat melt spun particles, of flake geometry, with a polymer prior to the molding process, which was shown to reduce flux aging loss at increased temperatures up to 189°C. However, there is no mention of performing the same coating process on atomized spherical particles, the ideal shape for injection and compression molding. In an attempt to control solidified particle surface chemistry during HPGA, a reactive gas, nitrogen trifluoride (NF_3), has been injected into the atomization chamber in the current effort to form highly stable and thermodynamically favored rare earth fluorides (REF_3) and rare earth oxyfluorides (REOF) [52] on the first several monolayers of the

spherical particles. Passivation of particle surfaces in situ may provide a unique opportunity to bypass any additional processing steps prior to the molding process itself, as well as providing the necessary oxidation barrier during further handling, especially important for protecting ultrafine (dia. <20μm) powders.

The concept that fluorine may provide a protective metallic fluoride layer stems largely from research performed in the early 1900's focused on isolating pure fluorine gas in bulk quantities. The procedure, initially developed by Henri Moissan in 1886, involved isolation of the element by electrolysis of anhydrous hydrofluoric acid mixed with potassium hydrogen fluoride with pure fluorine gas being a byproduct. Modification of his procedure utilized graphite electrodes in a molten potassium hydrogen fluoride bath encased within a copper constructed apparatus. It was noted that "formation of a protective layer of metallic fluoride prevents further attack on the inner surfaces of the cell," [53]. In addition to the separation of elemental fluorine, extensive investigation into producing high purity rare earth elements at Ames Laboratory in the 1950's established preparation methods for producing rare earth fluorides (REF_3) from their native oxide forms [5][54] as described in equation 9 with water vapor as a byproduct. The fluoride compound was described as being quite stable in air and possessed fair packing density.

$$RE_2O_3 + 6HF \overset{700^\circ C}{\rightarrow} 2REF_3 + 3H_2O \tag{9}$$

REF_3 could then be easily reduced to pure RE by reaction with calcium through a metallothermic process. One such preparation method, still used today, employs a rotary-bed design where high-purity RE_2O_3 (RE = Y, Nd, Dy for example) was placed within a rotating Inconel tube furnace, heated to 700-750°C, and hydrofluorinated by passing HF gas through the system. Conversion rates of 99.90-99.98% were achievable and the REF_3 compound was produced in tonnage amounts [54]. Interestingly enough, a study on bulk formation of FeF_3 by thermite reduction processing concluded that anhydrous hydrofluorination was not an efficient conversion method with iron. Schmidt and Peterson found that "a ferric oxyfluoride

layer formed on the outer layer of the oxide particle and serves as an inhibitor for further diffusion of the hydrogen fluoride gas into the oxide particle thereby slowing or stopping the reaction completely," [54]. However, in contrast to the current research presented in this work, the purpose is not to fully convert the whole volume of the material, but only to grow a controlled fluoride layer on the first several monolayers of the particle surfaces, thereby protecting the bulk of the volume from oxidation. To accomplish this, a safer and less aggressive technique uses NF_3 gas as the source of fluorine.

NF_3 gas is commonly used as an etching and cleaning agent in the semiconductor industry, since its only byproducts are gaseous, mostly consisting of N_2, O_2, NO_x's, and the corresponding solid fluoride [55]. It is known that fluorine, being the most electronegative element, will react with all metals to form metallic fluorides at increased temperatures, forming passive films which are capable of resisting further reaction with fluorine [56]. It has been shown that these films are quite adherent and will not easily detach from the substrate by mechanical flexing or thermal shock. More importantly, exposure to humidity results in hydrated metal fluorides which enable secondary fluorination upon re-exposure to fluorine at the expense of oxide films [57]. At low temperatures (150-300°C), NF_3 reacts slowly as the activation energy needs to be overcome through increased heating to completely dissociate the gas into its components. At temperatures above 500°C, reaction with any metallic surface in its vicinity will occur readily and possibly explosively if the reaction is not kept under control [58], e.g., by dilution.

A study on fluorination of rare earth metals, performed by Rakov *et al*. [59], revealed a difference in rate of the reactions for each rare earth present in this system. Yttrium has a moderate rate of fluorination, while dysprosium and neodymium yield a slightly lower rate. To further support this result, Table II provides the heats of formation (ΔH_f) of compounds that could form during the in situ passivated HPGA process. Thermodynamically, YF_3 would be the most stable fluoride, while DyF_3 and NdF_3 are comparatively less stable, yet highly possible given the relative concentrations present. Also reported are the heats of formation for possible oxide compounds, noticeably higher than corresponding fluorides.

However, these values only take into account the thermodynamic driving force for formation of likely compounds and previous research, already mentioned, suggests the fluoride structure will be the most probable to form under HPGA conditions, where the oxygen partial pressure is minimized and the availability of fluorine ions is boosted.

Table II: Heats of formation values for possible reactions of in situ passivation during HPGA

Compound	ΔH_f (kJ/mol) 298 K	Reference
DyF_3	-1692.0	[60][61]
NdF_3	-1679.4	[60][61]
FeF_3	-989.6	[60]
YF_3	-1719.5	[62]
Dy_2O_3	-1864.5	[63]
Nd_2O_3	-1809.2	[63]
Fe_3O_4	-1114.9	[64]
Y_2O_3	-1906.9	[63]

1.10 Evolution of a Fluidized Bed for Controlled Fluorination

Original development of a gaseous fluidized bed apparatus was established by M. Anderson [65] in an effort to passivate gas atomized $LaNi_{4.75}Sn_{0.25}$ particulate for battery applications. This was accomplished through means of a gas-solid surface reaction with NF_3. Formerly, the concept of "F-treatment" (F referring to fluorine) was developed under work by S. Suda et al [66] as an aqueous-based approach to form a thick, 1-2μm, layer of LaF_3. Their effort aimed at preventing degradation of the hydrogen storage alloy from oxidation and corrosion by means of forming an anticipated adherent and protective fluoride coating.

The objective, as proposed by Anderson, was the implementation of the gas-solid phase reaction as an alternative processing step to the aqueous-based method. As a direct result of his work, it was concluded that the fluoride layer commonly fractured and spalled due to expansion and contraction during cyclic electrode charging and discharging, as was also the case with the aqueous method. The spallation of the protective layer exposed clean surfaces that quickly oxidized, thus undermining the purpose of the fluoride layer. Regardless of this result, however, a successful approach to gaseous surface fluorination was developed. The

minimal success in protecting the alloy from oxidation and corrosion is suggested to be characteristic of the alloy and more importantly the nature of its intended performance. This realization permits other alloys which require surface passivation, yet are not thermally or mechanically cycled, to be tested in a similar manner. Rare earth based alloys, being highly susceptible to severe oxidation and corrosion are suitable alloys for testing since protective coatings are usually preferred and fluorine preferentially forms compounds with the rare earth elements in controlled atmospheres. Thus, the concept of fluorinating the desirable $Nd_2Fe_{14}B$ permanent magnet alloy, an alloy generally exhibiting unwarranted oxidation and corrosion behavior, evolved as an industrial approach to protecting fine particulates processed via HPGA.

Initial fluorination methods on the hydrogen storage alloy, as tested by Anderson, centered on a continuous and pulsed NF_3 flow into a heated (210°C) reaction chamber. The continuous flow technique resulted in excessive fluorination and inconsistent coating as indicated by an elevated exothermic reaction and visual inspection and was therefore not pursued. The pulsed flow method was designed to maintain increased control over the extent of the surface reaction and was also monitored by local temperature measurements. Also, the Ar gas flow needed to fluidize the particulates was established as a result of his work at a flow rate between 300-500sccm for a sample size of 8-10g.

This previous setup was systematically tested in the same manner on the magnet alloy to develop a fluoride coating on both atomized and melt spun particulate. Periodic assessment of the pulsed method approach revealed insufficient coatings which were either incomplete or too aggressive. In order to better control the extent and uniformity of the surface reaction, a digital flow meter with precise control of NF_3 flow between 1-10sccm was installed [39] such that low concentrations (0.5-1%) of the reactive gas could be utilized. The idea being that a reduced concentration of reactive gas passed through the system, in a constant flow method, allows for even and controlled surface reaction. In addition, the mechanism of fluidizing the particulates to interact with the passing gas was modified by the addition of a magnetic stirring plate [39] which would agitate the particles instead of relying on gas flow

to levitate particles with high aspect ratios, i.e. flake morphology. Through these modifications, it was suggested [39] that the optimal parameters for forming a sufficient fluoride coating of 15nm could be achieved with 0.5%NF_3 concentration in 300sccm flowing argon at a reaction chamber temperature of 160°C.

The ability to reproduce much of those results proved to be fruitless, however. Therefore, this work aimed at better understanding the mechanisms involved during fluorination. To do so, more control over the atmosphere within the reaction chamber was established and a reduced concentration of NF_3 (0.05%) was determined to be more effective in understanding the extent of the reaction. The addition of an oxygen gettering furnace to the high purity Ar flow and incorporation of a vacuum pump to reduce adsorbed moisture and oxygen present within the reaction chamber prior to the heating stage resulted in a cleaner starting atmosphere. Also, the NF_3 cylinder was replaced with a 10%NF_3 + 90%Ar mixed gas cylinder providing the reduced concentration of NF_3 in the reaction zone.

In the effort to optimize the reactive gas passivation mechanism, the use of a scaled-up modified fluidized bed (built to accommodate ~30g samples) was initally utilized to perform coating experiments on small (10 grams) amounts of commercially provided flake (MQP-11-HTP). Initial runs were done at a low concentration (0.05%NF_3) of the reactive gas in order to gain more control over the extent of the surface reaction. Increased set reaction temperatures, i.e. 160, 165, 170, 175°C, etc. were expected to improve reaction kinetics and allow for a systematic study on the effectiveness and completeness of the reaction. Thermogravimetric analysis (TGA) on fluorinated flake, generated from the constant flow fluidized bed procedure, gives insight into the change in rate of oxidation at increased temperatures for the same alloy as a function of fluoride treatment. This analysis will lead to an optimized surface passivation treatment with the fluidized bed apparatus. Optimized parameters will initially be used to mass produce fluorinated flake (30g samples) for production of polymer bonded magnets. These bonded magnets are then to be STILT and LTILT tested by Arnold Technologies for direct comparison to untreated magnet material which have been environmentally tested.

A primary reason for determining the optimized parameters in the "steady-state" fluidized bed is to use those results as a foundation for fluorination of fine particulates while in flight during the atomization process. Understanding the steady-state approach (in comparison to atomization) should give insight into the ideal parameters, e.g. temperature zone of injection and required NF_3 concentration, necessary for successful in situ fluorination during chaotic atomization processing. In order to monitor the reaction taking place, a residual gas analyzer (RGA), discussed in more detail in a following section, was used to detect and record specific gas evolution within the atomization chamber during the run.

It is suggested that a simple model can be applied to the reaction occurring, equation 10. This preferential reaction results in N_2 evolution, which is monitored through the use of the RGA unit that is capable of identifying gases with concentrations as low as 10^{-14} Torr.

$$2NF_{3(g)} + 2RE_{(s)} \overset{+Heat}{\Rightarrow} 2REF_{3(s)} + N_{2(g)} \tag{10}$$

Alternatively, it is possible and more likely that rare earth oxides have formed prior to the passivation process and incorporation of NF_3 into the chamber would actually result in equation 11. Provided this equation is more feasible, monitoring O_2 in conjunction with N_2 would be another indication as to the extent of the fluorination reaction.

$$4NF_{3(g)} + 6RE_2O_{3(s)} \overset{+Heat}{\Rightarrow} 12REOF_{(s)} + 2N_{2(g)} + 3O_{2(g)} \tag{11}$$

Considering the rate of fluorination of rare earth metals and its exothermic behavior, the reaction would be self sustaining after overcoming initial activation energies. It is conceivable that initiating a fluorination reaction at a high temperature could completely consume fine particulates instead of producing an even film on the surface, resulting in a "burned" condition. However, atomized particles are continually cooled by the atomization

gas as they move downstream within the chaotic atmosphere of the spray chamber. Also, by placing the injection halo in a warm zone within the chamber (cooler, but sufficient for promoting the preferred reaction) and by keeping NF_3 concentrations low, the extent of reaction is kept to a minimum in an effort to optimally passivate the surface.

1.11 Polymer Bonded Magnet Significance

For producing magnetic components in complex shapes with high accuracy at increased production rates, injection and compression molding have become ideal manufacturing methods, where magnetic particulate is combined with a polymer binder and injected into a cavity as a finished magnet shape. Current processing routes for melt spun particulate require communition of the ribbon before it can be utilized for bonded PM's, adding processing steps. The spherical geometry of gas atomized particles is more ideal for bonded magnet processing when compared to the tabular or disk-like shape of crushed melt spun ribbon. Based on powder metallurgy principles, a higher loading fraction of spherical powders can be achieved at lower injection viscosities as seen in Figure 12 [67], thereby reducing the required injection pressures and lowering overall processing costs. As noted by other research [51], the atomized spherical powders are the most ideal for injection molding based on its low apparent viscosity when mixed with a polymer binder.

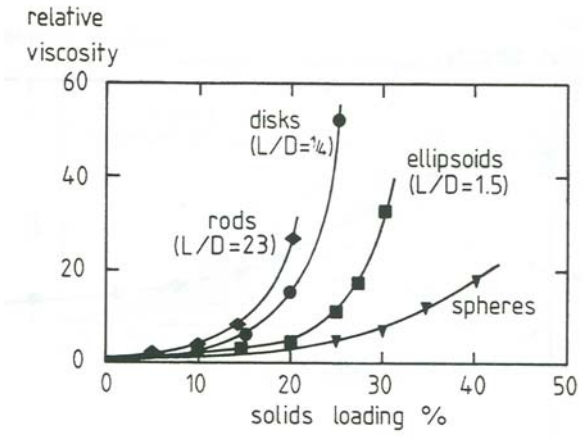

Figure 12: Particle shape effect on relative viscosity with increased solids loading.

Through increasing the relative loading fraction of magnetic material, a higher $(BH)_{max}$ may be reached over the current bonded magnet values attained with flake particulate. By means of multimodal spherical particle packing, a higher fill factor, *f*, may be obtained which ultimately increases the available energy per unit volume according to equation 8 [68].

$$[(BH)_{max}]_{bonded} = f^2 [(BH)_{max}]_{sintered(isotropic)} \quad (8)$$

Bonded magnets will inherently have a reduced $(BH)_{max}$ due to the presence of the polymer matrix which acts as an inactive volume between particles. However, through increasing the fill factor, bonded magnets can approach 25% to 50% $(BH)_{max}$ of their isotropic sintered fully dense counterparts [3]. Aside from the drawback in energy product, bonded magnets provide an improvement in mechanical stability as well as corrosion and oxidation resistance. This can lead to an extended service lifetime and a broader application base, especially in harsh environments. From these standpoints, isotropic bonded magnets have an advantage over sintered magnets which are typically brittle and susceptible to severe corrosion in particular applications. Current research [69][70][50][71] with bonded magnets has made use of the high temperature polymer bonding material, polyphenylene sulfide (PPS), which possesses excellent chemical resistance and greater structural integrity as opposed to current industrial choices, nylon and epoxy. Table III [72] provides melting temperatures of typical polymers used for bonding purposes. The melting temperature for PPS is noticeably higher and thus, greatly enhances thermal stability of the magnet in applications at 200°C. Magnets produced with a "low temperature" polymer will otherwise degrade rapidly due to heat distortion effects and loss of the protective coating.

Table III: Typical polymers used for bonded magnet production.

Polymer	Melting Point (°C)
Epoxy	Thermoset ~ 150
Nylon, polyamide-12	160-209
Nylon, polyamide-6/12	195-219
Nylon, polyamide-6	210-220
Polyphenylene sulfide (PPS)	285-290

To produce PBPM's with enhanced $(BH)_{max}$ values, the fill factor must be increased as stated above and the magnetic material properties must be optimized. To accomplish both requirements, HPGA offers the best solution for providing a range of particle sizes for multimodal particle packing and can provide the necessary cooling rate to form a highly refined grain structure or partially amorphous particles, allowing for microstructural control. HPGA particles below 15-20μm [39] and possibly larger particles are capable of exhibiting average cooling rates similar to that of ribbon spun at moderate wheel speeds. This study is intended to show that these particles can demonstrate microstructural and magnetic characteristics that approach the melt spinning processing route due to recent alloying behavior.

2. METHODOLOGY

2.1 Melt Spinning (MS)

Alloy design iterations were accomplished with a small scale, custom built free-jet chill-block melt spinner, using wheel speeds of 13 and 16m/s. This lab-sized setup allows for a short turn around time in alloy production while providing sufficient material property information. Melt spun ribbon samples were prepared by arc-melting ingots of the initial composition in an Ar atmosphere. Ingots of approximately 8g were subsequently induction melted to a superheat of 1370°C in a quartz crucible in 0.03 MPa of ultra high purity (UHP) He gas and then ejected onto the rotating Cu wheel. Portions of the as spun ribbon were annealed in Ar at 700°C for 15 minutes.

2.2 High Pressure Gas Atomization (HPGA)

All magnet alloy powder preparation was performed at the Material Preparation Center (MPC) of Ames Laboratory. A charge weighing 4.5kg was produced for each atomization experiment by plasma arc melting constituent elements together in a preferred alloying fashion [25]. Pre-alloyed compositions were induction heated in an alumina crucible to a superheat of 1550°C, held for 3 minutes to insure complete homogenization of the melt temperature and composition, and subsequently high pressure gas (He) atomized in a backfilled argon atmosphere spray chamber. The atomization process utilized a close-coupled nozzle developed at Ames Laboratory which allows a high velocity gas shearing mechanism to break up the melt into fine spherical particles. Ultra high purity He gas with a supply pressure of 800psi was used as the atomization gas for all (2) runs. Powder removed from a primary cyclone collector was sieved in an ambient environment using ASTM standard sieves into size distributions of <106µm, +75-90µm, +63-75µm, +53-63µm, +45-53µm, +38-45µm, +32-38µm, +25-32µm, +20-25µm, and <20µm. Air classification was used to separate the <20µm particles into +15-20µm, +10-15µm, +5-10µm, and <5µm

distributions. A small secondary cyclone powder collector can was opened within an argon glove box containing approximately 0.1-0.3ppm oxygen to obtain samples for surface characterization, including XPS, TGA, and gas fusion analysis (see following sections for description). These samples were considered unexposed.

2.3 Magnetically Stirred – Fluidized Bed Apparatus

A small, modified fluidized bed, characterized by the addition of a magnetic stirring plate to provide the turbulent mixing behavior instead of gaseous levitation, was used to fluorinate particle surfaces in a controlled environment. The loaded and sealed reaction chamber (fabricated out of Alloy 400 and Alloy 600), as seen in Figure 13, was evacuated twice at the beginning of each experiment to reduce adsorbed moisture and then backfilled with gettered high purity Ar. Gettered Ar was constantly flowed through the system at 300sccm for the entirety of the experiment. The chamber was heated with two Chromalox™ band heaters up to a specified temperature (between 170-200°C currently), with a type-K thermocouple positioned directly inside the chamber to monitor particle temperatures. Upon stabilization of powder temperature, the 10%NF_3+90%Ar gas cylinder was opened and gas flow into the chamber was controlled with an electronic flow meter to provide a calculated 0.05% volumetric flow concentration of NF_3 inside the reaction vessel. The atmosphere in the chamber was monitored downstream with a residual gas analyzer, detecting evolution of N_2 and O_2 – byproducts of the surface reaction. The fluorination experiments were completed after 1 hour at temperature and NF_3 flow, and then allowed to return to room temperature via gettered Ar purging.

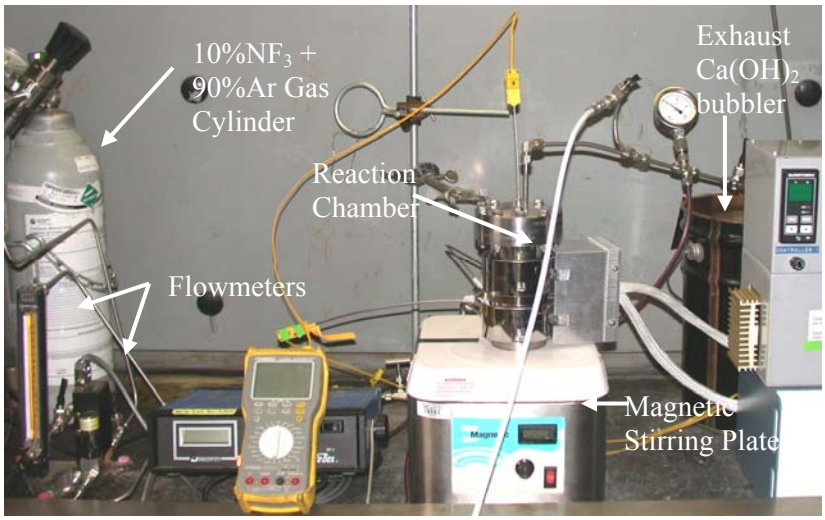

Figure 13: Experimental fluidized bed apparatus located within a fume hood with the main features pointed out.

2.4 Reactive Gas Injection – HPGA

Application of NF_3 into the gas atomization chamber was accomplished through the use of a halo placed downstream from the atomization zone, shown in Figure 14. A mixed gas cylinder of 25% NF_3 and 75%Ar supplied the gas for injection at a pressure of 75psi and was calculated to be about 1% of the total gas flow within the chamber. The halo is located in a region where gas temperature has been measured to be approximately 200°C, a sufficient temperature to encourage fluorination of rare earth elements without the possibility of allowing an accelerated exothermic reaction. An AMETEK residual gas analyzer (RGA) was used in conjunction with the experiment to monitor the concentrations of specific gas species within the atomization spray chamber, along with type-K thermocouples (TC) for observing temperature trends in the system.

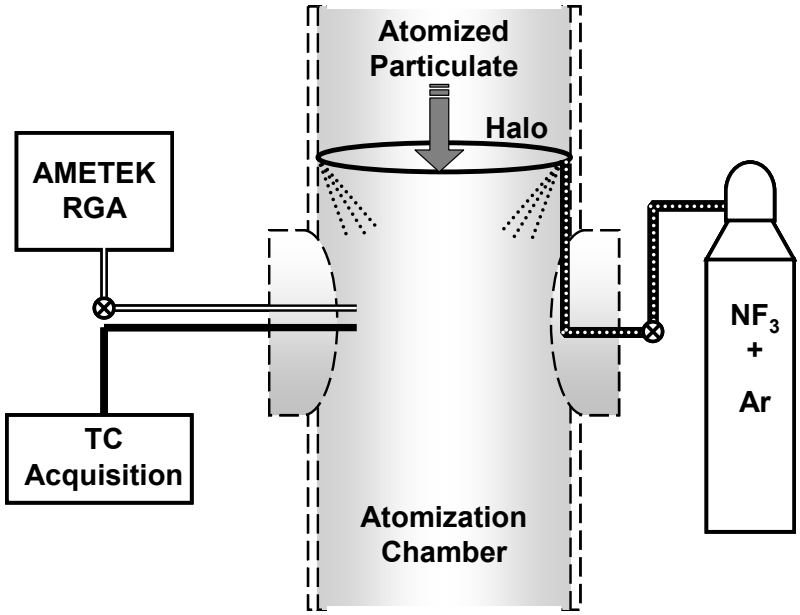

Figure 14: Schematic representation of reactive gas injection halo location in HPGA chamber.

2.5 Polymer Bonded Magnet Fabrication

Commercially provided powders of $MRE_2Fe_{14}B$ were blended with polyphenylene sulfide (PPS) at a loading fraction of 60vol% melt-spun magnet powder. Compression bonding of the magnet was carried out in an inert atmosphere to reduce oxidation during processing. The loaded die, as seen in Figure 15, was heated with a 120V, 400W Chromalox™ band heater to a temperature of 310-315°C and held for 20 minutes at temperature to ensure complete melting of the binder. The sample was compressed at a pressure of 6ksi and held at pressure for 5 minutes to encourage total wetting of the magnet particulate. Upon removal of heat, pressure was maintained until mold temperature was well below 200°C and then allowed to slowly return to ambient pressure. All compression molded samples were machined to final dimensions to obtain a permeance coefficient (P_C) of 2, as required for magnetic measurements.

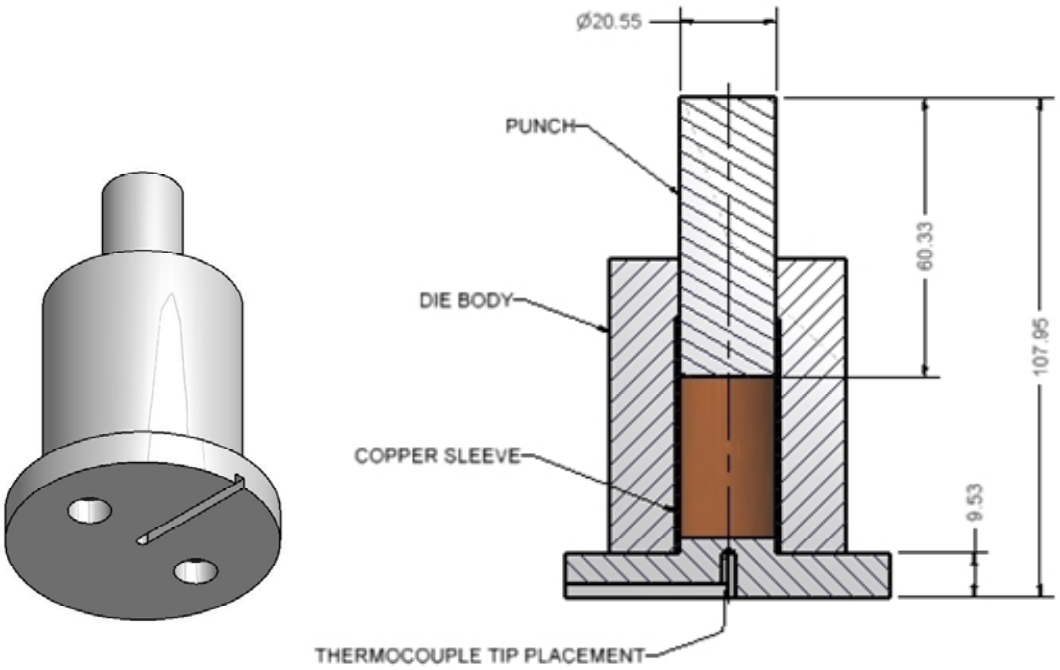

Figure 15: Schematics of compression bonded magnet die (measurements in millimeters). Interior of die is lined with a sacrificial copper sleeve. Sample temperature during bonding is monitored with specified thermocouple placement.

3. ANALYSIS TECHNIQUES

3.1 Scanning Electron Microscopy (SEM)

Powder size classifications were mounted in epoxy, polished with 400 and 600 grit paper in oil and then down to 6μm and 1μm with diamond oil suspension. Oil was used as the lubricant due to tendency of rare earth metals to hydrolyze in water. The 1μm polished surfaces were etched with a four part acid mixture containing nitric, acetic, phosphoric, and lactic acid diluted with methanol in a 2:3 ratio, 1ml of each acid – 6ml total methanol [39]. The mounted and etched samples were subsequently prepared for SEM imaging with gold sputter coating for 2 minutes. A JEOL 59101v SEM was used with a range of accelerating voltages from 5-15kV. Both secondary and backscattered imaging was performed for topological and chemistry analysis, respectively.

3.2 Transmission Electron Microscopy (TEM)

Transmission electron microscopy analysis was carried out by Yaqaio Wu using a Philips CM-30 TEM. The TEM provides a significant boost in resolution over SEM imaging and yields increased understanding of structural makeup through electron diffraction performed within the TEM.

3.3 X-Ray Diffraction (XRD)

X-ray diffraction was performed on ground ribbon and specified HPGA particle distributions with the use of a Philips X-ray Diffractometer and a Scintag X-ray Diffractometer, each using Cu Kα radiation. Typical runs were performed with a range of $20^{2\theta}$-$85^{2\theta}$ with a step of 0.02°.

3.4 Hysteresis Loops – SQUID Magnetometer/VSM

Magnetic hysteresis loop measurements were performed by Wei Tang using a Quantum Design MPMS SQUID magnetometer with a max applied field (H) of 5 Tesla. Field correction was applied by using a demagnetization factor of 0.333 for spherical geometries, giving a more exact internal field within the particles [4]. High temperature magnetization versus temperature curves were measured with a vibrating sample magnetometer (VSM) with a max applied field of 1 Tesla.

3.5 Residual Gas Analysis (RGA)

An Ametek Dycor Dymaxion Mass Spectrometer with a quadrupole mass spectrometer was used to monitor gaseous evolution and detection within the atomization chamber (as previously discussed) and fluorination bed apparatus. Gas was drawn from the atomization chamber through a 1/16inch capillary tube by means of a roughing pump. A small representative fraction of the gas is further drawn into the housing of the isolated spectrometer housing for analysis. The analyzer head has a range of 1-100amu detection with an enclosed ion source and a channel plate electron multiplier detector. A laptop PC was attached to the RGA system and ran the supplied software, Dycor System 2000. Labview was utilized by David Rehbein to simultaneously gather temperature and gas analysis at the same location within the atomizer in order to correlate temperature trends to possible reactions occurring within the chaotic atmosphere.

3.6 Gas Fusion Analysis

A LECO TC-436 nitrogen/oxygen determinator was utilized by Hal Sailsbury to perform gas fusion analysis on unexposed powder that was size classified to <45μm. Calibration standards were used before and after the tests to insure reliable results. Three experiments

were performed per sample to obtain an average value of oxygen concentration on the powder particle surfaces.

3.7 Thermogravimetric Analysis (TGA)

A Perkin-Elmer TGA HT7 was used for monitoring weight gain from oxidation of fluorinated and nonfluorinated particulate. Samples of approximately 50-60mg were heated from 50°C at 5°C per minute to 300°C and held for 20 minutes in flowing dry air at 20cc/min. This scheme was chosen based on the temperatures that are experienced by the particles during the polymer bonding step, where polyphenylene sulfide melts at about 285°C and flows readily above 300°C. Therefore, it is believed the wetting behavior of PPS as it melts will sufficiently coat the particles, cutting off any opportunity for continued oxidation above 300°C.

3.8 X-ray Photoelectron Spectroscopy (XPS)

XPS was performed by Jim Anderegg with a PHI 5500 Multitechnique system using monochromatic Al K_α excitation source and 4kV ion gun energy with a supplied current of 20ma. Depth profiling was based on a 190Å SiO_2/Si standard at an etch rate of 1nm/min. XPS was used to determine chemical composition and surface bonding structure on both atomized and melt spun particulate that had been fluorinated. In this technique, x-ray photons are used to excite surface atoms, producing an ejected characteristic electron. Through measuring the kinetic energy, KE, of the detected electron and applying the following relationship, equation 12, the binding energy, BE (which is distinctive to each element), can be determined. Where hν is the x-ray energy and Φ is the work function, typically <2eV.

$$KE = h\nu - BE - \Phi \tag{12}$$

This surface analysis works best on flat samples of reasonable size, >1μm. In the case of the atomized particulates, which are spherical, shadowing effects and unknown surface contours result in speculative qualitative results. However, it still provides general information on a collection of particles.

3.9 Auger Electron Spectroscopy (AES)

AES was performed by Jim Anderegg with a JEOL Jamp 7830F Field Emission Auger Microprobe using monochromatic Al K_α excitation source and 3kV ion gun energy and current of 20ma. Depth profiles were calibrated using a 1000Å SiO_2/Si standard with 10nm/min etch rate. This method is preferred for analyzing the surface of a single particle where the electron resolution is on the order of 10nm. Also, depth profiling is more accurate as surface curvature is less of an effect due to the higher resolution of scanned area.

3.10 Short Term (STILT) and Long Term (LTILT) Irreversible Loss Tests

The STILT is a measure of loss in room temperature magnetic flux output after short-term exposure to elevated temperatures. The procedure is carried out by fully saturating the magnet and measuring its initial flux level with a Helmholtz (integrating) Fluxmeter system. The magnet is placed in an open circuit and exposed to an elevated temperature for 1 hour, allowed to cool to 23°C, and then the flux output is re-measured. The LTILT is carried out in a similar fashion as the STILT, however it is only performed at one specified temperature (150°C) and held for extended periods of time at that temperature. The magnets are placed in an oven at constant temperature and periodically assessed to determine long term temperature exposure flux loss [73].

4. RESULTS

4.1 Melt Spinning

Initial alloy design iterations were performed with free-jet melt spinning at wheel speeds of 13 and 16m/s, see Table IV for compositions and associated nomenclature used in the subsequent results. It is noted that the compositions are kept the same as the wheel speed is the only variable altered in order to study the effect of a lower cooling rate on the solidification behavior of the alloy. Ribbon microstructures, with a perceived reduced cooling rate, can provide insight into the expected solidification path and morphology of particulate processed via HPGA. The microstructural and magnetic results reveal the stability of the desired $RE_2Fe_{14}B$ phase due to the recent additions of Zr and TiC to the alloy.

Table IV: Melt spun composition used in this study.

Alloy Designation	Nominal Composition	Wheel Speed
WT-102	$[Nd_{0.45}(Y_{0.66}Dy_{0.33})_{0.55}]_{2.3\text{-}0.1}Zr_{0.1}(Fe_{0.89}Co_{0.11})_{14}B+Ti_{0.02}C_{0.02}$	13m/s
WT-102	$[Nd_{0.45}(Y_{0.66}Dy_{0.33})_{0.55}]_{2.3\text{-}0.1}Zr_{0.1}(Fe_{0.89}Co_{0.11})_{14}B+Ti_{0.02}C_{0.02}$	16m/s

As seen in Figure 16 and Figure 18, an observable length scale is beyond the limitations of the SEM. Through TEM, Figure 17 revealed that melt-spinning at 16m/s produced finely dispersed nanocrystals on the order of 20nm within an amorphous matrix. Upon annealing in Ar at 700°C for 15 minutes, devitrification of the matrix produced grains of 50nm as seen in Figure 19.

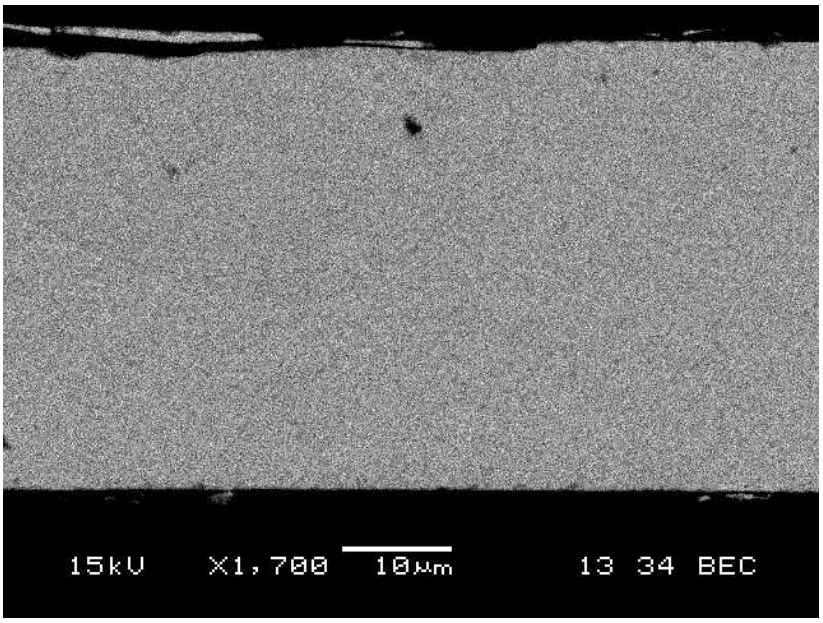

Figure 16: Back-scattered SEM cross-section of etched melt spun ribbon at 16m/s.

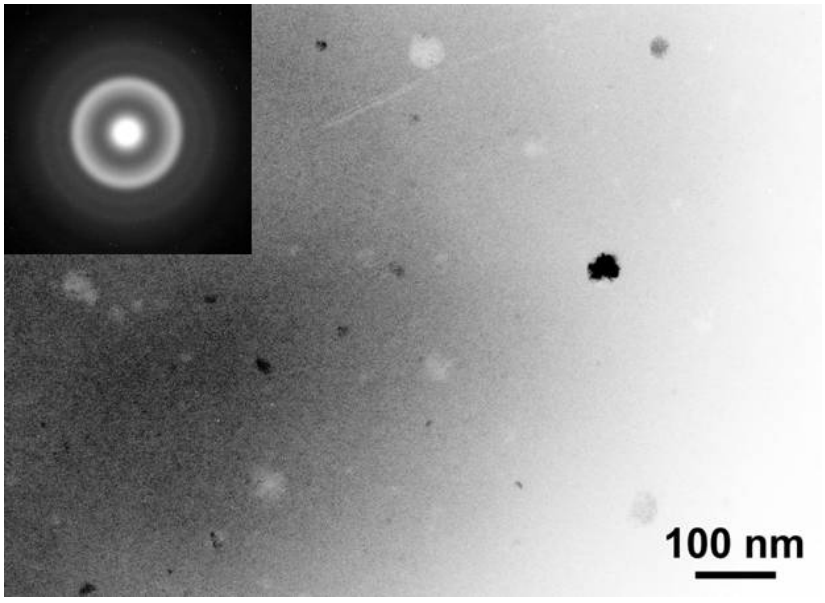

Figure 17: TEM micrograph of as spun condition, revealing nanocrystallites in an amorphous matrix.

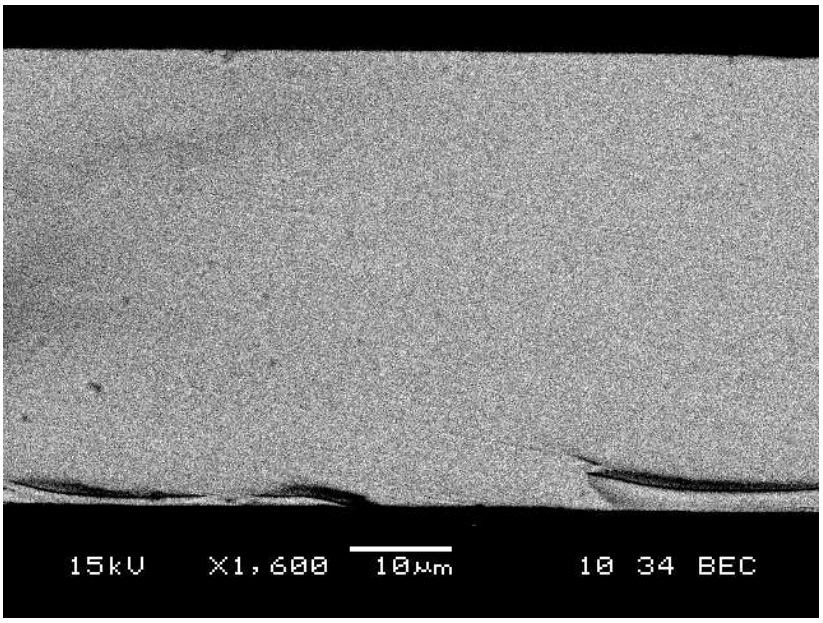

Figure 18: Back-scattered SEM cross-section of etched melt spun ribbon at 16m/s, annealed at 700°C for 15 minutes.

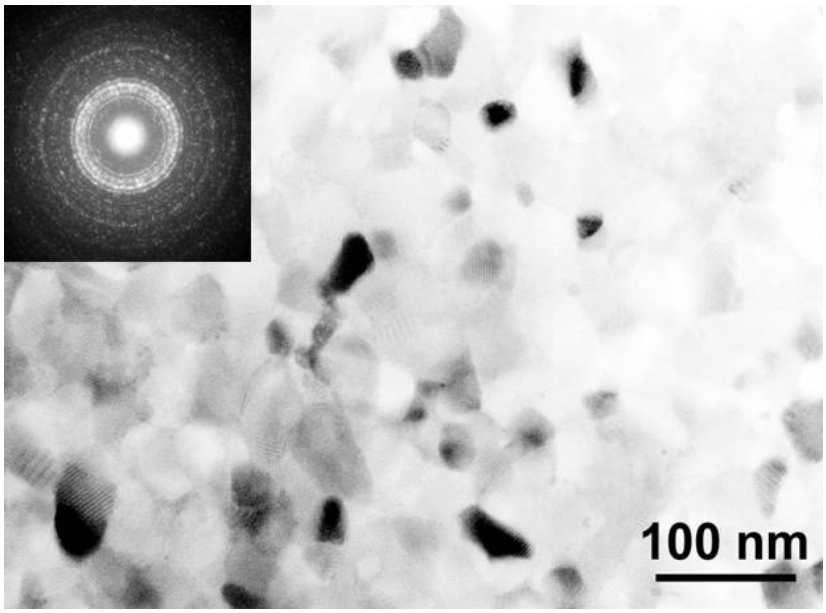

Figure 19: TEM micrograph of annealed ribbon showing a fully crystallized nano-grained structure.

As shown in Figure 20, the as-spun version of the alloy exhibits a reduced $(BH)_{max}$ of 8.5 MGOe as compared to the annealed version of the alloy, 11.9 MGOe (a 40% increase after annealing). The reduced initial $(BH)_{max}$ can be attributed to the presence of the amorphous matrix. Annealing the ribbon improves the hard magnet properties through the nucleation

and growth of 2-14-1 from the glassy phase. It is evident through sufficient additions of Zr and TiC, an average grain size of 50nm can be obtained with an improved $(BH)_{max}$ of 11.9 MGOe in the annealed state.

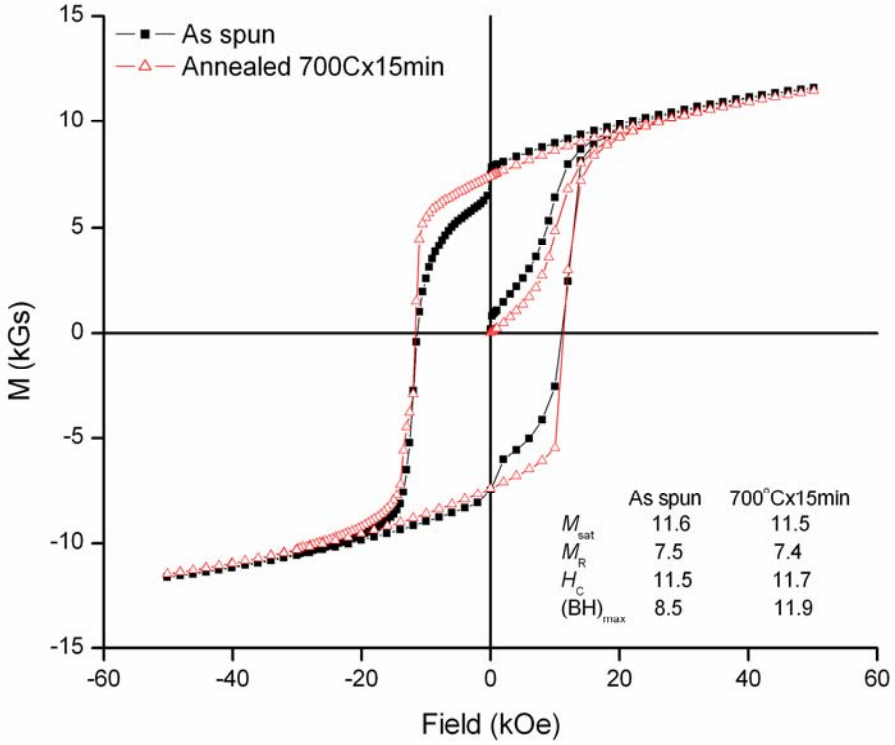

Figure 20: Hysteresis loops of melt spun ribbon at 16m/s.

Melt spinning at 13m/s was subsequently carried out for the same alloy to determine if the Zr and TiC additions were capable of forming 2-14-1 at a lower cooling rate, approaching that of gas atomization. Figure 21 thru Figure 23 show the solidified morphologies of the alloy melt spun at 13m/s. A noticeable interface was revealed that is located approximately 17μm from the wheel side of the ribbon where solidification is known to initiate. This observation reveals the drastic effects on the microstructure from the small difference in cooling rates due to the slightly decreased circumferential wheel speed. As soon as the solidification front slows down, dendritic structures appear to extend from the interface towards the free side of the ribbon. Near the free surface, excessive coarsening occurs resulting in cellular structures on the order of several microns.

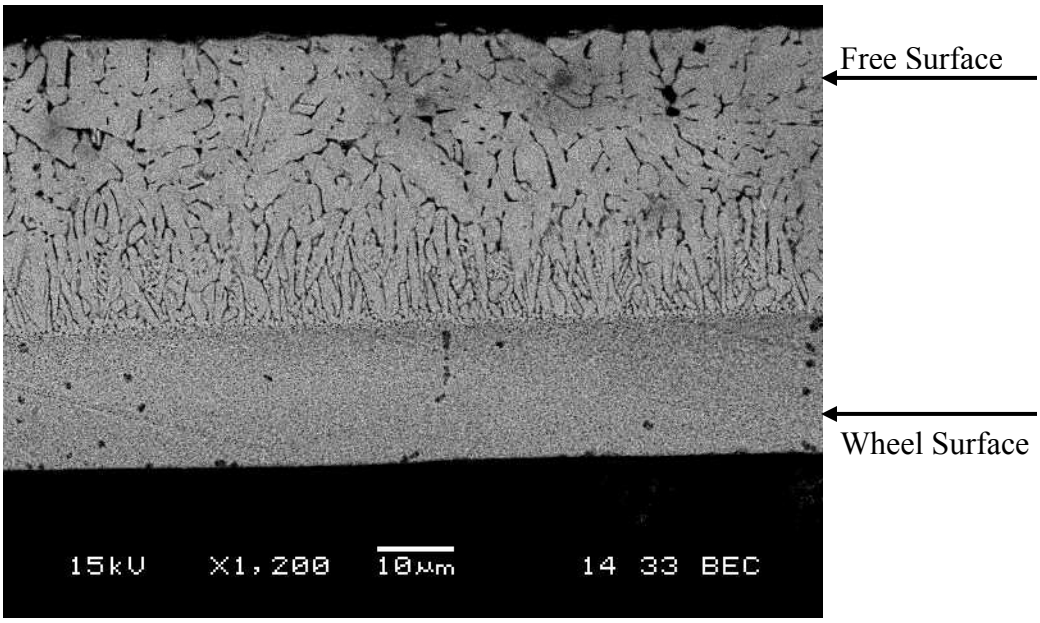

Figure 21: Back-scattered SEM cross-sectional microstructure of melt spun ribbon at 13m/s**.**

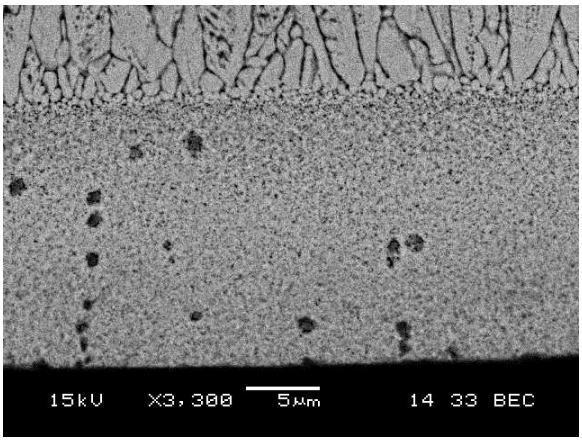

Figure 22: Back-scattered SEM of highly refined microstructure formed at the wheel surface of the ribbon spun at 13m/s.

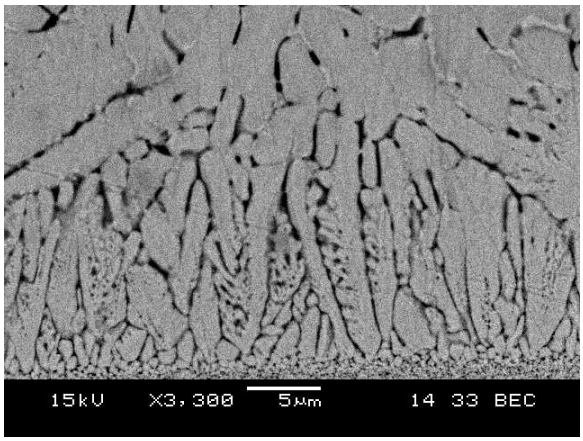

Figure 23: Back-scattered SEM of dendritic and cellular structure nearing the free surface of the ribbon spun at 13m/s.

The x-ray diffraction pattern, Figure 24, was collected on melt spun 13m/s ribbon flake, crushed into powder with a mortar and pestle in ethanol within a nitrogen atmosphere. Crushing of the ribbon was performed in order to provide a bulk structural analysis as it was apparent from SEM investigation the microstructure transitioned from the wheel side to the free side, indicative of possible undesirable phase formation. This bulk perspective can be correlated to the magnetic measurements, which are also a bulk analysis. Preliminary investigation of the pattern reveals that the dominant solidified phase is 2-14-1, although

when compared to stoichiometric $Nd_2Fe_{14}B$ (not shown here), the peaks are shifted due to slight changes in lattice constants attributed to the substitution of smaller Zr atoms in Nd sites and larger Co atoms in Fe sites. The significantly reduced solidification rate near the free side produced a dendritic 2-14-1 phase suggesting that the latest alloy enhancements are capable of suppressing the formation of the 2-17 phase or α-Fe, making it possible to utilize the alloy for HPGA.

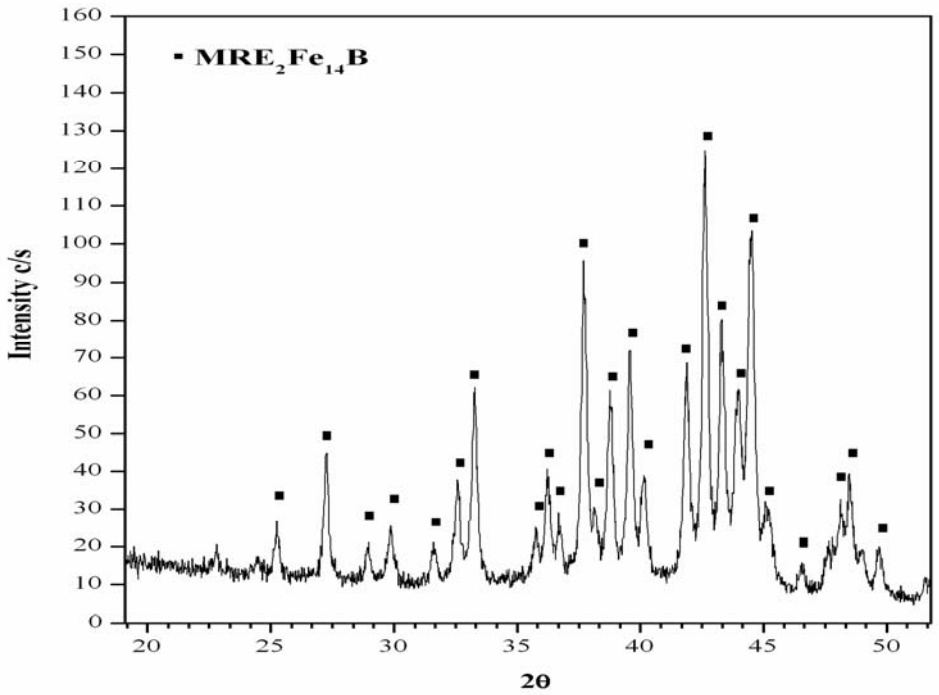

Figure 24: XRD trace showing 2-14-1 structure of crushed ribbon, spun at 13m/s.

The volume fraction of extensive dendritic coarsening region near the free side of 13m/s ribbon reduced the magnetic properties of the volume fraction of the ribbon that experienced an enhanced coupling effect from nanometric, 1-100nm, magnetic domains. This resulted in a $(BH)_{max}$ of 9.6 MGOe in the as spun state, compare to Figure 20, whereupon annealing slightly decreased the coercivity from 12.3 to 11.7 kOe (a 5% decrease), see Figure 25. This can be attributed to possible growth or formation of the 2-17, or α-Fe phase and general grain coarsening near the free side of the ribbon during the annealing stage as evidenced by the curvature in the second quadrant.

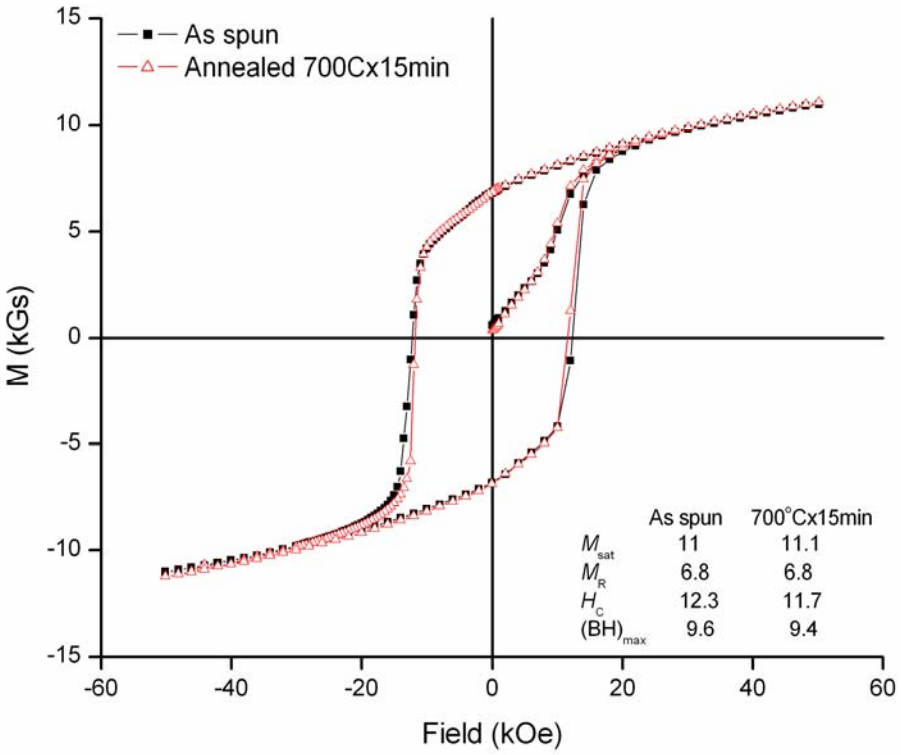

Figure 25: Hysteresis loops of melt spun ribbon at 13m/s.

The difference in energy product between the as spun and annealed states (2%) seems negligible, notably at a reduced solidification rate, proving the stability of the 2-14-1 phase formation during heat treating for this alloy. Not only does the 2-14-1 remain the dominant phase, but these results reveal the effectiveness of grain size reduction and grain boundary pinning through the additions of Zr and TiC to the alloy.

4.2 Translation to Gas Atomization Processing

The ability to produce a high yield of fine spherical powder through an efficient processing route is an advantage of the HPGA system. Initial attempts at He gas atomization of the alloy $[Nd_{0.45}(Y_{0.66}Dy_{0.33})_{0.55}]_{2\text{-}0.1}Zr_{0.1}(Fe_{0.89}Co_{0.11})_{14}B+Ti_{0.02}C_{0.02}$ resulted in unfavorable magnetic properties (GA-1-52) due to compositional deficiencies (discussed below). Through adjustments to the alloying procedure the target composition was achieved successfully (GA-1-66), see Table V for nomenclature and associated compositions of alloys

used in this study, and will be described in more detail in the following sections. However, it should be noted that GA-1-52 and GA-1-66 are the only HPGA alloys which are microstructurally and magnetically reported on. The other runs are primarily utilized for the in situ HPGA fluorination analysis. In addition, Table VI lists the processing conditions of each atomization run to compliment the remainder of the results.

Table V: Nominal HPGA compositions used in this study.

Designation	Alloy Formula
GA-1-52	$[Nd_{0.45}(Y_{0.66},Dy_{0.33})_{0.55}]_{2\text{-}0.1}Zr_{0.1}\ (Fe_{0.89},Co_{0.11})_{14}B+Ti_{0.02}C_{0.02}$
GA-1-66	$[Nd_{0.45}(Y_{0.66},Dy_{0.33})_{0.55}]_{2.3\text{-}0.1}Zr_{0.1}\ (Fe_{0.89},Co_{0.11})_{14}B+Ti_{0.02}C_{0.02}$
GA-1-100	$[Nd_{0.45}(Y_{0.66},Dy_{0.33})_{0.55}]_{2.3\text{-}0.3}Zr_{0.3}\ (Fe_{0.93},Co_{0.07})_{14}B+Zr_{0.01}C_{0.01}$
GA-1-106	$[Nd_{0.45}(Y_{0.66},Dy_{0.33})_{0.55}]_{2.3\text{-}0.3}Zr_{0.3}\ (Fe_{0.93},Co_{0.07})_{14}B+Zr_{0.01}C_{0.01}$

Table VI: HPGA processing conditions

Parameter	Alloy Designation			
	GA-1-52	GA-1-66	GA-1-100	GA-1-106
Alloy $T_{melting}$	1200°C	1200°C	1200°C	1200°C
Pour Temperature	1550°C	1550°C	1625°C	1625°C
Atomization Gas	He	He	He	Ar
Gas Pressure	5.52MPa	5.52MPa	5.52MPa	6.89MPa
Gas to Metal Ratio	0.66	1.0	0.5	0.5
NF_3 injection	no	yes	Yes	yes

The dominant solidified microstructures of GA-1-52 particles are shown in Figure 26. Formation of highly dendritic and cellular growth in a broad range of atomized particle sizes of similar compositions was previously shown to be mostly the 2-17 phase [49][24], conclusively. The GA-1-52 atomized particles are primarily composed of the 2-17 soft magnetic phase based upon the significant amount of dendritic and cellular features. This is supported through hysteresis loop measurements, as seen in Figure 27, which confirms the customary high M_r (6.9 kGs) and very low H_C (2.8 kOe), even upon annealing, exhibited by a soft magnet.

a)

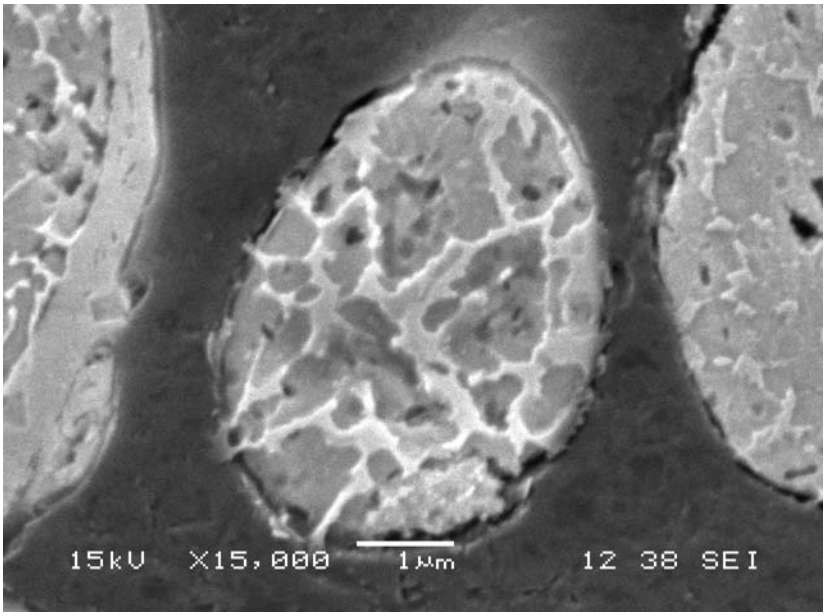

b)

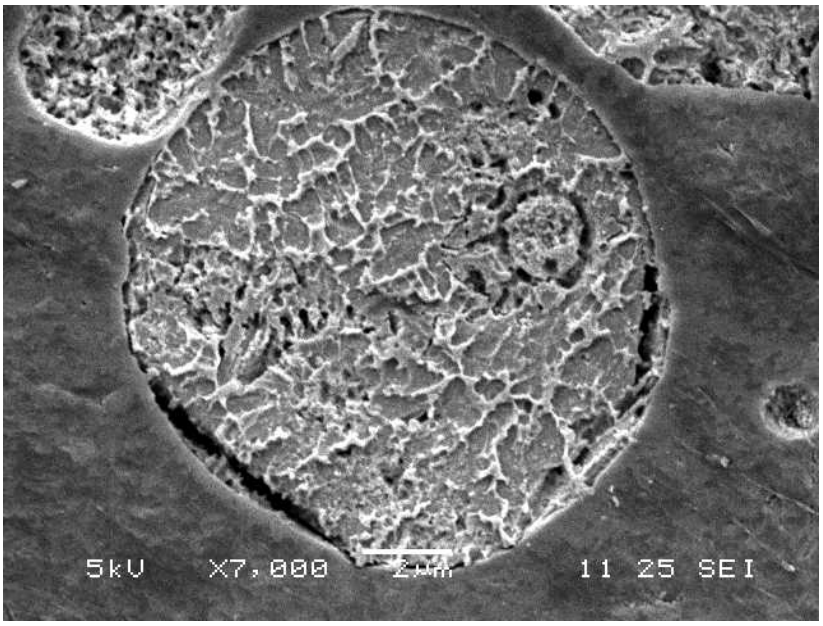

Figure 26: GA-1-52 particle microstructures a), b) deficient in B and Zr resulting in a dendritic and cellular structure, even in the smallest of particle size fractions (top micrograph).

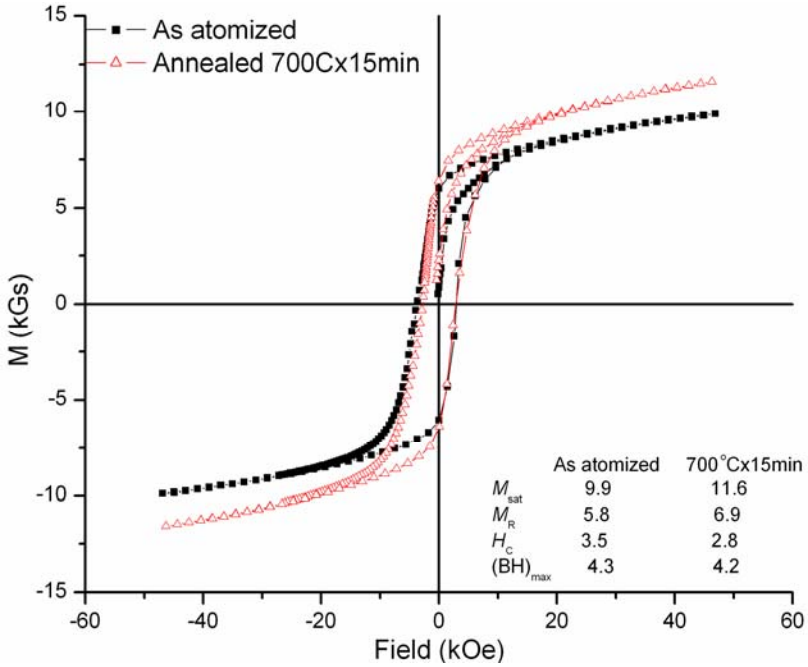

Figure 27: Hysteresis loops for GA-1-52, +10-15µm particle distribution.

It was determined through chemical analysis, provided by NSL Analytical Services, Inc., that the target composition was off in GA-1-52 due to unforeseen reactions of constituents with the crucible during induction melting of the pre-alloyed charge, refer to Table VII. Nominal values refer to calculated pre-alloyed constituent weight percents and contain some error due to difficulties in producing the charge. The values below GA-1-52 and GA-1-66, respectively, are the as-atomized measured values as reported by NSL. It is believed the loss of B and Zr during GA-1-52 resulted in the formation of the iron rich phase, 2-17, during solidification. In order to accommodate the unanticipated losses during atomization, B and Zr were enriched in the melt for GA-1-66.

Table VII: NSL chemical analysis results for GA-1-52 and GA-1-66

Constituent	Target wt%	Nominal	GA-1-52	Nominal	GA-1-66
Y	6.5	6.7	5.8	6.6	6.0
Dy	5.9	6.1	6.4	6.0	6.1
Nd	12.9	13.3	13.7	13.7	13.7
Fe	63.0	62.2	62.2	62.0	61.7
Co	8.0	7.9	8.0	8.0	8.1
B	1.0	1.0	0.8	1.1	1.0
Zr	0.8	0.8	0.5	1.1	1.1
Ti	1.6	1.6	1.6	1.6	1.6
C	0.4	0.4	0.4	0.4	0.4

With the use of He gas in the HPGA system, an average particle size of 12.4μm with a standard deviation of 2.8 was achieved with GA-1-66, as a typical result of size distribution analysis with a (Microtrac) laser scattering size analyzer, Figure 28. Particle sizes in this range have a very high surface area which corresponds to an increased surface energy and an increased tendency to oxidize spontaneously upon exposure to air. Figure 29 shows the near-spherical solidified shape that is produced through gas atomization in addition to multiple oblong and irregular shaped particles, where the reduced pour temperature may have resulted in insufficient droplet spherodization due to a rise in melt viscosity. Oxidation during processing could easily consume useful magnetic material and degrade the properties at an accelerated rate. Fluoride passivation of the particle surfaces was performed on GA-1-66, GA-1-100, and GA-1-106 in order to reduce the rate of oxidation during further handling.

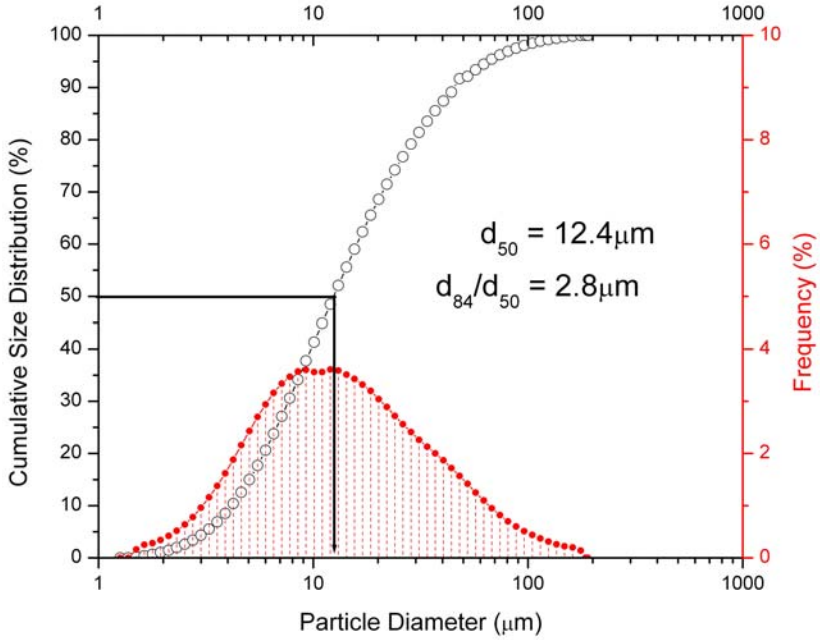

Figure 28: GA-1-66 particle distribution determined with a Microtrac laser scattering size analyzer.

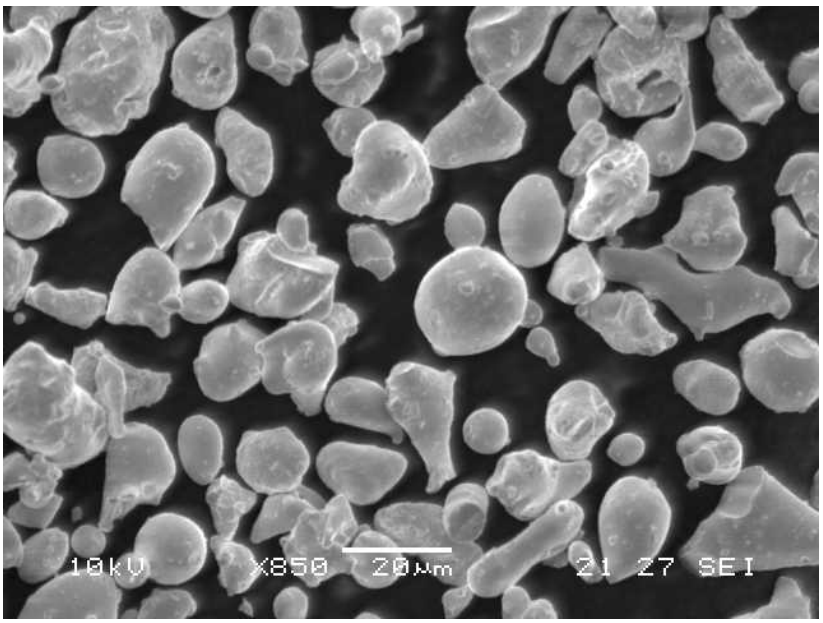

Figure 29: SEM micrograph of in situ passivated HPGA spherical powder, GA-1-66.

With the correct composition, the effectiveness of the alloy enhancements designed for use in HPGA can be seen in Figure 30 and Figure 32. As-atomized particles below 5μm are predominantly amorphous and contain finely dispersed (etched out) nanocrystallites as

observed with the SEM. These microstructural results are notably different and more desirable than those observed from GA-1-52, suggesting the loss of B and Zr were primarily responsible for the formation of the soft magnetic phases.

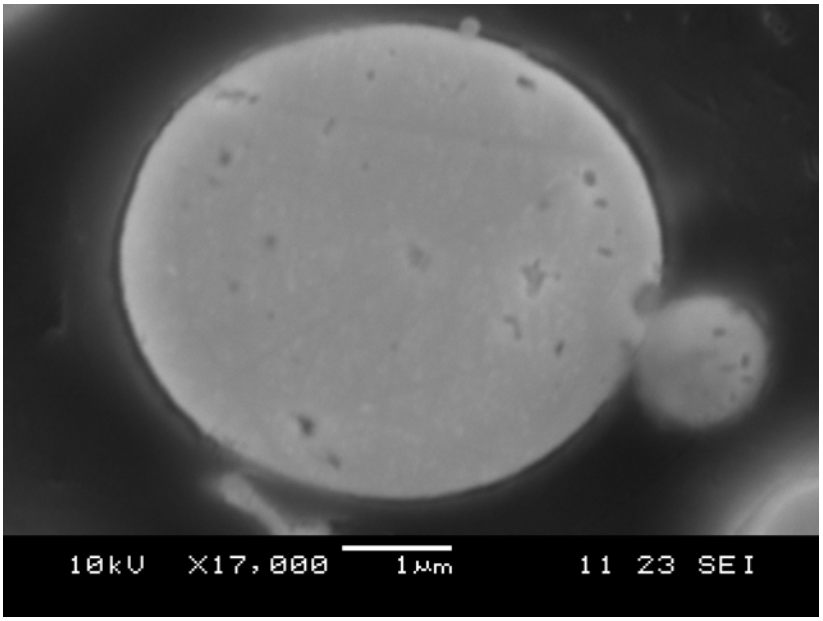

Figure 30: SEM micrograph of as-atomized GA-1-66, polished and etched, <5µm particle exhibiting an amorphous matrix with dispersed, etched out nanocrystallites.

A report of magnetic properties for as-atomized and annealed <5µm particle distribution can be seen in Figure 31. The as-atomized state displays a magnetic response consistent with amorphous particles, no detectable coercivity, yet exhibits a large saturation of 10.6 kGs. Upon annealing, crystallization of nanosized, ~50nm, grains promotes anisotropy of nucleated magnetic domains. The random alignments of magnetic domains are subsequently pinned by the grain boundaries giving a characteristic permanent magnet response with an increased H_C (9.3 kOe) and moderate M_r (6.9 kGs). However, the lack of squareness of the loop, as indicated by the arrow in Figure 31, suggests that the annealing treatment may not have been sufficient to fully crystallize the matrix.

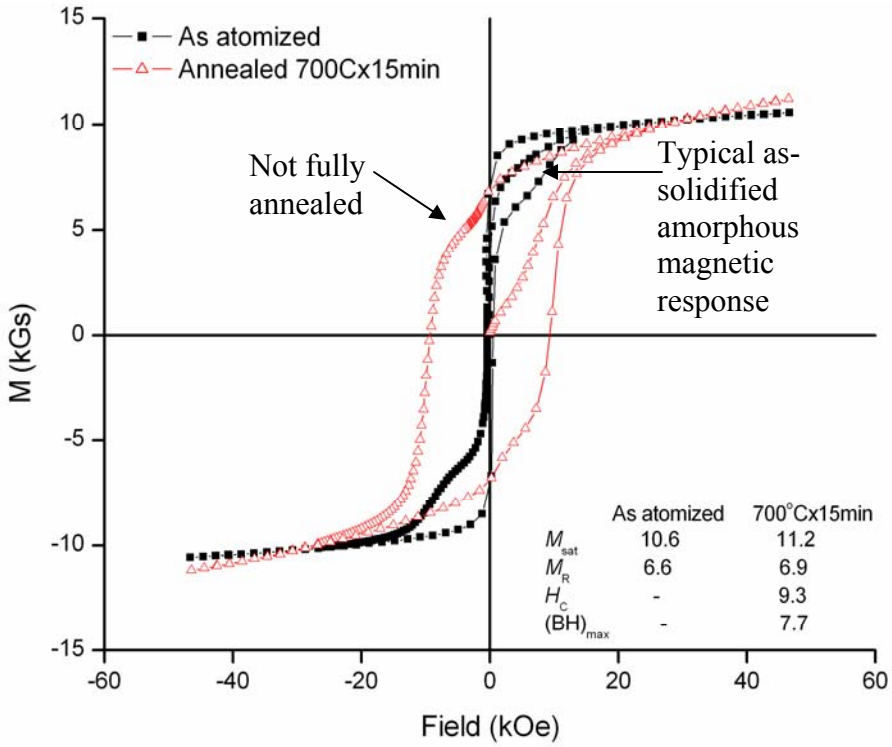

Figure 31: Hysteresis loops for GA-1-66 <5µm particle distribution revealing hard magnetic properties upon devitrification.

Further examination of as-atomized particles between +5-10µm with TEM revealed the amorphous matrix with finely dispersed nanocrystallites on the order of a few nanometers. Annealing at 700°C for 15 minutes devitrified the majority of the matrix allowing for interior grain growth of ~50nm. The surface "rim" of the particles exhibits a more refined microstructure, appearing to be on the order of ~20nm, which can be attributed to the cooling characteristics of HPGA processing [74].

a)

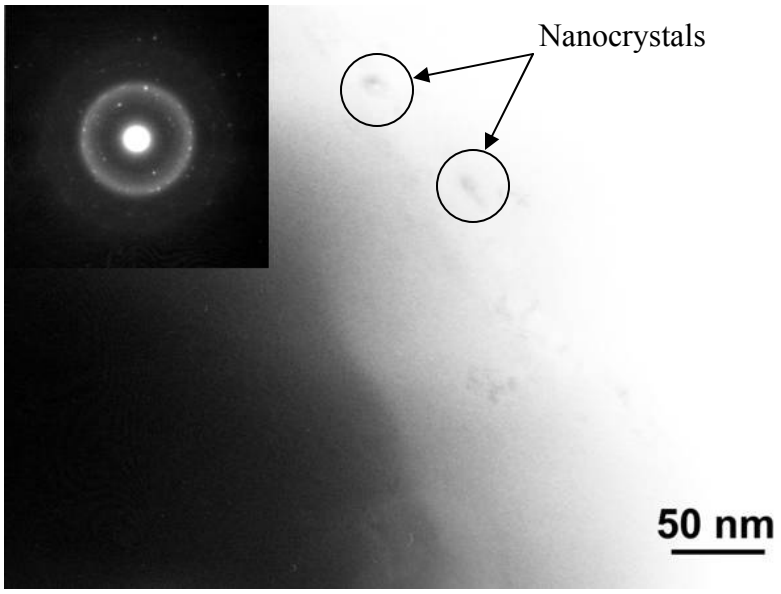

b)

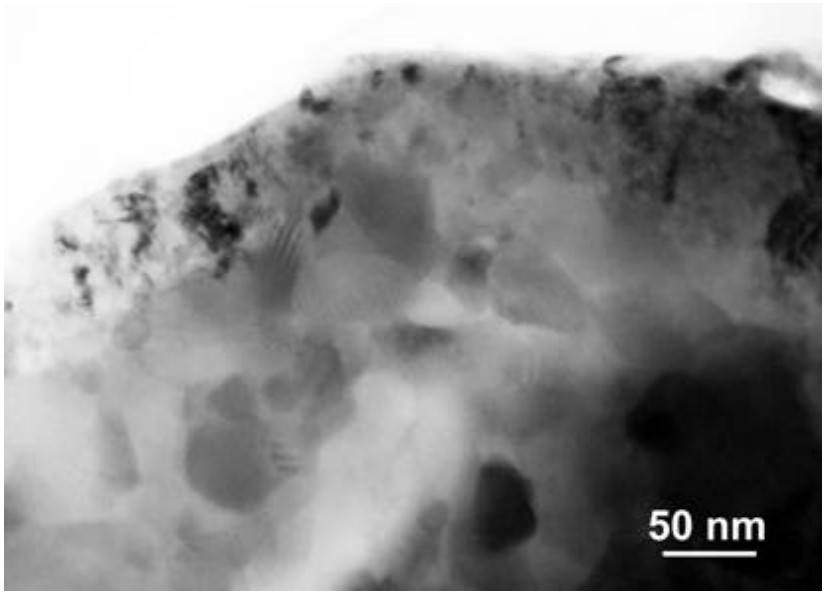

Figure 32: TEM micrographs of a GA-1-66 +5-10μm particle; (a) as-atomized exhibiting highly amorphous matrix with a few dispersed nanocrystals, (b) annealed particle revealing a fine grained structure upon devitrification.

A similar microstructure with increased evidence of fine crystallized phases can be noticed through incrementally larger particle size distributions as seen in Figure 33. Zr and TiC additions made it possible for larger particles to experience high enough cooling rates to form an amorphous matrix with the formation of finely dispersed nanocrystals, see Figure 34 for an enhanced representation. This allows considerable microstructural control over a high

yield of He atomized powder, referring back to Figure 28. Since the average particle size, 12.4μm, of GA-1-66 is within the desirable microstructural particle size range, an increased yield of the atomized powder can be utilized for bonded magnet production.

a)

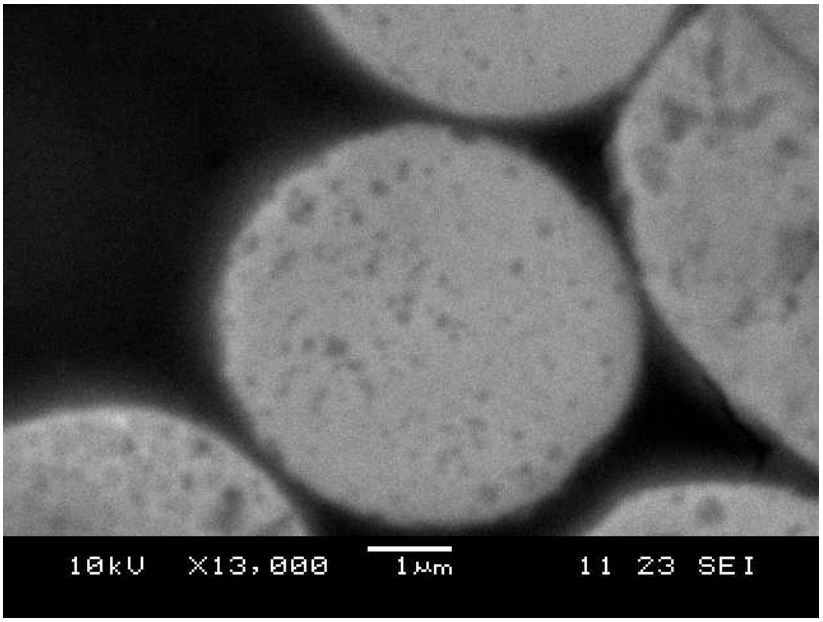

b)

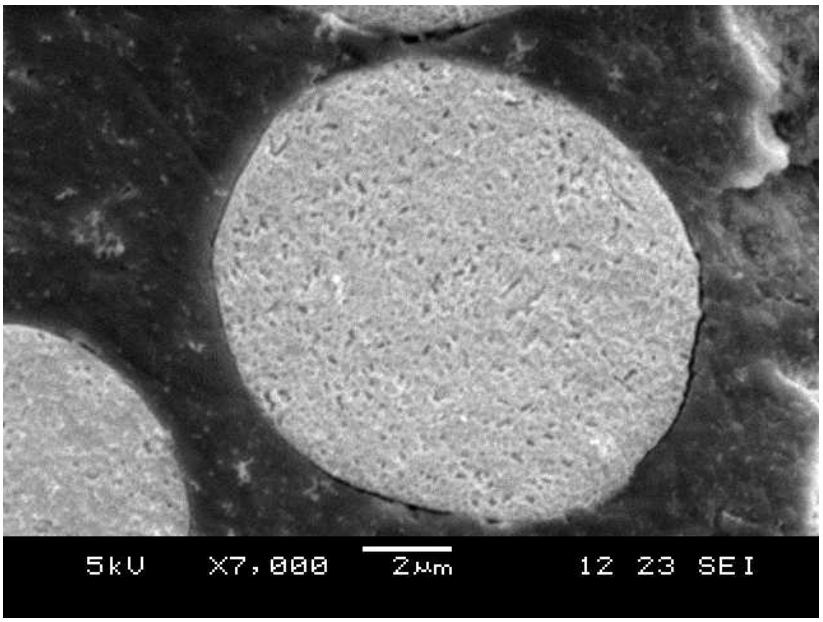

Figure 33: SEM micrographs of polished and etched as-atomized GA-1-66; (a) +5-10μm particle range and (b) +15-20μm particle range.

To confirm morphology patterns seen with the SEM in larger particles and the extrinsic effect that microstructure has on the magnetic properties per the hysteresis loops, TEM was performed on the +20-25µm distribution in addition to the +5-10µm particles. As shown in Figure 34, the as-atomized state retains an amorphous matrix with a significant amount of embedded nanocrystallites which coarsen during devitrification of the matrix.

a)

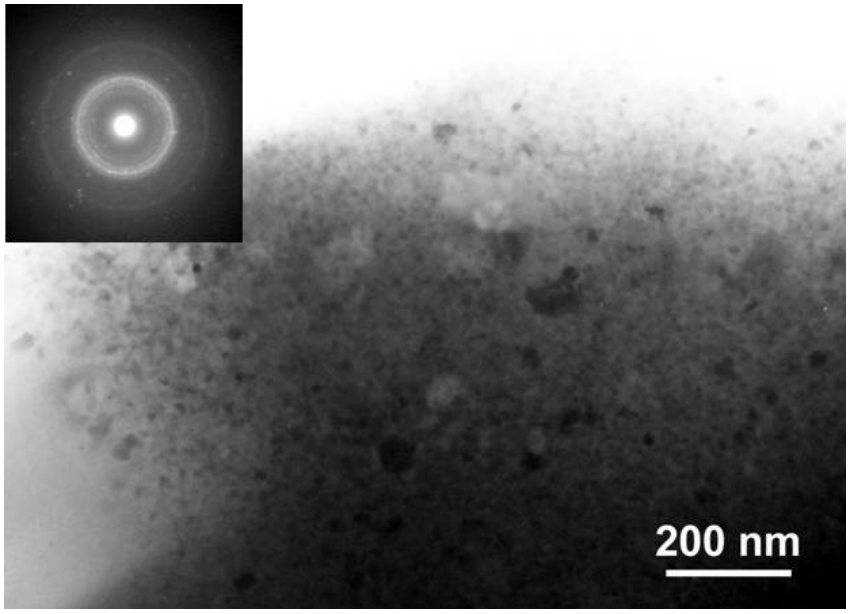

b)

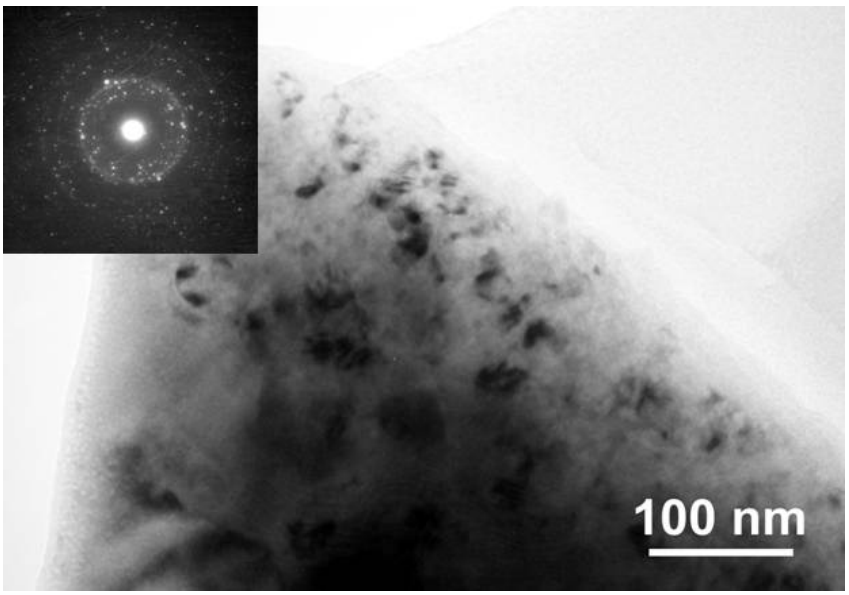

Figure 34: TEM micrographs of a GA-1-66 +20-25µm particle; (a) as-atomized, (b) annealed at 700°C for 15 min.

Hysteresis loops for the as-atomized and annealed states verify the direct formation of the 2-14-1 phase in Figure 35, even in particle distributions of 20-25µm. As evidenced by a partial crystalline response in the as-atomized state, coercivity is present, however, noticeably increases as the remaining amorphous fraction converts to crystalline 2-14-1 and coarsens during annealing. This annealing step at 700°C for 15 minutes crystallized fine grains of 2-14-1 from the amorphous matrix, increasing $(BH)_{max}$ from 5.2 to 9.2 MGOe.

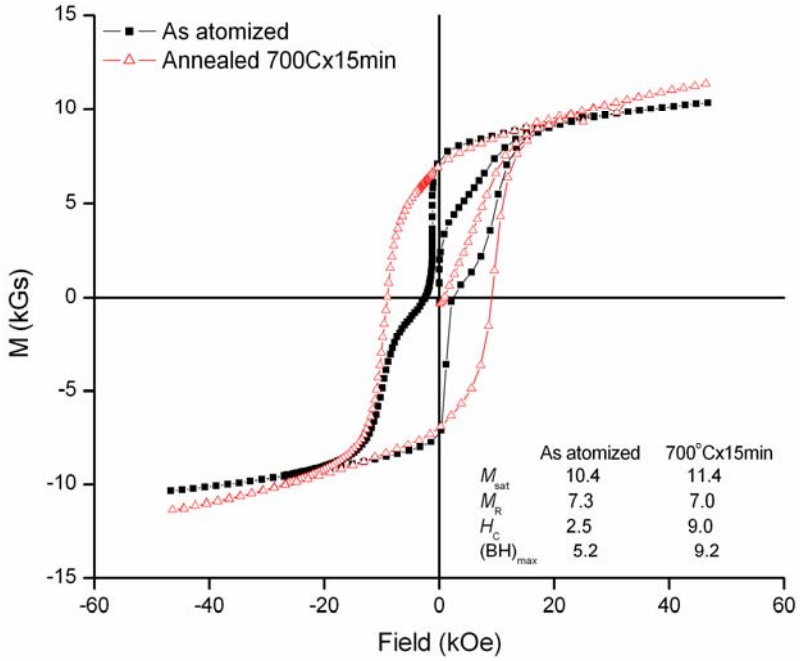

Figure 35: Hysteresis loops for GA-1-66 +20-25µm particle distribution revealing hard magnetic properties upon devitrification.

Further analysis with x-ray diffraction on the +20-25µm particle distribution revealed evidence of an amorphous matrix in the as-atomized state with 2-14-1 as the primary phase, Figure 36. The amorphous matrix is indicated by the slight hump between $30^{2\theta}$-$50^{2\theta}$ in addition to peak broadening and low intensity peaks. After annealing, the particles were mostly crystallized and initial indexing revealed characteristic hard magnetic 2-14-1 phase peaks. An increase in the 2-14-1 peak intensities suggests that these particles are primarily 2-14-1, however there are possible indications of the presence of 2-17 or α-Fe phases in small amounts, more indexing and a better understanding of the alloying behavior is necessary to fully recognize all impurity phases present. As mentioned previously, the $MRE_2Fe_{14}B$ peaks

are shifted to slightly different 2θ in comparison to stoichiometric $Nd_2Fe_{14}B$ diffraction peaks due to substitutions of Dy, Y, Zr, and Co into the crystal structure, thereby changing the lattice constants.

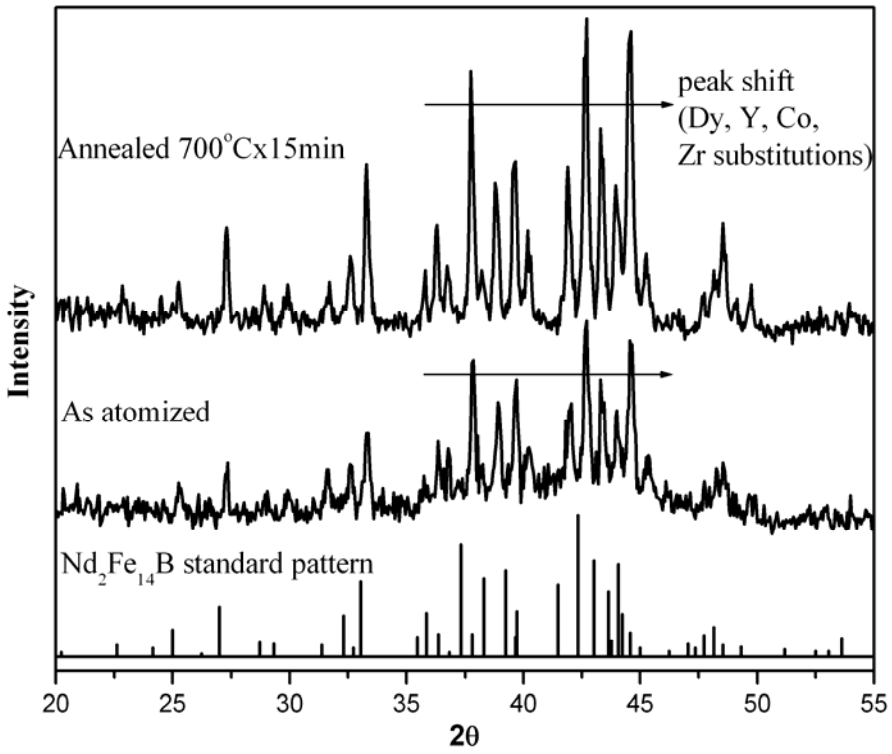

Figure 36: XRD patterns of GA-1-66 +20-25μm particle distribution exhibit a characteristic $MRE_2Fe_{14}B$ structure.

It has been shown that perhaps larger particles, +20μm, are now capable of exhibiting the desired microstructural length scales with sufficient hard magnetic properties due to the recent alloy additions as a summary of magnetic properties in Table VIII indicates.

Table VIII: Summary of magnetic properties on a collection of <25μm GA-1-66 particles.

	SI (cgs)	As-Atomized	700°Cx15min
M_S	mT (kGs)	1040 (10.4)	1140 (11.4)
M_r	mT (kGs)	730 (7.3)	700 (7)
H_c	kA/m (kOe)	200 (2.5)	716 (9)
$(BH)_{max}$	kJ/m^3(MGOe)	41.4 (5.2)	73.2 (9.2)

4.3 Fluorination of Magnet Particulate

4.3.1 Residual Gas Analysis

In all fluorination experiments performed, both in the fluidized bed and in situ atomization, residual gas analysis was utilized to monitor local atmosphere and gaseous evolution as the experiment progressed. The following RGA results depict the nature of the experiment and progression in understanding the reactions that are occurring during fluorination of magnet particulate as inferred from the analysis.

4.3.1.1 Magnetically Stirred – Fluidized Bed Apparatus

Residual gas analysis data obtained during the fluidized bed approach to controlled fluorination revealed information on the partial pressures of gases present within the reaction chamber, as previously discussed. Generally, the 10%NF_3/90%Ar tank was opened and allowed to flow through the fluidized bed once the temperature of the particles inside the reaction chamber, as measured with a type-K thermocouple, reached a desired set fluorination temperature. NF_3 gas was passed through the chamber for approximately 60 minutes or until the reaction was determined to have come to completion, indicated by a decrease and plateau behavior in N_2 and O_2 partial pressures. All of these results were obtained with the same NF_3 concentration, 0.05%, at least an order of magnitude lower than previous fluorination experiments performed by Buelow [39].

As a typical experimental gas trend result, Figure 37, nitrogen, oxygen, and nitrogen trifluoride were monitored during fluorination of melt spun particulate MQP-11-HTP at constant temperature of 185°C. Baseline gas partial pressures within the chamber were established prior to the beginning of the run as shown by the level of N_2 within the detected atmosphere as well as no detectable NF_3 or O_2 at t = 0sec. This was expected as the reaction chamber was evacuated twice before being backfilled with gettered UHP Ar. It should be

mentioned that Ar was also monitored, but is not illustrated due to its inactivity during the experiment. The distinctive rise in N_2 and O_2 indicates the release of NF_3 into the chamber and, more importantly, the reaction between the particle surfaces with the gas. The initial rise of NF_3 at the beginning suggests that not all the gas was consumed by the surface reactions and therefore rises to an equilibrium pressure. A secondary rise is apparent in the NF_3 trend as the surfaces of the particles become passivated and additional NF_3 exits through the exhaust. This behavior correlates well with the rise, peak, and decrease of both N_2 and O_2 partial pressures. Particle surface passivation begins to occur after approximately 15 minutes, indicated with the dashed line, at which point the N_2 and O_2 have reached their respective maximum partial pressure levels. As the surfaces continue to be coated and passivated, the partial pressures of N_2 and O_2 decrease as NF_3 increases and eventually return to their respective baseline concentrations after approximately one hour. These characteristic results were reproducible and expected to change with an increase or decrease in supplied activation temperature of the particles, thereby dictating the extent of the reaction.

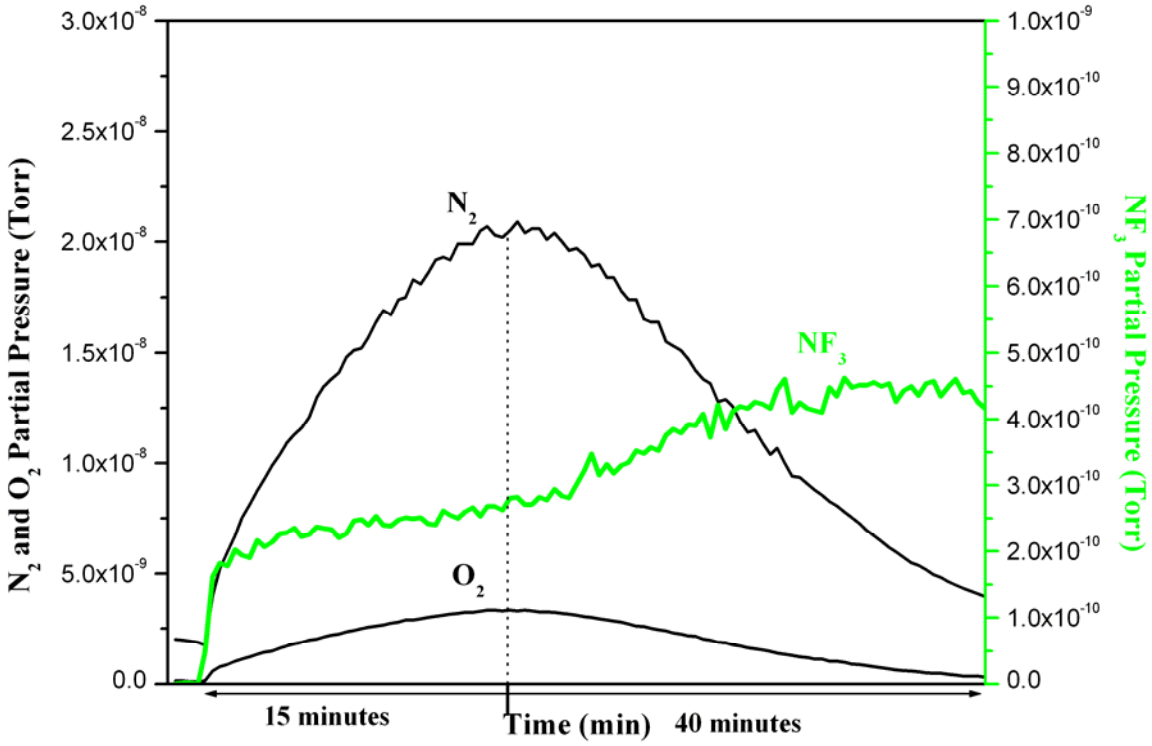

Figure 37: RGA analysis on fluorinated MQP-11-HTP at 185°C.

Therefore, successive fluorination experiments were carried out at different temperatures under the same starting atmosphere and particle surface conditions to create a range of particle coating thicknesses and uniformity. Figure 38 illustrates the normalized difference in N_2 formation from consecutive fluorination treatments at 5°C increments. Initial experiments were performed at 160-165°C, the previous suggested fluorination temperatures [39]. There was no indication of surface fluorination at these temperatures, as detected by the RGA, and the trends are consequently not within the figure. The first temperature to demonstrate an activation of surface fluorination was at 170°C and can be considered the lower limit to initiate a reaction under the given experimental conditions. As shown, an increase in temperature resulted in an increase of maximum N_2 partial pressure prior to complete passivation. In addition, the initial slopes of each curve increase with an increase in fluorination temperature revealing a change in surface kinetics.

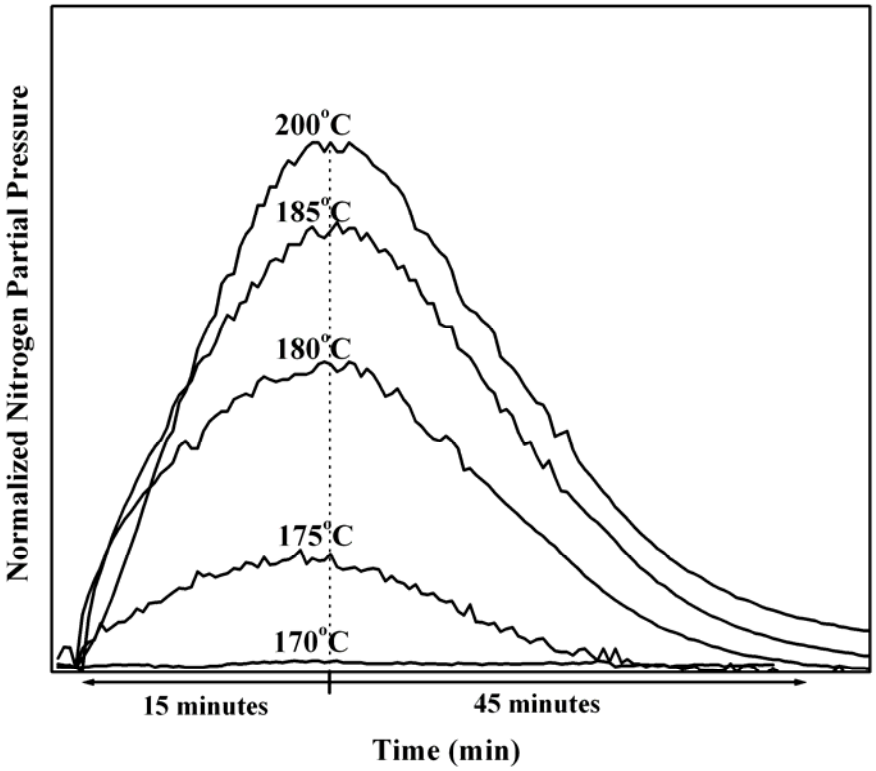

Figure 38: Normalized partial pressure levels of evolved N_2 gas as a result of different fluorination temperatures within the fluidized bed.

The highest reported fluorination temperature in Figure 38 is only 200°C, short of the optimized temperature as suggested by Anderson at 210°C [65]. Although the experimental setup has changed significantly since its first inception, it is believed that those elevated temperatures will still demonstrate a coating thickness beyond what is required for optimized passivation. This will be further elaborated on in the following surface analysis results.

4.3.1.2 In situ HPGA Fluorination

Residual gas analysis data obtained during He or Ar gas atomization and in situ fluorination reveals information on the partial pressures of gases present within the chamber. As seen in Figure 39, argon, nitrogen, and helium were monitored during atomization of the alloy GA-1-66. NF_3, as the reactive gas injected through the halo, was also monitored; however, a measurable concentration was barely detectable during the experiment and is therefore not present within the figure. Baseline gas concentrations within the chamber are established prior to the beginning of the run as shown by the level of Ar within the detected atmosphere as well as no detectable He or N_2 at t = 0sec. This is expected as the chamber is evacuated two times before being backfilled with UHP Ar.

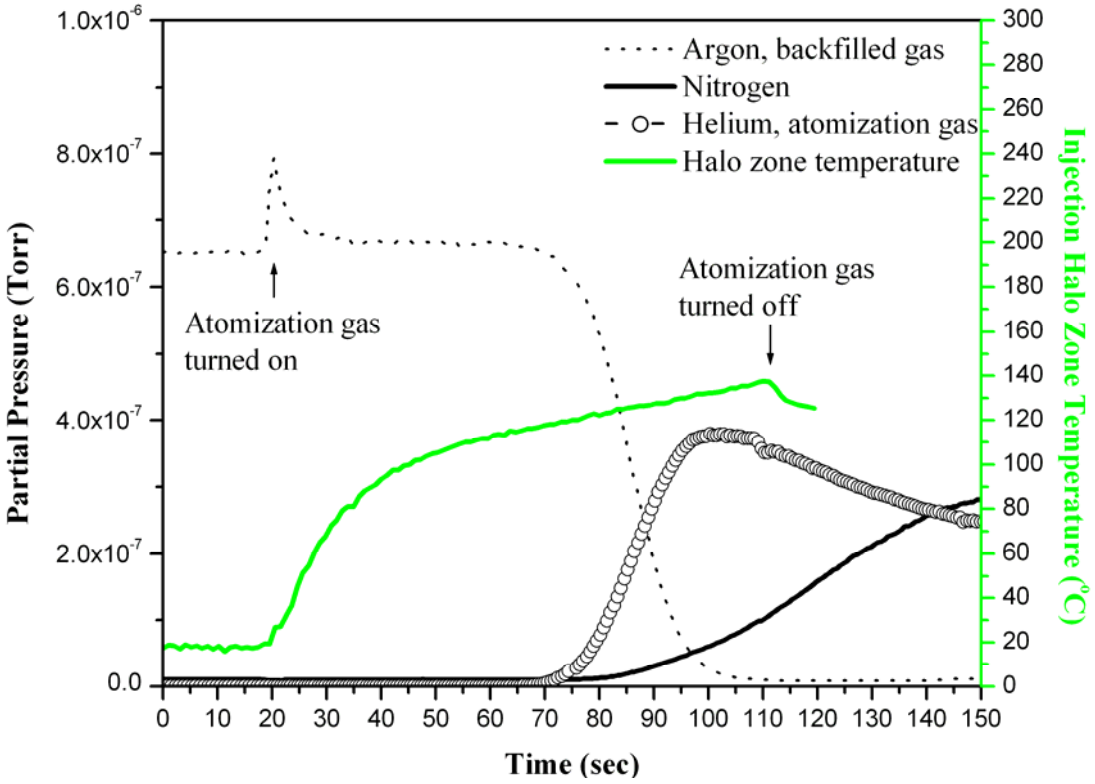

Figure 39: In situ HPGA residual gas analysis as measured with the quadrupole mass spectrometry unit for GA-1-66 along with the temperature profile as measured below the NF_3 injection zone.

The spike in the Ar trend signals the start of the run as the overall pressure of the system initially increases and He gas is injected through the close-coupled high pressure nozzle. The spike diminishes as pressure release valves are initiated and the whole system comes to an equilibrium pressure. He quickly dilutes the chamber and its signal increases quickly as Ar is pushed out of the system and its level of concentration decreases sharply. N_2 evolution is detected as the reactive gas, NF_3, comes in contact with the hot particles as they pass through the halo zone, where the reaction between the hot metal and NF_3 is the only possible source of N_2. Once the atomization run ends and He gas is turned off, the partial pressures of the gases plateau as the atmosphere becomes stagnant and the surface passivation mechanism has gone to completion. N_2 is shown to be at a greater concentration over He after the run has ended, however this is attributed to the ionization efficiency of N_2 in regards to He, with N_2 being more efficient. This method of monitoring gas species within the chamber allows for greater understanding of the localized reactions occurring and increased processing control

for further experiments performed in a similar fashion. In addition, the temperature of the gas flowing past the halo is separately, yet simultaneously measured, as plotted in the figure. The temperature rises quickly as hot metal sprays into the chamber (as droplets) and much of the heat is transferred to the atomization gas. The heat continues to rise until melt flow into the chamber diminishes or stops all together. The temperature of the gas flowing by the NF_3 injection zone supplies the necessary activation energy to enable the dissociation of NF_3 and promote surface reaction with the hot particles.

Observation of gaseous evolution within the atomization chamber was more focused for the subsequent fluorination runs, GA-1-100 (Figure 40) and GA-1-106 (Figure 41). The use of a new RGA coupled together with more accurate temperature acquisition system allowed for increased understanding of the internal environment. As seen in Figure 40, only nitrogen and oxygen are reported in order to observe expected reactions. NF_3 is also monitored, however a detectable level is too low and is not added to the graphs. As before, the baseline partial pressures are recorded prior to the start of the atomization run. The temperature quickly rises once the atomization run is started and begins to plateau around 275-280°C before the melt flow reduces causing a decrease in the chamber atmosphere temperature. During the rise in temperature, the onset of N_2 concentration is evident and can be correlated back to a required temperature range (as illustrated with dashed lines) to initiate a fluorination reaction resulting in the production of N_2 gas and the reduction of possible surface oxides, giving off O_2.

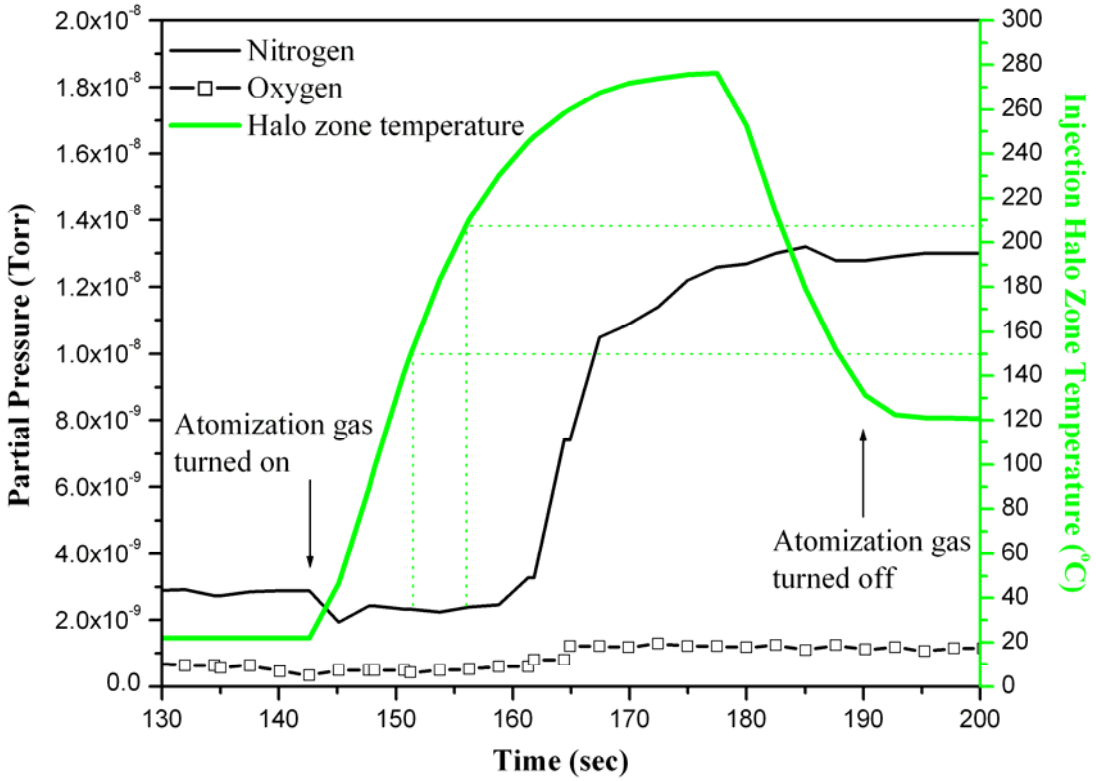

Figure 40: In situ residual gas analysis as measured with the quadrupole mass spectrometry unit for GA-1-100 along with the temperature profile as measured near the NF_3 injection zone.

Using the same RGA settings as GA-1-100, the gas and temperature trends for GA-1-106 (Figure 41) are noticeably different, yet have several similarities. The measured temperature rises to approximately 265-270°C as expected and drops as soon as the hot melt flow decreases prior to the end of the atomization run. However, the onset of N_2 is not seen until the run is almost complete, attributed to the delay in detection and efficiency in conductance of the gas through the capillary tube into the RGA. The measured partial pressure is nearly an order of magnitude lower than the previous run. In addition, the level of nitrogen drops abruptly after the run is over. It is noted that perhaps blockage of the capillary tube may be a reason for this result as the N_2 level rose again several minutes later (not shown in the figure). Also, no noticeable level of oxygen was measured during the run. This result is consistent with the oxygen concentration in the atomized particulates, to be reported in a following section.

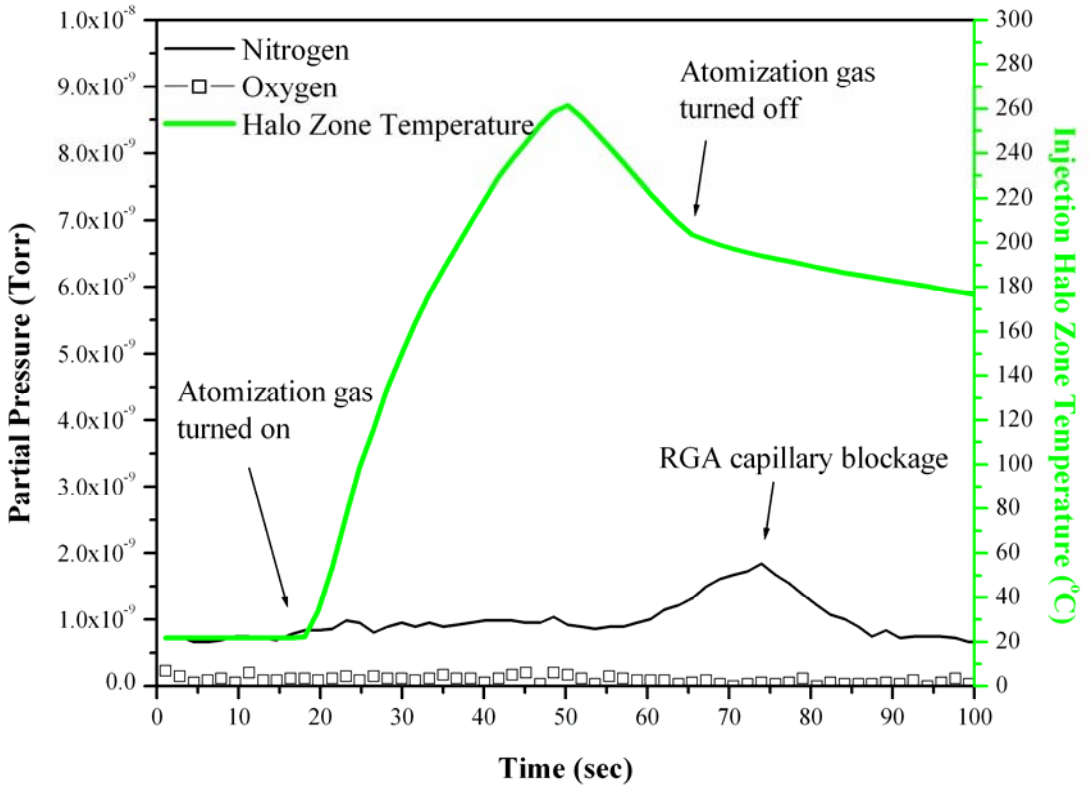

Figure 41: In situ residual gas analysis as measured with the quadrupole mass spectrometry unit for GA-1-106 along with the temperature profile as measured near the NF_3 injection zone.

4.3.2 Surface Analysis

In order to determine the effectiveness of the fluoride coatings as initially presented in the RGA results, only promising fluorinated flake samples were chosen for in-depth surface analysis by several methods. Otherwise, a collection of particles (<45μm) from each HPGA magnet run were analyzed accordingly. These methods include x-ray photoelectron and auger electron spectroscopy for surface structure and apparent fluoride thickness determination respectively, gas fusion analysis for oxygen content, and thermal gravimetric analysis for fluoride stability at increased temperatures. Due to the amount of time it takes to perform XPS and AES, not all of the samples were analyzed thoroughly with both methods. Therefore, only the most informative data is presented in the following sections and may not

include both XPS and AES for each type of sample. Regardless, these results reveal the surface fluoride architecture after in situ HPGA fluorination as well as an effective thickness as produced in the controlled modified fluidized bed. In addition, the improvement in in situ HPGA fluorination is addressed through direct surface chemistry comparison of powder in the unexposed condition.

4.3.2.1 Magnetically Stirred – Fluidized Bed Apparatus

Three fluorinated flake samples of industry supplied MQP-11-HTP which displayed the most promising RGA results were analyzed in the AES. An as-received sample (base alloy) was also examined as a point of reference for characterization of changes to the surface chemistry as a result of fluorination processing. Figure 42 is an averaged AES depth profile produced from a collection of compiled and averaged scans at several surface locations and from multiple flakes. The most prominent surface atoms, oxygen, fluorine, and yttrium are displayed with their relative concentrations plotted as a function of etching time. This etch time can be correlated to the aforementioned standard etch rate of 10nm/min. Therefore an etch time of 10 seconds is approximately equivalent to a depth of 12-15Å.

The base alloy primarily consists of a rare earth-oxide or yttrium-oxide layer as evidenced by the level of oxygen and yttrium on the surface. In comparison to samples fluorinated at 175, 180, and 185°C, the oxygen level is significantly reduced but not completely removed from the surface. On the other hand, fluorine is apparent on all fluorinated samples with the 185°C sample exhibiting a slightly higher initial concentration. It seemingly drops off in concentration more quickly than the lower temperature samples although maintains nearly the same level of fluoride thickness at about 12-20Å. Additionally, the level of yttrium on the fluorinated samples is decreased at the surface in comparison to the base alloy. This behavior is not fully understood, but is most likely a result of the formation of rare earth oxyfluorides (REOF) or rare earth fluorides (REF_3) realizing that the relative RE concentration difference between RE_2O_3 and REF_3 for instance has decreased by half.

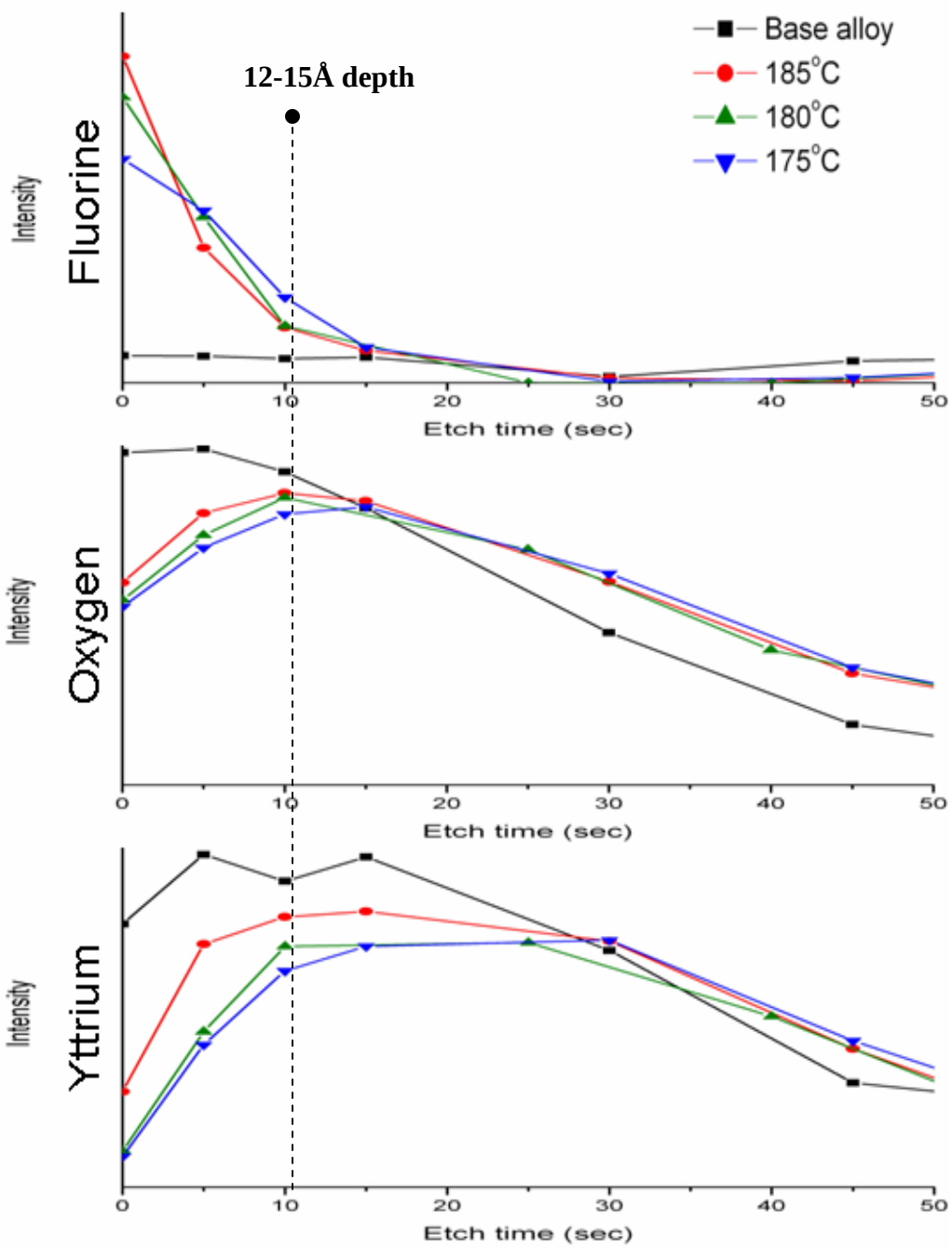

Figure 42: AES depth profile on an as-received (base alloy) flake sample of MQP-11-HTP and on fluorinated flake of the same alloy at temperatures of 175, 180, and 185°C. An etch time of 10 seconds is approximately 12-15Å.

To support the AES measurements, gas fusion analysis was performed on the same fluorinated and base alloy samples, providing insight into the level of oxygen and nitrogen

before and after the specified fluorination reaction. Figure 43 illustrates the difference in oxygen content (as the main focus) as a function of reaction temperature. As revealed in the AES depth profile result, there is a reduction in oxygen content from the as-received state (base alloy) by as little as 50ppm (at 200°C) and as much as 150ppm (at 180°C). A reduction in nitrogen content is also apparent, but is not necessarily directly correlated to the gaseous N_2 level as detected by the RGA during the fluorination experiment.

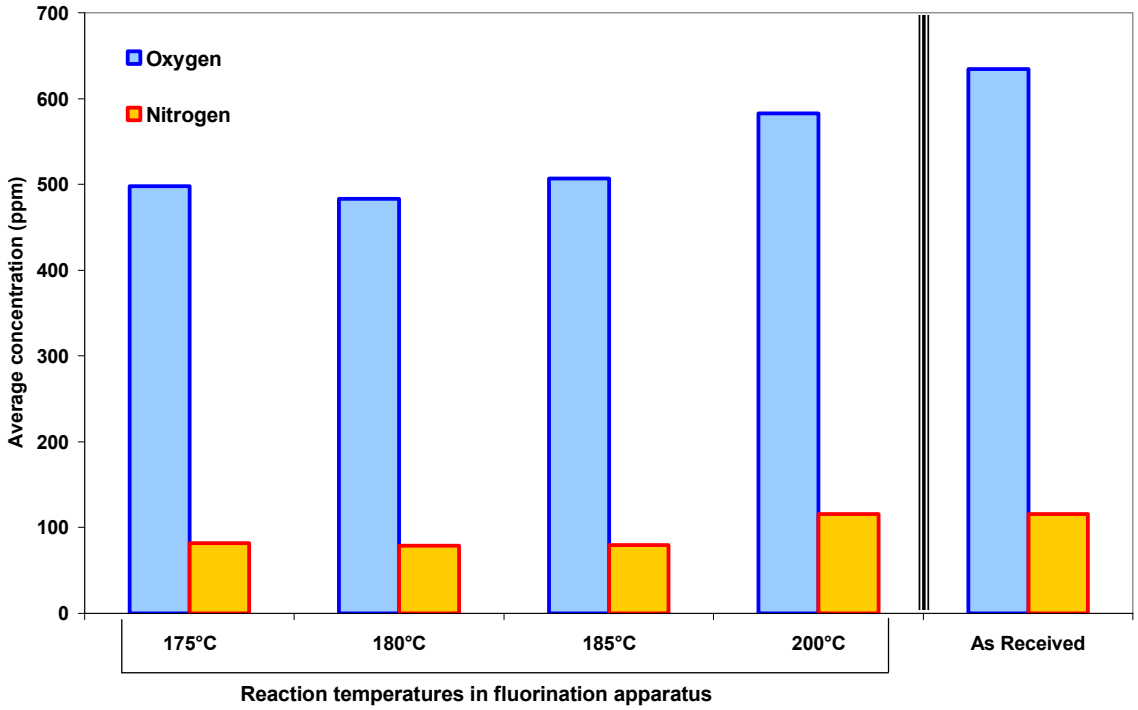

Figure 43: Bulk oxygen and nitrogen levels in fluorinated flake samples, MQP-11-HTP.

An important aspect of the surface passivation approach is the fluoride's ability to resist or reduce the rate oxidation at elevated temperatures, which it would be exposed to during injection or compression molding. Thermogravimetric analysis on a collection of particles in dehydrated air provided this critical performance information. It is evident from Figure 44 that at a fluorination temperature of 185°C, the fluoride coating has perhaps been developed with near optimum growth conditions, thereby providing a greater resistance to oxidation at 300°C. In comparison to the non-treated material (as-received), the fluorinated samples exhibit a reduction in rate of oxidation of nearly 60-70%, for 175°C and 185°C reaction

temperatures, respectively. It is noticed that at a fluorination temperature of 200°C, the initial resistance to oxidation is less, however maintains a similar rate after it reaches 300°C and is held at that temperature for the specified time of 10 minutes.

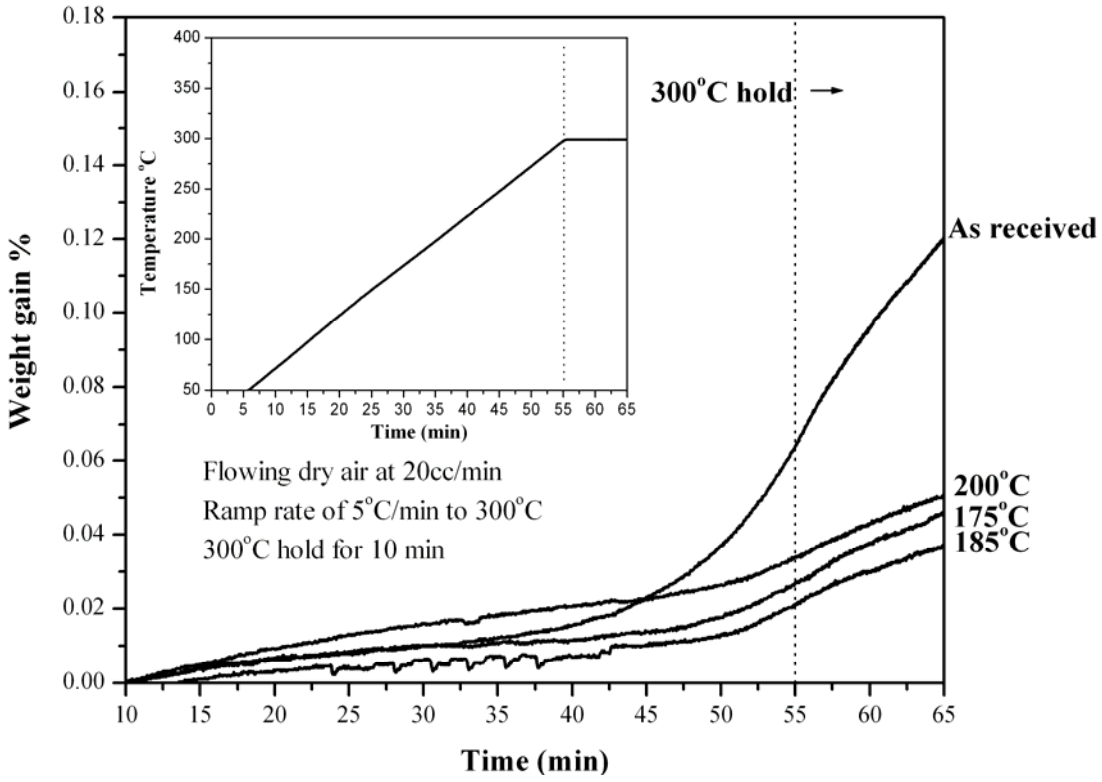

Figure 44: TGA analysis on fluorinated flake particulate at 175, 185, and 200°C in comparison to an as-received (nonpassivated) sample.

4.3.2.2 In situ HPGA Fluorination

In order to obtain surface chemistry information, x-ray photoelectron spectroscopy was performed on HPGA particles (<45μm) that had minimal exposure to atmosphere as well as samples that were exposed to air for more than 24 hours, or as indicated. Initial spectra reveal the dominant elements on the surface of the particles prior to Ar^+ ion etching for depth profiling.

Referring to Figure 45, elemental analysis of characteristic binding energies confirms the presence of yttrium (Y-3p1, 3p3, 3d, 3s), neodymium (Nd-4d, 3d5), oxygen (O-1s), and fluorine (F-1s) on the unexposed particle surfaces of the in situ fluorinated powder from the first NF_3 run, GA-1-66. The labeled iron peaks (Fe-2p, 3s, 3p) are minimal in comparison to the other element peaks and even absent at the Fe-3s unique location. This suggests the surface chemistry is primarily composed of some type of RE fluoride or RE oxyfluoride as previously stated for the fluorinated flake particulates. Deconvolution of the peaks is necessary to correctly identify all the remaining peaks present and to obtain quantitative data pertaining to relative concentrations; however this step is quite challenging and nearly impossible considering the number of constituents within the alloy and the amount of overlapping between characteristic binding energies [75].

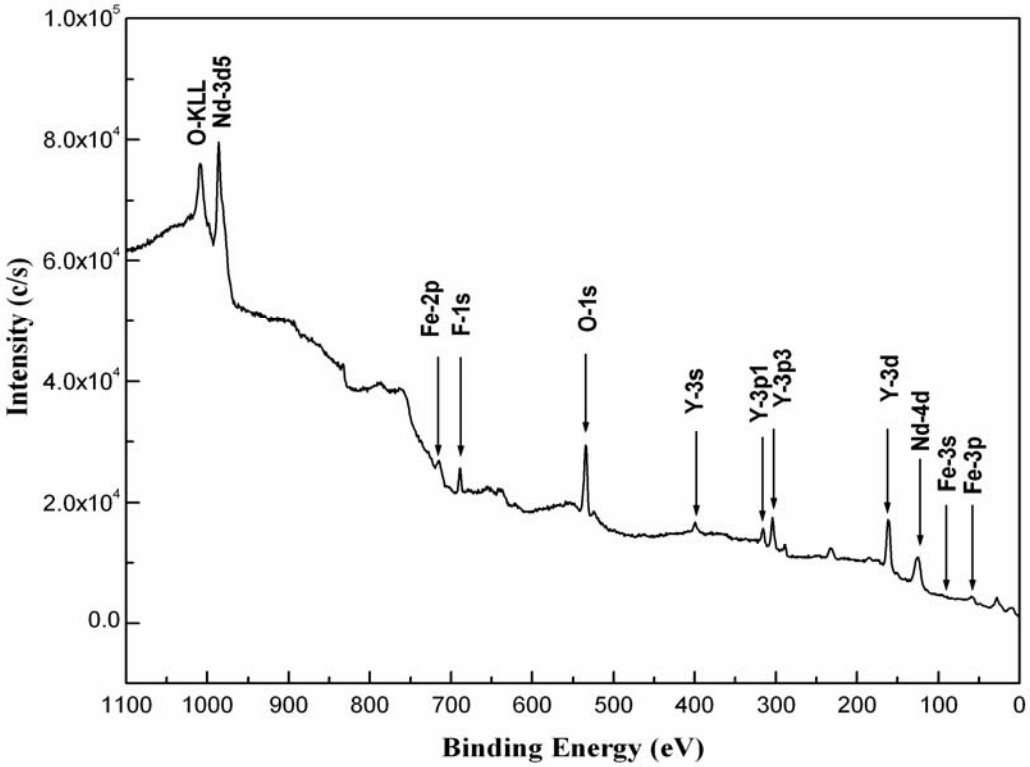

Figure 45 : X-ray photoelectron spectroscopy (XPS) spectrum of in situ fluorinated GA-1-66 powder (<45μm), unexposed to air.

Surface chemistry analysis with XPS is certainly a useful tool for examining relative concentrations of constituent elements. An important aspect of this tool is its ability to perform depth profiling in order to determine an effective thickness of a coating. Unfortunately, relating the method to a spherical particle, a direct thickness cannot be determined without applying mathematical models that account for portions of the curved surface being shaded from either x-ray incidence and/or electron escape. These models also are alloy specific and would require additional information on electron interactions with the particular crystal structure. Fundamentally, application of flat surface equations will actually overestimate the thickness of the passive layer on spherical particles by a factor of 2 for thin layers [76]. In any case, depth profiling in the XPS still provides a rough estimate as to the scale and architecture of surface passivation.

Depth profiling with the use of the XPS system on the ensemble surface of a collection of spherical particles provides useful information about the extent of the passivation kinetics, in

particular, what thickness of fluoride layer is sufficient for protection against increased oxidation rates. Figure 46 is a three dimensional depth profile of each respective element found in the initial XPS surface spectrum. Intensity (c/s) of the signal is displayed in the z-axis, binding energy (eV) in the x-axis, and sputtering time (sec) in the y-axis (going into the page).

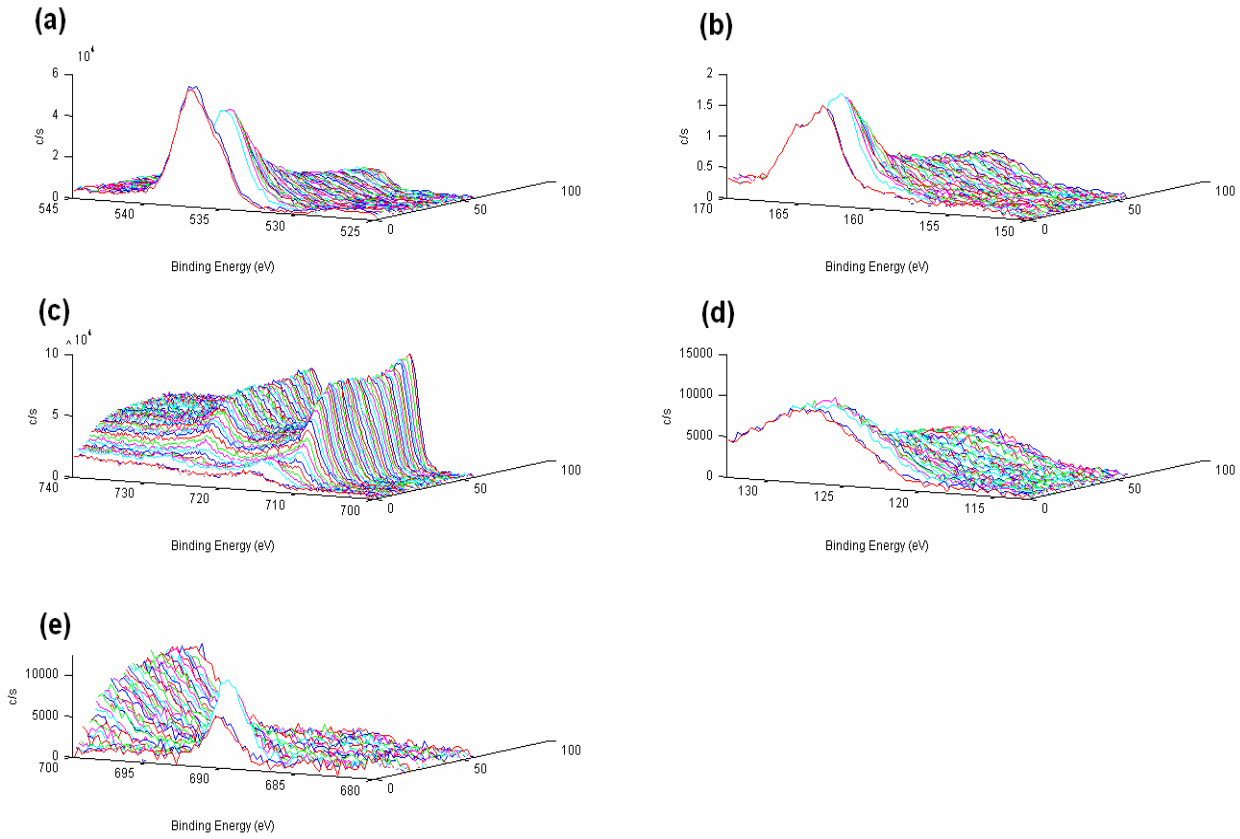

Figure 46 : XPS depth profiles of unexposed in situ passivated powder GA-1-66. (a) Oxygen 1s peak; (b) Yttrium 3d peak; (c) Iron 2p peak; (d) Neodymium 4d peak; and (e) Fluorine 1s peak.

After each sputtering cycle, a spectrum was taken of the sputtered area and then combined to produce the depth profile. The profiles can be correlated to a numerical depth considering the pre-mentioned XPS sputtering rate of 1nm/min on a SiO_2/Si standard. A quantitative depth analysis at this time is tentative at best though, as the etch rate depends directly on the composition of the alloy and the "roughness" of the sample surface and should be compared to a standard with a smooth planar geometry of the alloy in question. Regardless, it is clear

from Figure 46 that the rare earth elements, Y (b) and Nd (d), are bonded with fluorine (e) and oxygen (a). Their intensities decrease notably in parallel with fluorine and oxygen. Fluorine disappears from the surface after only a few etch cycles, suggesting that the penetration of the passivation reaction was kept to a minimum of 10-15Å by using a low exposure temperature and a small concentration of NF_3 gas. The characteristic Fe peaks (c) begin to increase in intensity as the etching process moves into the bulk of the sample as one would expect of an alloy consisting of more than 80% by weight Fe.

To verify this unique approach to in situ fluorination processing, a nonfluorinated RE-Fe-B alloy XPS spectrum from GA-1-52, produced with typical previous atomization parameters, was compared, Figure 47, to the coated powders: GA-1-66, GA-1-100, and GA-1-106. To simplify the diagram, only the range of binding energies from 500 to 740eV is shown to illustrate the difference in fluorine and oxygen content on the surface. It is apparent from this spectral comparison that a fluoride structure (F-1s) formed during the first attempt (GA-1-66) and was increasingly more successful as demonstrated by the relative increase in the characteristic fluorine peak intensity going from GA-1-100 to GA-1-106. It should also be mentioned that a slightly lower oxygen peak (O-1s) is evident, also as a result of this approach.

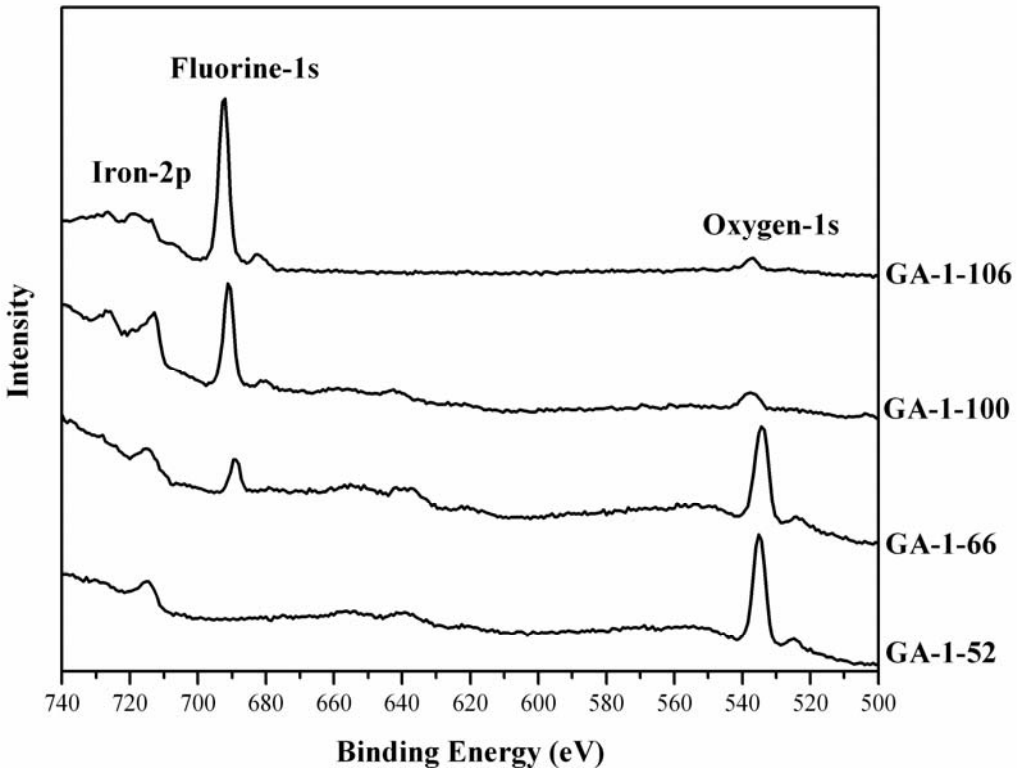

Figure 47 : XPS comparison spectra between different unexposed (<45μm) HPGA particles, revealing a reduction in surface oxide as presence of fluorine increases. GA-1-52 is the nonfluorinated atomization run and GA-1-66 thru GA-1-106 are successive in situ fluorination runs.

To evaluate the durability of the passive fluoride layer, a powder sample of GA-1-66 was exposed to ambient air for more than 24 hours before being re-examined with XPS. Figure 48 shows the unexposed and exposed XPS spectrums of the same sample. It is believed that the sharp increase and minor shift in the O-1s peak is associated with adsorption of ambient moisture on the particle surfaces that was converted to residual oxygen. The F-1s peak also is slightly less in intensity after exposure, which is also attributed to ambient oxidation of the surface of the powder that masks the signal [75].

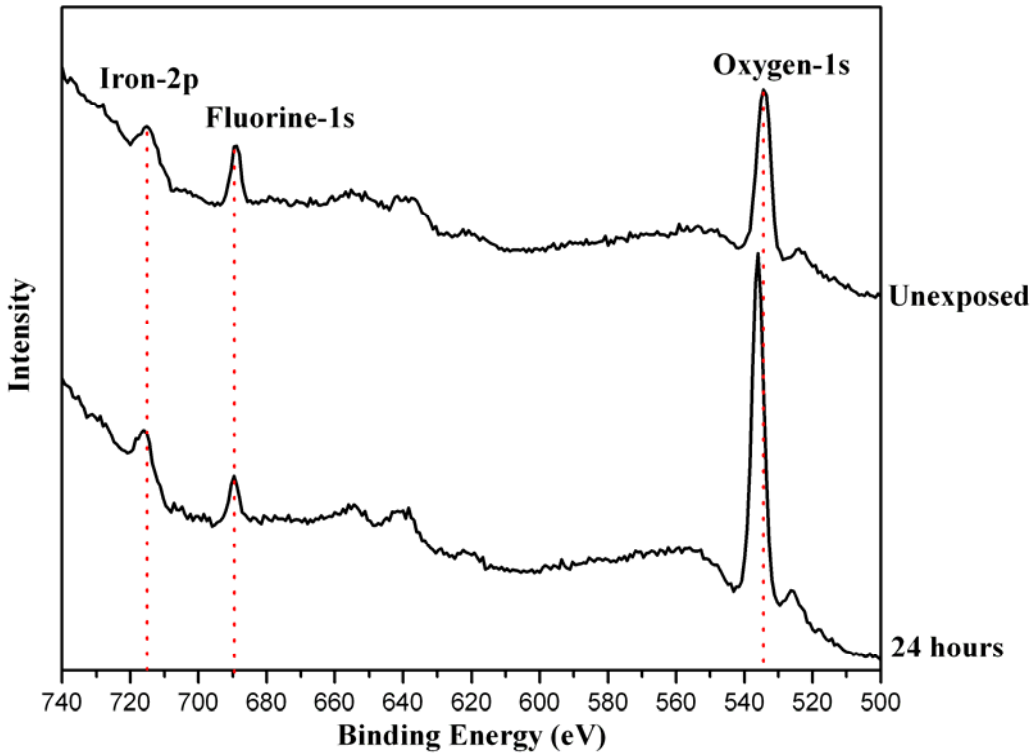

Figure 48 : XPS spectra of fluorinated GA-1-66 (dia. <45µm) unexposed and after 24 hours exposure to ambient atmosphere.

A similar approach was taken to evaluate GA-1-100, as seen in Figure 49. The sample was initially exposed to ambient air for 10 minutes before being re-examined with XPS and then again at 16 hours. As before, the sharp increase and minor shift in the O-1s peak is associated with adsorption of ambient moisture on the particle surfaces that was converted to residual oxygen. The F-1s peak also is slightly less in intensity after exposure, which is also attributed to ambient oxidation of the surface of the powder that masks the signal. The second exposure however, reveals that the fluoride is perhaps reduced by the oxidation of the surface as indicated by the significant reduction in the fluorine peak and change in oxygen peak, this time referring to oxidation and not simply adsorption of ambient moisture. This result indicates that the coating is most likely inadequate or not uniform over the entirety of the surface.

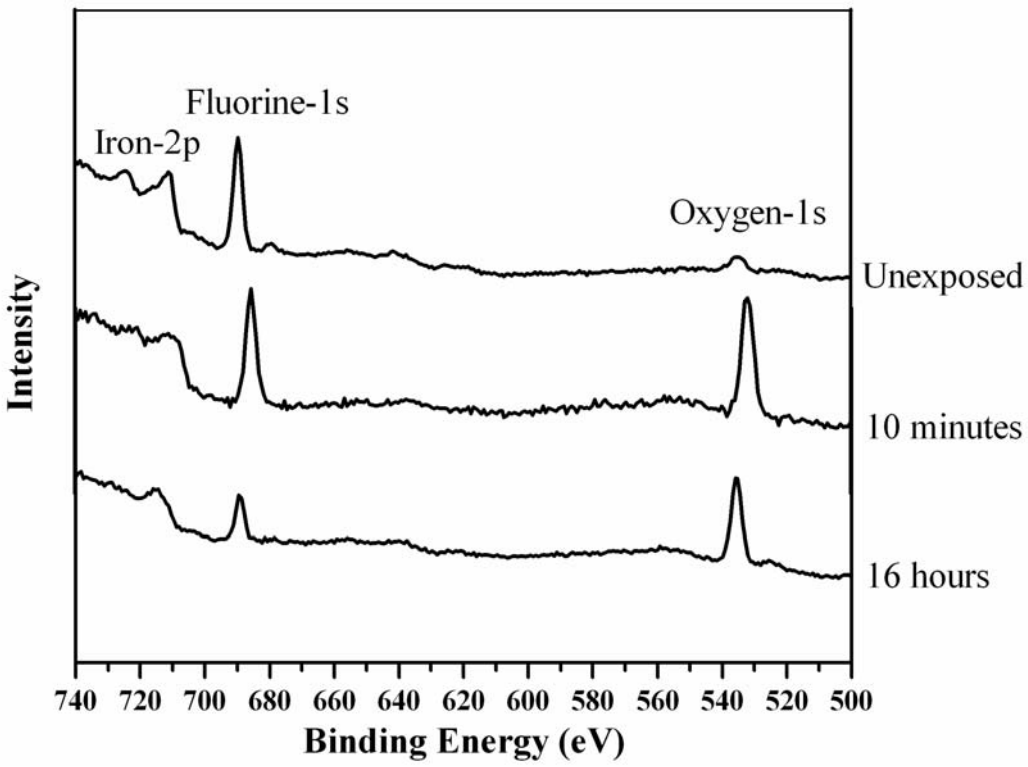

Figure 49: XPS spectra of fluorinated GA-1-100 (<45μm) in the unexposed state, 10 minutes, and 16 hours exposure to ambient atmosphere.

The most promising result, thus far, has been the behavior of GA-1-106 as demonstrated in Figure 50. The initial XPS spectrum (unexposed) displays the relative intensity of the fluorine peak height in comparison to an almost absent oxygen peak. After ambient air exposure for 20 hours, the fluorine peak intensity drops noticeably as the oxygen peak increases just as previous results have shown. Yet, after 6 days of exposure and re-examination of the surface, the surface structure is nearly the same as the 20 hour exposure with a healthy level of fluorine still present. This result indicates the coating may not completely prevent all oxidation, but it limits the extent of oxidation to a depth of penetration.

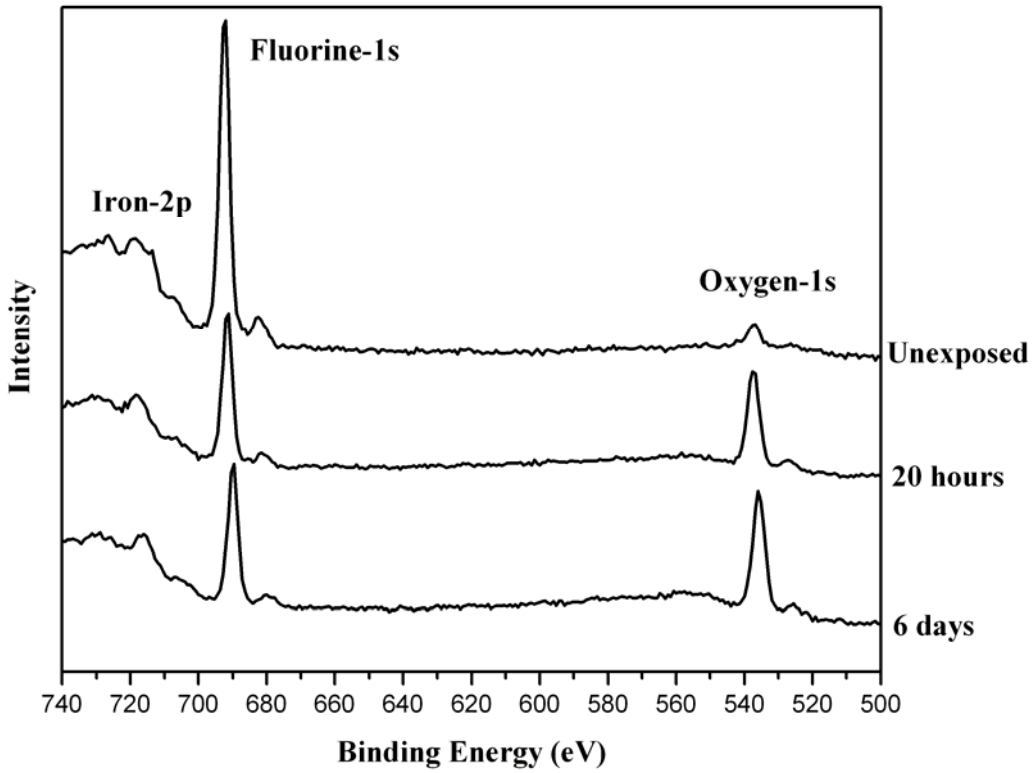

Figure 50: XPS spectra of fluorinated GA-1-106 (<45µm) in the unexposed state, 20 hours, and 6 days exposure to ambient atmosphere.

Table IX indicates the difference in oxygen concentration of powder samples in the unexposed condition. Typical magnet atomization runs, nonpassivated, have oxygen concentrations around 1800ppm or above. Passivation with NF_3 gas was capable of reducing this concentration to 1/6 of that value at 343ppm (GA-1-106).

Table IX: LECO analyzer results for different HPGA runs.

HPGA <45μm powder	Average O_2 concentration (ppmw)
GA-1-52	1800
GA-1-66	585
GA-1-100	904
GA-1-106	343

In addition, measurement of weight gain caused by thermal oxidation provides insight into the passive layer's ability to reduce the rate of oxidation at increased temperatures. Figure 51 contrasts the difference in weight gain over time at increased tempertures in dehydrated air between nonfluorinated GA-1-52 and in situ fluorinated powders of a similar alloy. The passive layer apparently provides a mechanism for reducing the rate of oxidation at 300°C.

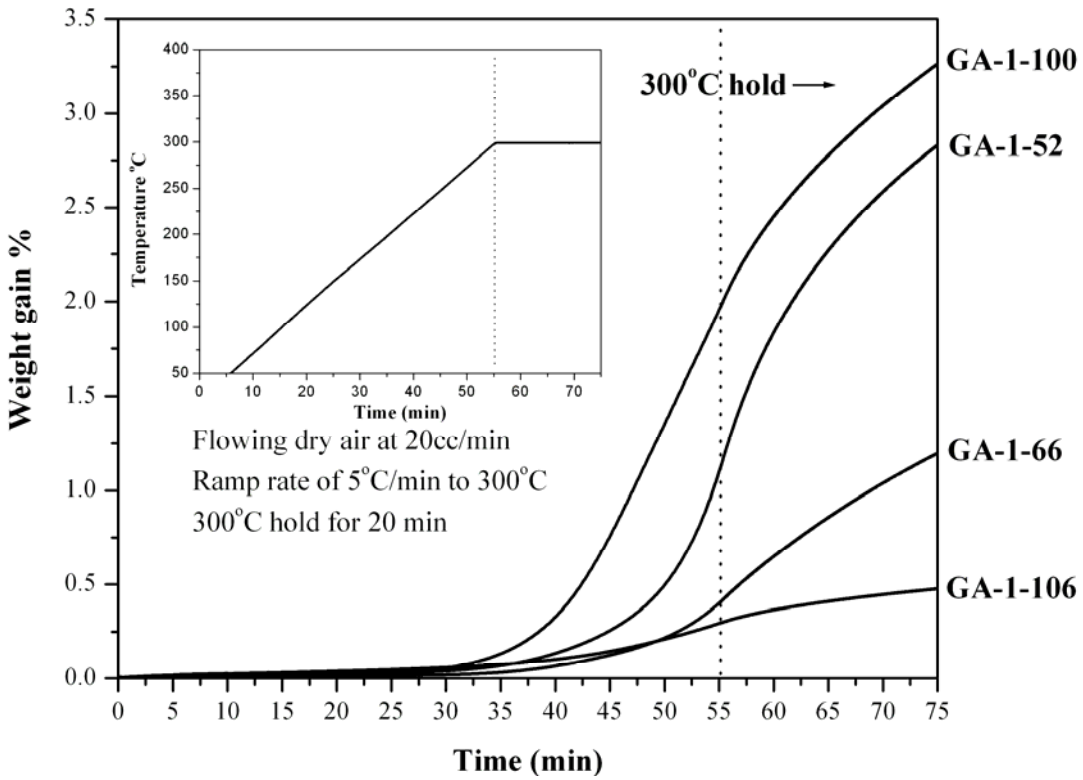

Figure 51 : Weight gain on a collection of <45μm HPGA particles as measured with the TGA. GA-1-66, GA-1-100, and GA-1-106 are in situ fluorinated. GA-1-52 is a nonfluorinated atomization run.

4.4 Polymer Bonded Magnets

The warm pressed magnets, composed of 60vol% as-received MQP-11-HTP, 40vol% PPS and supplied to Arnold Magnetic Technologies, Figure 52, were measured for physical properties, i.e. weight, density, etc., after being machined to a final shape to obtain a permeance coefficient (P_C) of 2. This is a characteristic of geometry of the magnet which accounts for a magnet's susceptibility to de-magnetization [73]. Therefore, to evaluate and maintain comparable magnetic values, the samples were machined with appropriate length to diameter ratios to achieve a $P_C = 2$. Finished magnets were subjected to a Short Term Irreversible Loss Test (STILT) and a Long Term Irreversible Loss Test (LTILT) to determine their commercial viability based on sustained performance level and reliability.

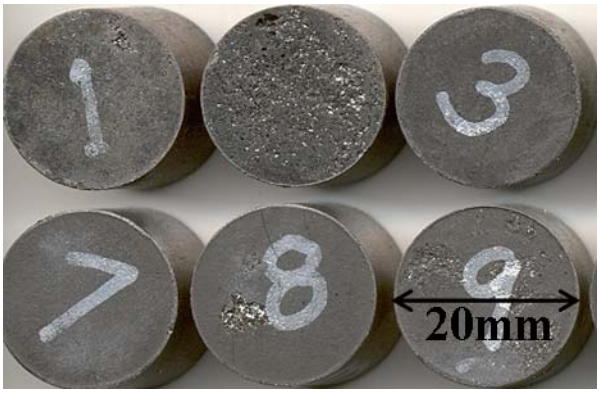

Figure 52: Compression bonded magnet samples produced for STILT and LTILT testing.

The STILT and LTILT graphs, Figure 53 and Figure 54 respectively, are plotted as a function of percent of initial flux and directly reveal sustained performance levels of the Ames Laboratory alloy (of ribbon form) MQP-11-HTP in comparison to its commercial counterpart, Magnequench^{TM} MQP-14-12. The STILT results show that the difference in flux loss after exposure to a temperature of 200°C is less than 1% between the Ames Lab alloy (being slightly less) and the commercial alloy. LTILT results reveal the difference between the alloys is again negligible, being less than 1%, after exposure to a temperature of 150°C for over 7,000 hours. Also, both environmentally tested magnets begin to plateau in flux loss suggesting degradation of each alloy behaves similarly with time of exposure.

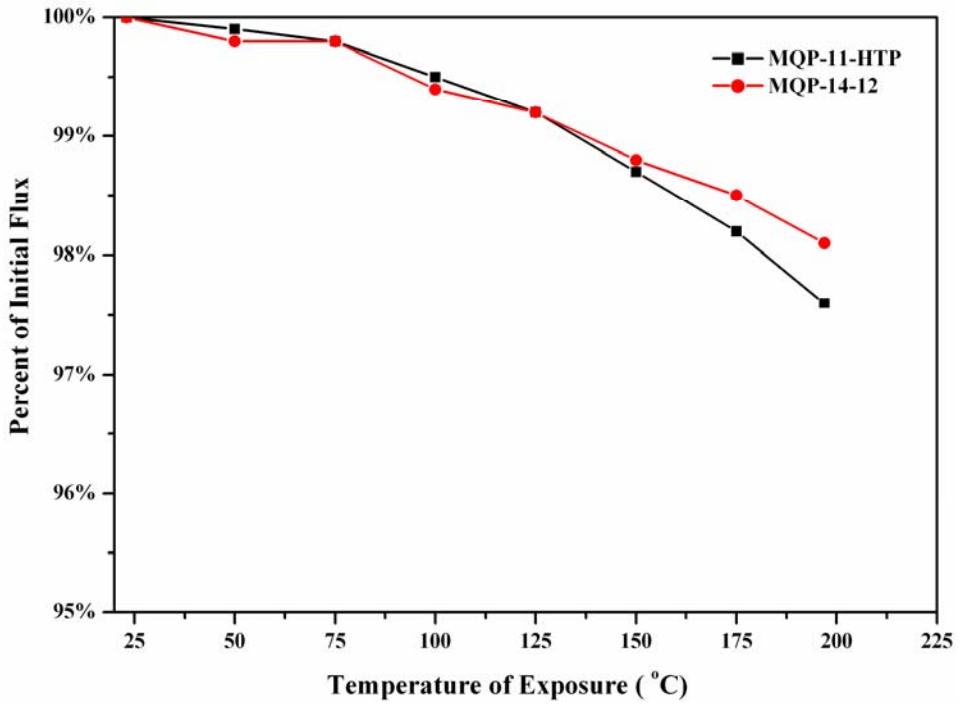

Figure 53: Short Term Irreversible Loss Test (STILT) on PPS bonded magnets with a $P_C = 2$.

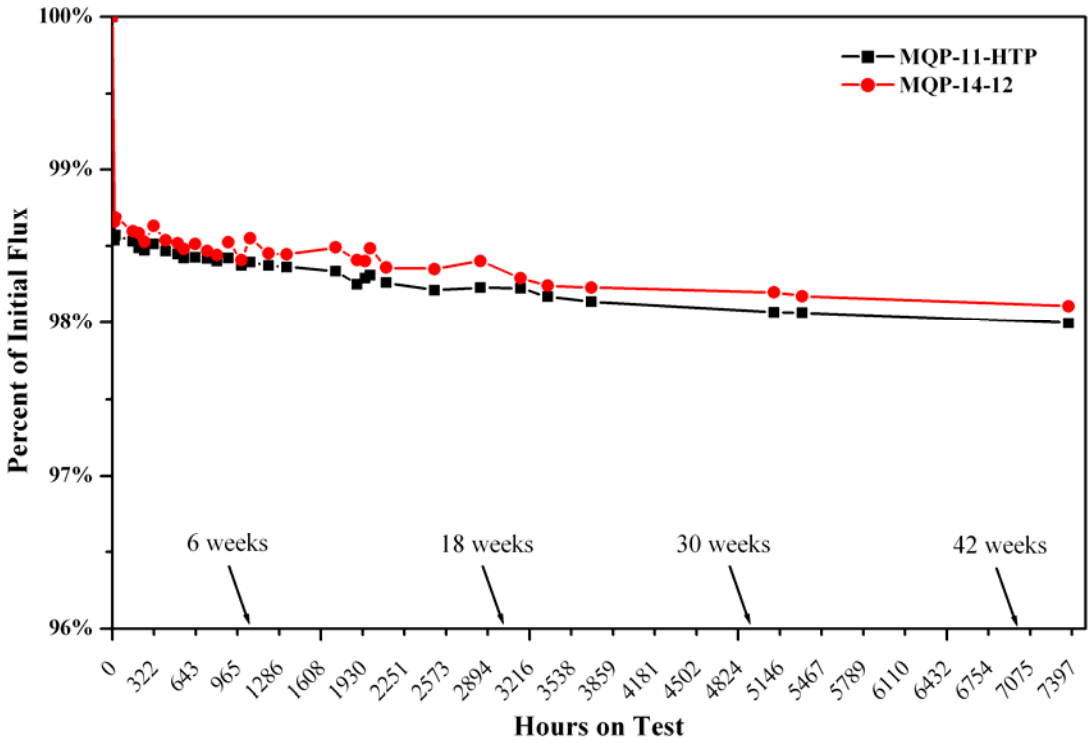

Figure 54: Long Term Irreversible Loss Test (LTILT) on PPS bonded magnets with a $P_C = 2$.

5. DISCUSSION

The alloy design iterations via melt spinning are proven to be very promising as these steps reveal the effects of adding Zr and TiC to the alloy in order to promote uniform crystallization and refine the grain size. Before the additions, typical grain sizes were on the order of 200nm for the base alloy $YDy_2Fe_{14}B$. As noted previously, the addition of Zr was capable of reducing the grain size down to 65nm with optimal magnetic properties; however 50nm grains were possible with increased amounts of Zr, leading to reductions in magnetic properties. Through judicious additions of TiC, an additional grain boundary and domain wall pinning mechanism was established within the alloy. The TiC addition, in conjunction with Zr, produced grains on the order of 50nm, enhancing $(BH)_{max}$ beyond that of only the optimized Zr addition. By adjusting the alloy for use in HPGA, the ideal processing route for manufacturing bonded permanent magnet particulate, a significant amount of particles were capable of exhibiting a more controllable and optimized microstructure as seen in the microstructural analysis of GA-1-66.

The subsequent gas atomized alloys, GA-1-100 (helium atomized) and GA-1-106 (argon atomized), were intended to utilize the substitutional behavior of ZrC for TiC, in an effort to directly crystallize the hard magnetic 2-14-1 phase with optimized grain size. To do this, the switch from helium to argon atomization gas, coupled together with the kinetic behavior of ZrC, is expected to result in a change in heat transfer rate [35][77] allowing for increased control over solidification structure. However, this result has yet to be realized as GA-1-100 required a post atomization anneal to crystallize and optimize the grain structure and GA-1-106 was significantly off in composition. Thus, their microstructural and magnetic analysis, to aid in understanding alloy development as an overall project goal, was not included within this thesis. On the other hand, the RGA and surface analysis data on these alloys provided useful and reliable information on the success of the first trials of in situ HPGA fluorination.

In addition to directly crystallizing a desired microstructural length scale (although not yet reached) in magnetic particulate through HPGA processing, gas atomization is capable of producing a high yield of fine spherical particles with a tight distribution, as revealed in Figure 55. Three of the HPGA alloys were chosen to illustrate a size distribution analysis, as a typical result from a Microtrac laser scattering particle size analyzer, and respective average particle size, d_{50}, and standard deviation, d_{84}/d_{50}. Having a yield of approximately 90% below 45µm for nearly all three runs is an ideal processing result and a desirable size range for polymer bonded magnet and injection molding (IM) manufacturing since spherical particles of this range have a high packing density. Through using HPGA processing to produce ideal spherical magnetic particulate, the need for crushing and grinding (a requisite for utilizing melt spun particulate) to reduce particle size is eliminated.

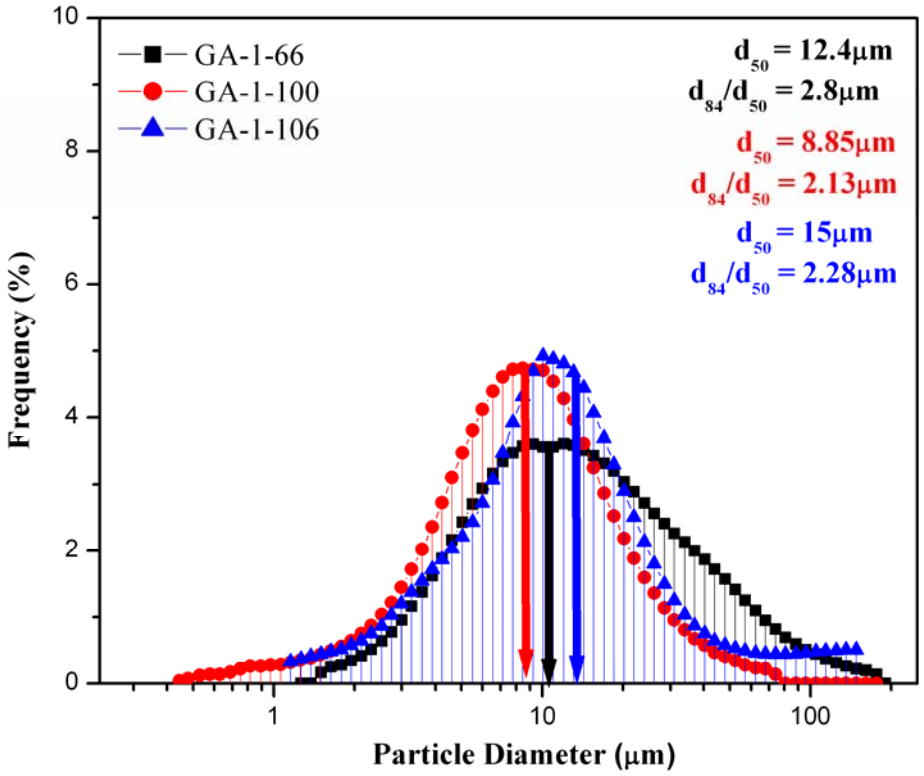

Figure 55: HPGA particle size distribution analysis on GA-1-66, GA-1-100, and GA-1-106. The average particle size (d_{50}) and standard deviation (d_{84}/d_{50}) of each atomization run are reported in the upper right of the figure.

The production of fine, especially <20μm, spherical particulates, results in a tremendous amount of surface area that is highly sensitive and susceptible to ambient oxidation and corrosion. In order to protect the particles during handling and elevated temperature polymer bonding, the method of in situ HPGA surface fluorination was successfully developed although may not be fully optimized as the results show there is the ability for continued surface passivation improvement. It has been shown that the novel approach to passivation of spherical particulate while "in flight" is capable of forming RE fluorides or RE oxyfluorides on the first several monolayers, predominantly YF_3 and YOF as was also reported by Buelow [39]. These results are in good agreement with previous research on fluorination and reactivity of fluorine in contact with metallic surfaces at elevated temperatures [57][78][79][80]. XPS results confirm that the thermodynamically favored rare earth compounds are formed, most likely at the expense of their respective oxides as supported with residual gas analysis and oxygen content analysis, and are able to persist upon exposure to air.

As was revealed through an XPS comparison trend, refer back to Figure 47, the fluorine content on the surface of a collection of unexposed atomized particles increased as the oxygen peak decreased with each successive in situ fluorination trial. Although the same NF_3 injection parameters were used during the first two trials, GA-1-66 and GA-1-100, the injection halo was lowered approximately 2 feet below its previous chamber location for GA-1-106. This modification may be a reason as to why GA-1-106 exhibited a sharp (and desirable) increase in fluorine content on the particle surfaces. This adjustment was to anticipate an increase in powder particle temperature as a result of changing the atomization gas from He (as used for GA-1-66, GA-1-100) to Ar for GA-1-106, where Ar has a lower heat capacity and thermal conductivity than He. Therefore, it was thought that lowering the injection halo would maintain a similar temperature zone for initiation of particle surface fluorination.

In Figure 56, the temperature zone profile (as measured below the NF_3 injection halo within the atomization chamber) for each in situ HPGA fluorinated run is compared. The trend for

the first run GA-1-66, which used a different temperature data collection system, is noticeably low in temperature throughout the length of the run and peaks at 137°C after about 90 seconds of a run that lasted 102 seconds. However, in stark contrast, GA-1-100 and GA-1-106 exhibit very similar temperature profiles which peak at 276°C and 260°C, respectively, nearly 30 seconds after the start of their runs. The difference in max achieved temperature and cooling behavior is perhaps a factor in creating processing conditions which result in the formation of more ideal surface fluorides as revealed through surface analysis on GA-1-106.

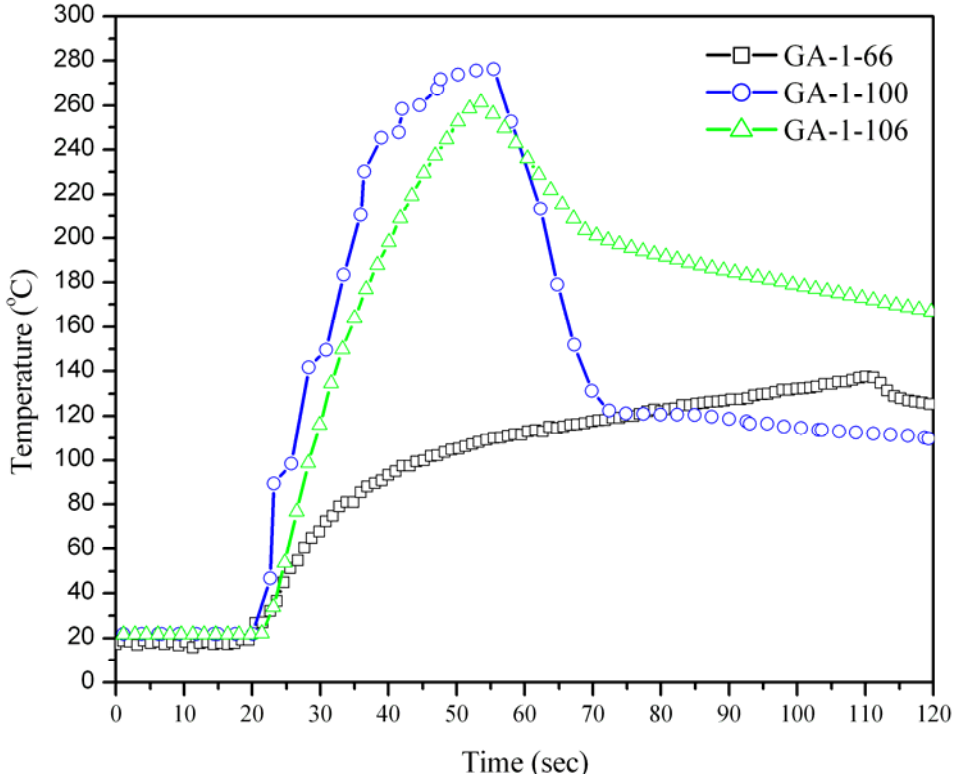

Figure 56: Halo temperature profile comparison between in situ HPGA fluorination runs.

Based on the XPS and TGA results, the setup for GA-1-106 proved to be a promising adjustment and is suggested to be the ideal approach at passivating particles in situ, especially with Ar gas as the atomization gas. Certainly, a change in NF_3 concentration would have an effect on passivation kinetics during in situ HPGA fluorination and an increase in concentration could possibly lead to a thicker coating. However, the most recent

surface analysis results reveal that the fluorine was capable of reducing the amount of oxygen present in the alloy to 343ppmw, as well as providing a stable film which changed little after air exposure for 20 hours or more.

An accurate fluoride thickness measurement, as inferred from the XPS depth profile, revealed a fluoride depth of approximately 10-15Å for GA-1-66. A depth profile for GA-1-106, not presented, was inconclusive as fluorine was never completely removed from the surface after etching for more than 30 minutes. This is most likely attributed to shadowing and curvature effects of the spherical particles that were analyzed; hence a fluorine binding energy was continually detected. As mentioned previously, XPS depth profiling is not ideal for curved surfaces and therefore simply supplies a conceptual thickness instead of an accurate value. In any case, auger analysis should provide a more precise thickness value. However, the GA-1-106 sample was not fully analyzed in time prior to this analysis but is believed to have a coating thickness within the same range as exhibited by GA-1-66 at 10-15Å.

The development and modification of a fluidized bed for controlled fluorination allowed for a systematic study to determine optimal fluorination parameters and coating thickness on flat samples of a similar alloy, MQP-11-HTP. The addition of an oxygen-gettering furnace and vacuum pump to the experimental fluidized bed increased atmosphere control considerably and encouraged reproducibility in results. The RGA analysis during fluorination in the fluidized bed was the base measurement for determining the direction of the experiments. Principally, the level of N_2 that was produced provided insight into the extent of the surface reaction as N_2 was a byproduct of the reaction between NF_3 and the alloy surface. An analysis of RGA data from different set fluorination temperatures revealed an increase in N_2 production with an increase in temperature, as was expected. These samples, as tested in a TGA, determined the most effective fluorination treatment as produced in the fluidized bed method. Fluorinated flake particulate, with the reaction temperature held at 185°C and an NF_3 concentration of 0.05%, proved to be the most stable and resistant fluoride coating that was generated as a result of this work. Auger depth profile analysis concluded that the

fluoride layer persisted to a depth of 12-20Å into the particulate. This measurement is in fair agreement with the thickness values obtained on in situ fluorinated spherical powders as well as previous results reported by Buelow [39] on fluorinated flake.

Additionally, kinetic information on the activation energy needed to initiate the onset of oxidation at 300°C may prove to be useful for future development of the fluorination mechanism. The Arrhenius equation relates the rate of a reaction, in this case the rate of oxidation, with the given temperature. Therefore, this relationship, equation 13, can be used to calculate and compare specific activation energies, E_a, needed to initiate oxidation of nonfluorinated and fluorinated magnet particulate.

$$k = A\exp^{(-E_a/RT)} \tag{13}$$

The rate constant, k, is the slope of the time vs. weight gain curve during the 300°C TGA hold. A, a constant, is assumed to be 1 in this case for simplicity, R is the gas constant 8.314 J/mol·K, and T the absolute temperature in Kelvin, 573.15 K for these calculations. As an example for determining the rate constant and respective activation energy, Figure 57 illustrates the location in the GA-1-66 TGA curve for extracting the rate constant value. The following equations 14-17, detail a brief calculation for $E_{a(\text{GA-1-66})}$ based on the slope from Figure 57. Substituting values into the Arrhenius equation and taking the natural logarithm of both sides of the equation provides an experimental determination of E_a. The constant from applying the natural log is ignored in this case, yet could be experimentally determined through additional TGA analysis at different holding temperatures as is also true for A.

$$0.01782 = A\exp^{(-E_a/8.314*573.15)} \tag{14}$$

$$\ln(0.01782) = \ln(1) + \ln(\exp^{(-E_a/8.314*573.15)}) \tag{15}$$

$$-4.0271 = 0 + (-E_a/8.314*573.15) + \text{constant} \tag{16}$$

$$E_{a(GA-1-66)} = 19.18 kJ/mol \tag{17}$$

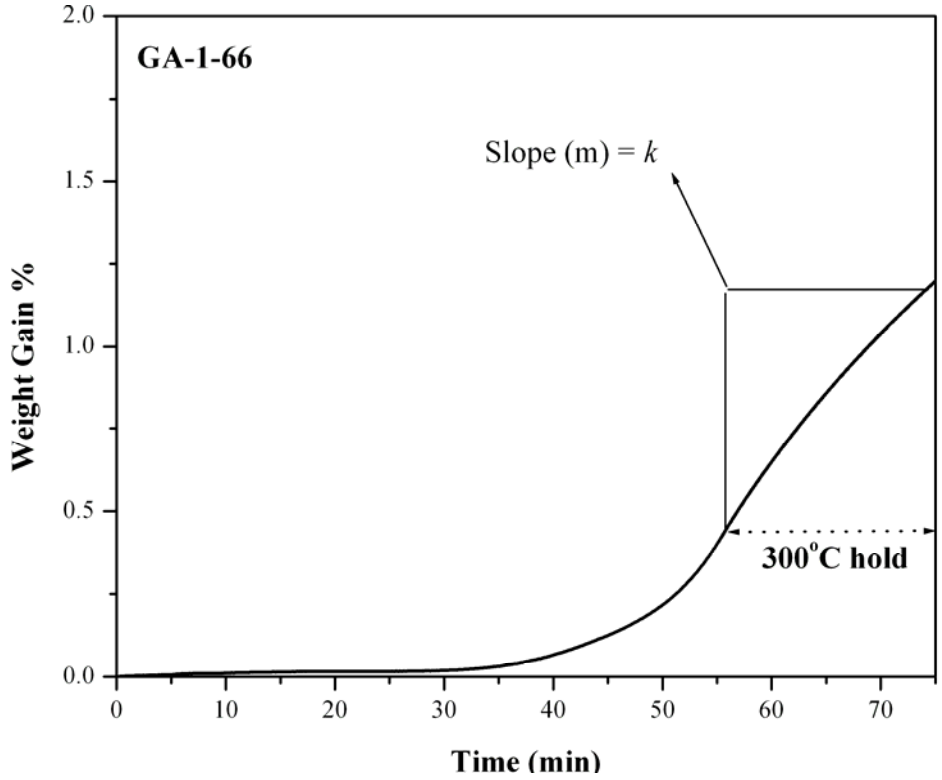

Figure 57: TGA analysis of atomized powder GA-1-66 revealing location of extrapolated rate constant, *k*, for determining the activation energy of oxidation at 300°C.

The results of the activation energy calculations for each sample previously analyzed in the TGA plots are charted in Figure 58. It is evident right away that the flake alloy results exhibit a higher E_a as a whole as compared to the spherical particle values. This is attributed to the difference in surface area (although not calculated here), where spherical particles, as already mentioned, have a very large surface area in contrast to flake morphologies, see Figure 59 for morphology contrast. Therefore, an additional surface energy factor and curvature effect should be taken into consideration as cause for the reduced E_a to initiate oxidation of atomized powder.

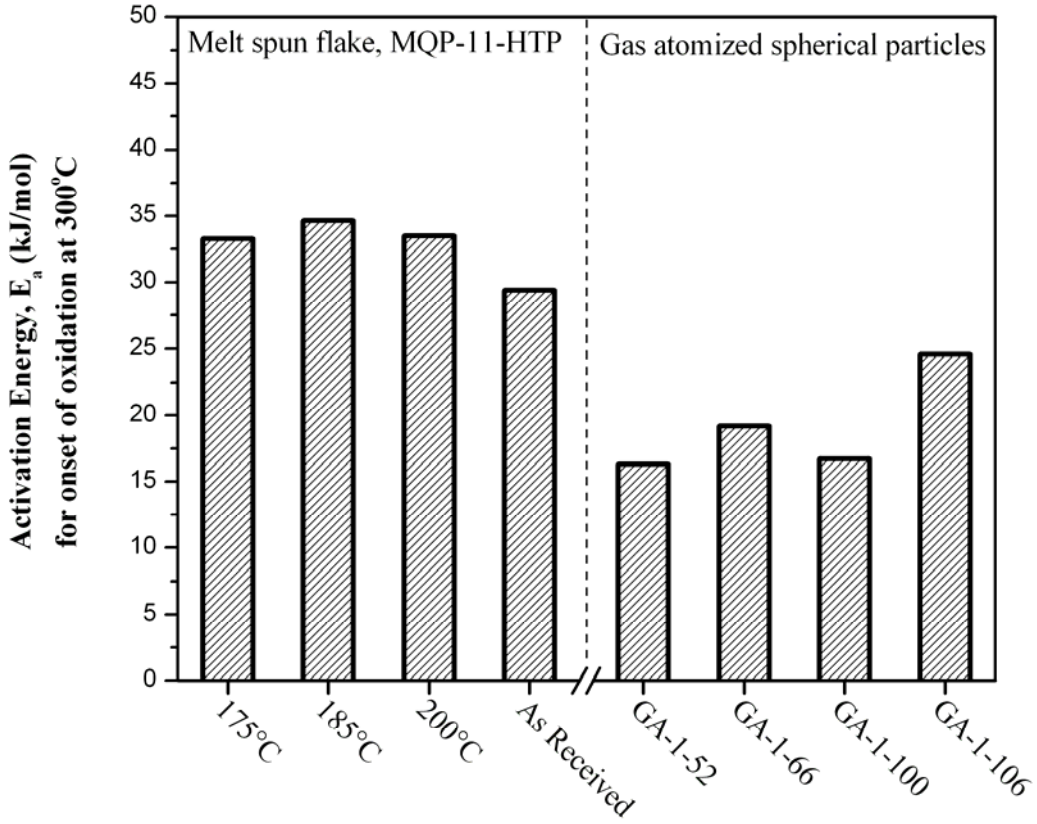

Figure 58: Activation energies for the onset of oxidation at 300°C, as calculated from the TGA results for both the fluorinated flake (at temperatures of 175, 185 and 200°C) and in situ HPGA fluorinated powder.

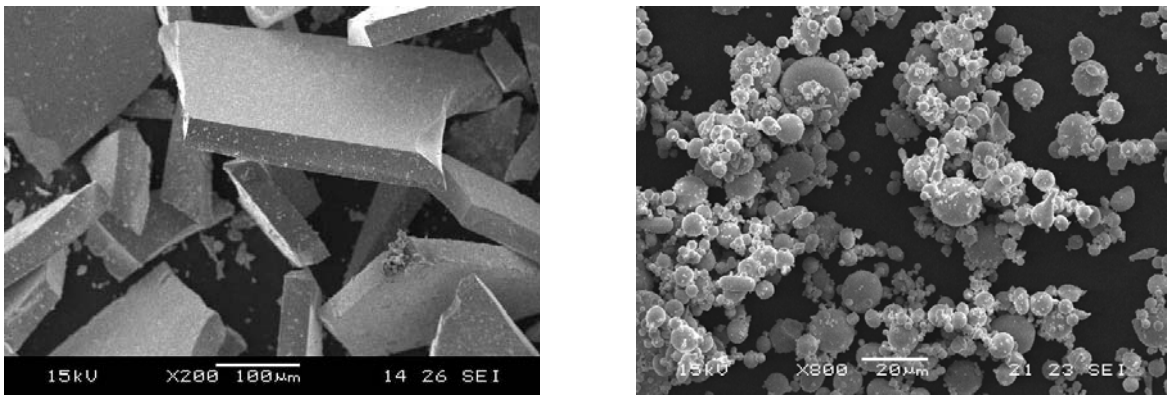

Figure 59: Contrasting morphologies of melt spun ribbon to HPGA particles (left) Melt spun magnet ribbon exhibiting flat surfaces and a high aspect ratio; (right) HPGA magnet powder revealing customary spherical shape and fine (<45µm) distribution.

In relation to one another, the fluorinated flake samples display fairly close values for E_a, however the 185°C fluoride coating temperature exhibits the greatest stability against oxidation at 300°C with a value of 34.65kJ/mol. In any case, a fluoride coating shows improvement over the as-received sample. The same trend is true for the in situ HPGA fluorinated samples where the nonfluorinated run, GA-1-52, shows the lowest E_a needed to initiate surface oxidation at 300°C. In comparison, GA-1-106 reveals the potential for achieving similar activation energies as possessed by flake particulate with a value of 24.56kJ/mol. This suggests that the fluoride coating on GA-1-106 is possibly more uniform than the previous runs and of adequate thickness.

Upon determination of the optimal parameters for fluidized bed fluorination, at 185°C with 0.05%NF_3 concentration, increased sample sizes (30g) of MQP-11-HTP were fluorinated and subsequently used to fabricate polymer bonded magnets for future, direct comparison to the already environmentally tested samples (STILT and LTILT). This stage is still in progress however, and the results will not be available in time to report. It is believed that the optimized fluorinated particulate in bonded form will demonstrate similar results as initially reported on a single, non-optimized fluorinated sample [39]. Where the non-optimized fluorinated bonded magnet displayed a reduced magnetic flux aging loss during STILT testing in comparison to a nonfluorinated bonded magnet of a similar alloy.

6. CONCLUSION

Rapid solidification processing has proven to be a reliable processing route for the production of isotropic $MRE_2(Fe+Co)_{14}B+Zr+TiC$ permanent magnet material. The hard magnetic properties are highly dependent on intrinsic and extrinsic factors brought about by alloy design and processing considerations. Through utilizing a lab-scale chill block melt spinner to perform alloy design iterations, small changes to the alloy can systematically be studied and further alloying steps predicted. Promising alloy enhancements have been translated for production via high pressure gas atomization, the ideal method for producing isotropic nanocrystalline $MRE_2Fe_{14}B$ for use in polymer bonded permanent magnets. The challenge has been to produce the same microstructural length scale in HPGA particles with the appropriate magnetic phase as seen in melt spun ribbon of the same alloy. Previous results reported [39][25][26][28], describe the initial steps of alloy development as well as the difficulty in producing HPGA powder exhibiting identical energy product $(BH)_{max}$ as that of the same alloy processed with melt spinning. Through recent judicious additions of Zr and TiC to the alloy, it has been shown that similar solidification morphologies can be produced in the finest of HPGA particle distributions to that seen in melt spun ribbon. Specifically, the ability to achieve high undercoolings has produced an ideally homogeneous microstructure consisting of fine nanocrystallites dispersed within an amorphous matrix. Annealing of the amorphous particles has led to a considerable amount of microstructural control where the current optimal grain size, 50nm, is a crucial factor in determining the magnetic properties.

Since oxidation and corrosion of the MRE-Fe-B magnetic material often leads to irreversible magnetic losses over time, the formation of rare earth-type fluorides (REF_3, REOF) on the spherical particle surfaces was attempted to prevent degradation prior to the polymer bonding step and to maintain magnetic performance. Initial in situ treatment results were shown to be successful at forming a passive fluoride layer on the order of 10-15Å on spherical powder, however it was essential to investigate effective fluoride thickness control. The development and use of a small scale modified fluidized bed apparatus provided a method for controlled

surface passivation of both flake and spherical magnetic particulate to allow discovery of a sufficient (but not excessive) fluoride thickness. As a result of this work and analysis, near-optimal fluidized bed conditions were established. The most promising surface passivation conditions have shown that a fluorination temperature of 185°C at a concentration of 0.05%NF_3 results in favorable (12-20Å thick) formation of a predominantly YOF and YF_3 surface structure. Even after a set of near-optimal fluorination parameters has been established with the fluidized bed, it is still a challenge to translate these to the in situ HPGA procedure where the environment is highly chaotic with non-steady state conditions in comparison to the fluidized bed.

REFERENCES CITED

[1]. W. Gilbert, *On The Magnet*, edited by Derek J. Price, Basic Books, Inc., New York. 1958.

[2]. J.D. Livingston, *Driving Force: The Natural Magic of Magnets,* Harvard University Press, Cambridge. 1996.

[3]. I.E. Anderson, W. Tang, and R.W. McCallum, "Particulate Processing and Properties of High-Performance Permanent Magnets," *International Journal of Powder Metallurgy*. 2004, vol. 40, issue 6, pp.37-60.

[4]. D. Jiles, *Introduction to Magnetism and Magnetic Materials*, Second Edition. 1998, Chapman and Hall, New York, NY.

[5]. O.N. Carlson, F.A. Schmidt, "Preparation of the Rare-Earth Fluorides," in *The Rare Earths* edited by F.H. Spedding & A.H. Daane, John Wiley & Sons, Inc., New York. 1961, 77-88.

[6]. J.F. Herbst, "$R_2Fe_{14}B$ materials: Intrinsic properties and technological aspects," *Reviews of Modern Physics*. October 1991, 63, 4, 819-898.

[7]. J.F. Herbst, J.J. Croat, F.E. Pinkerton, W.B. Yelon, "Relationships between crystal structure and magnetic properties in $Nd_2Fe_{14}B$," *Physical Review B*. 1 April 1984, 29, 7, 4176-4178.

[8]. A. Hütten, "Processing, Structure, and Property Relationships in Nd-Fe-B Magnets," *Journal of Metals*. March 1992, 11-15.

[9]. M. Sagawa, S. Fujimura, N. Togawa, H. Yamamoto, Y. Matsuura, "New material for permanent magnets on a base of Nd and Fe (invited)," *Journal of Applied Physics*. 15 March 1984, 55, 6, 2083-2087.

[10]. J.J. Croat, J.F. Herbst, R.W. Lee, F.E. Pinkerton, "Pr-Fe and Nd-Fe-based materials: A new class of high-performance permanent magnets (invited)," *Journal of Applied Physics*. 15 March 1984, 55, 6, 2078-2082.

[11]. L. Schultz, A.M. El-Aziz, G. Barkleit, K. Mummert, "Corrosion behavior of Nd-Fe-B permanent magnetic alloys," *Materials Science and Engineering A*. 1999, 267, 307-313.

[12]. A.S. Kim, F.E. Camp, "Improved Corrosion Resistance of Nd-Fe-B Magnets," *Journal of Materials Engineering.* 1991, 13, 175-182.

[13]. P. Campbell, *Permanent Magnet Materials and Their Application*. 1994, Cambridge University Press, Cambridge.

[14]. A.S. Kim, F.E. Camp, T. Lizzi, "Hydrogen induced corrosion mechanism in NdFeB magnets," *Journal of Applied Physics.* 15 April 1996, 79, 8, 4840-4842.

[15]. W. Liu, Y. Yang, Y. Meng, J. Wu, "The Effects of Surface Modification on the Properties of Bonded NdFeB Magnets," *Materials Transactions*. 2003, 44, 6, 1159-1162.

[16]. G.H.M. Koper, M. Terpstra, *Improving the Properties of Permanent Magnets, A Study of Patents, Patent Applications and Other Literature*. 1991, Elsevier Science Publishers LTD, London.

[17]. H.A. Davies, Z.C. Wang, "The role of sub-micron grain size in the development of rare earth hard magnetic alloys," *Materials Science and Engineering A*. 2004, 375-377, 78-83.

[18]. D. Brown, B.M. Ma, Z. Chen, "Developments in the processing and properties of NdFeB-type permanent magnets," *Journal of Magnetism and Magnetic Materials*. 2002, 248, 432-440.

[19]. J.J. Croat, "Current Status and Future Outlook for Bonded Neodymium Permanent Magnets (invited)," *Journal of Applied Physics*. April 1997, vol. 81, no. 8, pp. 4804-4809.

[20]. R.W. McCallum, Y. Xu, M.J. Kramer, I.E. Anderson, K.W. Dennis, "Permanent Magnet Alloy with Improved High Temperature Performance," ISURF 2935, filed 11 May 2005.

[21]. D. Givord, H.S. Li, J.M. Moreau, "Magnetic Properties and Crystal Structure of Neodymium-Iron-Boron ($Nd_2Fe_{14}B$)," *Solid State Communications*. 1984, 50, 497-499.

[22]. M. Boge, J.M.D. Coey, G. Czjzek, D. Givord, C. Jeandey, H.S. Li, J.L. Oddou, "The 3d-4f Magnetic Interactions and Crystalline Electric Field in the $R_2Fe_{14}B$ Compounds: Magnetization Measurements and Mössbauer Study of Gadolinium Iron Boride ($Gd_2Fe_{14}B$)," *Solid State Communications*. 1985, 55, 295-298.

[23]. Magnequench, Inc., *MQP^{TM} Isotropic RE-Fe-B Powders, Product Descriptions*, http://www.magnequench.com/products/pdf/MQP/MQP-S-11-9.pdf. [Accessed 30 May 2006].

[24]. N.L. Buelow, I.E. Anderson, R.W. McCallum, M. J. Kramer, W. Tang, and K.W. Dennis, "Comparison of Mixed Rare Earth Iron Boride Gas Atomized Powders to Melt Spun Ribbon for Bonded Isotropic Permanent Magnets," *Advances in Powder*

Metallurgy and Particulate Materials. Compiled by R.A. Chernenkoff and W.B. James, Metal Powder Industries Federation, Princeton, NJ, 2004, pp.230-244.

[25]. W. Tang, K.W. Dennis, Y.Q. Wu, M.J. Kramer, I.E. Anderson, and R.W. McCallum, "Studies of New YDy-Based $R_2Fe_{14}B$ Magnets for High Temperature Performance (R=Y+Dy+Nd)," *IEEE Transactions on Magnetics.* 2004, vol. 40, no. 4, pp.2907-2909.

[26]. W. Tang, Y.Q. Wu, K.W. Dennis, M.J. Kramer, I.E. Anderson, and R.W. McCallum, "Effect of Zr Substitution on Microstructure and Magnetic Properties of New YDy-Based $R_2Fe_{14}B$ Magnets (R=Y+Dy+Nd)," *Journal of Applied Physics*. 2005, 97, 10H106-1,3.

[27]. Y. Xu, M.J. Kramer, Y.Q. Wu, K.W. Dennis, R.W. McCallum, "The mechanism of magnetic properties improvements and microstructure refinement of Zr in $Nd_2Fe_{14}B$," *Journal of Applied Physics*. 2006, 99, 08B511(1-3).

[28]. W. Tang, Y.Q. Wu, K.W. Dennis, M.J. Kramer, I.E. Anderson, R.W. McCallum, "Effect of TiC addition on microstructure and magnetic properties for $MRE_2(Fe,Co)_{14}B$ melt-spun ribbons (MRE=Nd+Y+Dy)," *Journal of Applied Physics*. 2006, 99, 08B510(1-3).

[29]. D.J. Branagan, M.J. Kramer, R.W. McCallum, "Transition metal carbide formation in the $Nd_2Fe_{14}B$ system and potential as alloying additions," *Journal of Alloys and Compounds*. 1996, 244, 27-39.

[30]. O. Filip, R. Hermann, and L. Schultz, "Growth Kinetics and TiC Precipitation Phenomena in Nd-Fe-B-Ti-C Melts in Dependence on Cooling Parameters and Composition," *Materials Science and Engineering A*. 2004, vol. 375-377, pp. 1044-1047.

[31]. W. Tang, Y.Q. Wu, K.W. Dennis, M.J. Kramer, I.E. Anderson, R.W. McCallum, "Comparison of Microstructure and magnetic properties of Gas-Atomized and Melt-Spun MRE-Fe-Co-M-B (MRE=Y+Dy+Nd, M=Zr+TiC)," *Journal of Applied Physics*. May 2007, in press.

[32]. W.J. Boettinger, J.H. Perepezko, "Fundamentals of Rapid Solidification," in *Rapidly Solidified Crystalline Alloys*, edited by S.K. Das, B.H. Kear, C.M. Adam, TMS-AIME, Morristown, New Jersey, May 1985, 21-58.

[33]. J.H. Perepezko, I.E. Anderson, "Metastable Phase Formation in Undercooled Liquids," *Synthesis and Properties of Metastable Phases*, edited by E.S. Machlin, T.J. Rowland, Proceedings of AIME. October 1980, 31-63.

[34]. I.E. Anderson, M.P. Kemppainen, "Undercooling Effects in Gas Atomized Powders," *Undercooled Alloy Phases*, TMS-AIME, edited by E.W. Collings, C.C. Koch. 1986, 269-285.

[35]. R. Mehrabian, "Relationship of heat flow to structure in rapid solidification processing," *Rapid Solidification Processing Principles and Technologies*; Proceedings of the International Conference on Rapid Solidification Processing November 13-16, 1977. Edited by R. Mehrabian, B.H. Kear, M. Cohen. Baton Rouge, LA: Claitors, 1978, 9-27.

[36]. S.N. Sahu, S. Harikishore, S.C. Koria, "Solidification behaviour of droplets in spray deposition," Powder Metallurgy. 2005, 48, 3, 270-276.

[37]. R. Mehrabian, S.C. Hsu, C.G. Levi, S. Kou, "Heat Flow Limitations in Rapid Solidification Processing," in *Advances in Metal Processing*. Plenum Press, 1981, 13-43.

[38]. R. Mehrabian, "Rapid Solidification," *International Metals Review*. 1982, 27, 4, 185-208.

[39]. N.L. Buelow, "Microstructural investigation of mixed rare earth iron boron processed via melt-spinning and high-pressure gas atomization," Iowa State University Masters Thesis, 2005.

[40]. B. Grieb, E.T. Henig, G. Schneider, G. Petzow, "Phase Relations in the Systems Fe-Dy-B and Fe-Tb-B," *Zeitschrift Fuer Metallkunde*. 1989, 80, 2, 95-100.

[41]. G. Schneider, E.T. Henig, G. Petzow, H.H. Stadelmaier, "Phase Relations in the System Fe-Nd-B," *Zeitschrift Fuer Metallkunde*. 1986, 77, 11, 755-761.

[42]. G.F. Stepanchikova, Y.B. Kuz'ma, "Yttrium-Iron-Boron System," *Soviet Powder Metallurgy and Metal Ceramics*, translated from *Poroshkovaya Metallurgiya*, Kiev. 1980, 19, 697-699.

[43]. M. Sagawa, "Review of Sintering Process Development for Nd-Fe-B," *Journal of Materials Engineering.* 1991, 13, 95-101.

[44]. H.H. Liebermann, R.L. Bye, Jr., "Rapid Solidification Processing and Its Effects on Microstructure of Metallic Alloy Strip," in *Rapidly Solidified Crystalline Alloys*, edited by S.K. Das, B.H. Kear, C.M. Adam, TMS-AIME, Morristown, New Jersey, May 1985, 61-76.

[45]. D.J. Branagan, "A Metallurgical Approach Toward Alloying in Rare-Earth Permanent Magnet Systems," Iowa State University Dissertation, 1995.

[46]. M.J. Kramer, L.H. Lewis, Y. Tang, K.W. Dennis, R.W. McCallum, "Microstructural refinement in melt-spun $Nd_2Fe_{14}B$," *Scripta Materialia*. 2002, 47, 557-562.

[47]. Y.L. Tang, M.J. Kramer, K.W. Dennis, R.W. McCallum, L.H. Lewis, "On the control of microstructure in rapidly solidified Nd-Fe-B alloys through melt treatment," *Journal of Magnetism and Magnetic Materials*. 2003, 267, 307-315.

[48]. J. Ting, I.E. Anderson, "A Computational fluid dynamics (CFD) investigation of the wake closure phenomenon," *Materials Science and Engineering A*. 20004, 379, 264-276.

[49]. N.L. Buelow, I.E. Anderson, R.W. McCallum, M. J. Kramer, W. Tang, and K.W. Dennis, "Microstructure and Magnetic Properties of Gas Atomized Powders of Mixed Rare Earth Iron Boron," *Advances in Powder Metallurgy and Particulate Materials*. Compiled by C. Ruas and T.A. Tomlin, Metal Powder Industries Federation, Princeton, NJ, 2005, pp.74-88.

[50]. P.C. Guschl, P. Campbell, "Rare-Earth Fe-B Powder Coating for Improvements in Corrosion Resistance, Flux Aging Loss, and Mechanical Strength of Bonded Magnets," *IEEE Transactions on Magnetics*. October 2005, 41, 10, 3859-3861.

[51]. D.N. Brown, Z. Chen, P. Guschl, P. Campbell, "Developments with melt spun RE-Fe-B powder for bonded magnets," *Journal of Magnetism and Magnetic Materials.* 2006, 303, e371-e374.

[52]. Frederick A. Schmidt, private communication, Ames Laboratory USDOE, 24 October 2006.

[53]. M. Cannon Sneed, J. Lewis Maynard, *General Inorganic Chemistry*, Chapter 13 The Halogens, New York, 1942, 256-257.

[54]. F. A. Schmidt, D.T. Peterson, "Nd-Fe Alloy by Thermite Reduction Processing," Report for the U.S. Department of Commerce Grant ITA 87-02, Project 87-1. June 1989.

[55]. E. Vileno, M.K. LeClair, S.L. Suib, M.B. Cutlip, F.S. Galasso, S.J. Hardwick, "Thermal Decomposition of NF_3 with Various Oxides," *Chemistry of Materials*. 1996, 8, 1217-1221.

[56]. E. Vileno, M.K. LeClair, S.L. Suib, M.B. Cutlip, F.S. Galasso, S.J. Hardwick, "Thermal Decomposition of NF_3 by Ti, Si, and Sn Powders," *Chemistry of Materials*. 1995, 7, 683-687.

[57]. W.A. Cannon, S.K. Asunmaa, W.D. English, N.A. Tiner, "Passivation Reactions of Nickel and Copper Alloys with Fluorine," *Transactions of the Metallurgical Society of AIME*. August 1968, 242, 8, 1635-1643.

[58]. T.M. Klapötke, "Nitrogen-fluorine compounds," *Journal of Fluorine Chemistry*. 2006, 127, 679-687.

[59]. E.G. Rakov, G.A. Yagodin, V.P. Zagorets, I.Y. Andreev, V.I. Goncharov, "Fluorination of Rare Earth Metals," *Russian Journal of Inorganic Chemistry (Zhurnal Neorganicheskoi Khimii)*. 1979, 24, 4, 857-859.

[60]. V.Y. Leonidov, P.A.G. O'Hare, "Fluorine combustion calorimetry: progress in recent years and possibilities of further development," *Pure & Applied Chemistry.* 1992, 64, 1, 103-110.

[61]. G.K. Johnson, R.G. Pennell, K.Y. Kim, W.N. Hubbard, "Thermochemistry of rare-earth trifluorides I. Fluorine bomb calorimetric determination of the enthalpies of formation of LaF_3, PrF_3, NdF_3, GdF_3, DyF_3, HoF_3, and ErF_3," *Journal of Chemical Thermodynamics*. 1980, 12, 125-136.

[62]. R.C. Vickery, *The Chemistry of Yttrium and Scandium,* (Great Britain: Pergamon Press LTD., 1960), vol. 2.

[63]. K. A. Gschneidner, Jr., N. Kippenhan, O.D. McMasters, "Thermochemistry of the Rare Earths Part 1. Rare Earth Oxides," (Report IS-RIC-6, Ames Laboratory – U.S. Atomic Energy Commission, 1973).

[64]. H. Rau, "Thermodynamics of the reduction of iron oxide powders with hydrogen," *Journal of Chemical Thermodynamics*. 1972, 4, 1, 57-64.

[65]. M.L. Anderson, "Surface passivation and electrochemical behavior of gas atomized $LaNi_{4.75}Sn_{0.25}$ for battery applications," Iowa State University Masters Thesis, 2000.

[66]. M. Sakashita, Z.P. Li, S. Suda, "Fluorination mechanisms and its effects on the electrochemical properties of metal hydrides," *Journal of Alloys and Compounds*. 1997, 253-254, 500-505.

[67]. R.M. German, *Powder Injection Molding*, First Edition. 1990, Metal Powder Industries Federation, Princeton, NJ.

[68]. D. Goll, H. Kronmüller, "High-performance permanent magnets," *Naturwissenschaften.* 2000, 87, 423-438.

[69]. M. G. Garrell, B.M. Ma, A. J. Shih, E. Lara-Curzio, R.O. Scattergood, "Mechanical properties of polyphenylene-sulfide (PPS) bonded Nd-Fe-B permanent magnets," *Materials Science and Engineering A*. 2003, 359, 375-383.

[70]. J. Hemrick, E. Lara-Curzio, K. Liu, B.M. Ma, "Mechanical properties of thermally cycled nylon bonded Nd-Fe-B permanent magnets," *Journal of Materials Science*. 2004, 39, 6509-6522.

[71]. P.C. Guschl, H.S. Kim, J. U. Otaigbe, "Effects of a Nd-Fe-B Magnetic Filler on the Crystallization of Poly(phenylene sulfide)," *Journal of Applied Polymer Science*. 2002, 83, 1091-1102.

[72]. J. Liu, M. Walmer, "Bonded Rare Earth Magnets Produced by Hot Pressing," in *Bonded Magnets*, edited by G.C. Hadjipanayis, NATO Science Series II. Mathematics, Physics and Chemistry, 2003, 118, 55-72.

[73]. S. Constantinides, Evaluation of Ames Laboratory Magnet Alloy MQP-11-HTP, Laboratory Report AMTC-60620-A. 20 June 2006.

[74]. P.K. Sokolowski, I.E. Anderson, W. Tang, Y.Q Wu, K.W. Dennis, M.J. Kramer, R.W. McCallum, "Microstructural and Magnetic Studies of Gas Atomized Powder and Melt Spun Ribbon for Improved $MRE_2Fe_{14}B$," *Advances in Powder Metallurgy and Particulate Materials*. Compiled by William R. Gasbarre and John W. von Arx, Metal Powder Industries Federation, Princeton, NJ, 2006, pp.152-167.

[75]. James W. Anderegg, private communication, Ames Laboratory USDOE, 2 November 2006.

[76]. Y.M. Cross, J. Dewing, "Thickness Measurements on Layered Materials in Powder Form by Means of XPS and Ion Sputtering," *Surface and Interface Analysis*. 1979, 1, 1, 26-31.

[77]. A.L. Genau, "Microstructural development in Al-Si powder during rapid solidification," Iowa State University Masters Thesis, 2004.

[78]. A.L. Cabrera, E.J. Karwacki, J.F. Kirner, "Surface analysis of copper, brass, and steel foils exposed to fluorine containing atmospheres," *Journal of Vacuum Science and Technology A*. Nov/Dec 1990, 8, 6, 3988-3996.

[79]. M. Takashima, "Preparation and properties of binary rare-earth oxide-fluorides," *Journal of Fluorine Chemistry*. 2000, 105, 249-256.

[80]. M. Takashima, "Oxide Fluorides of Rare Earth Elements," in Advanced Inorganic Fluorides: Synthesis, Characterization and Applications. 2000.

ACKNOWLEDGEMENTS

The development of this thesis has certainly come about through the people that have influenced my education throughout the past several years. Most prominent to its maturity has been the involvement and support shown by my major professor, Iver Anderson. His encouragement and belief in my abilities is without doubt, a significant source of motivation for pursuing this degree in the first place. In addition to his guidance, I would also like to express my appreciation to the other committee members, Bill McCallum and Frank Peters, for taking the time to evaluate my work and provide insightful feedback on the research approach.

A majority of the results presented in the document could not have been accomplished without the work performed by several individuals. My sincere appreciation to Wei Tang for providing magnetometer measurements and his critical knowledge in magnetics, Yaqiao Wu for taking the TEM images, and Kevin Dennis for his capability to troubleshoot equipment related problems at any given time. Additionally, Jim Anderegg's expertise and interpretation of data with the Auger and XPS systems was invaluable to the success of this research. I would also like to thank everyone at the Materials Preparation Center of Ames Lab for doing excellent work in providing the materials and teaching me how to utilize the equipment. Particularly, Ross Anderson and Dave Byrd for the atomization runs, Hal Sailsbury for his metallography expertise and always interesting conversations, Dave Rehbein for his help with the RGA system, and Rick Schmidt for his knowledge of rare earth based fluorides. The opportunity to work with the late Robert L. Terpstra, whose untimely passing left a significant void in our research group, was uniquely influential to my education and growth. Thank you, Bob, for always taking the time to help.

Also, the suggestions and critiques given by my peers Eren Kalay, Joel Rieken, and Jason Walleser have been especially helpful over the past couple of years. Nick Buelow was instrumental in laying the groundwork for this project and his achievements were particularly useful during my progress. The experimental work performed by Lynn Tweed, Amy

Bergerud, and Nathaniel Oster is also appreciated and I am grateful for their devotion in helping me develop the fluorination system. To my family and friends, thank you for your unwavering support. I could not have achieved this without your presence and desire to be involved in my life. This work was performed at Ames Laboratory under Contract no. DE-AC02-07CH11358 with the U.S. Department of Energy through the DOE-EE-FCVT Freedom Car Initiative program. The United States government has assigned the DOE Report number IS-T2887 to this thesis.